Research on

Engineering
Structures &
Materials

R E S M

J R E S M

MiM
Research Group

The International Journal of **Research on Engineering Structures and Materials (RESM)** is a peer-reviewed open access journal (p-ISSN: 2148-9807; o-ISSN: 2149-4088) published by MIM Research Group. It is published in February, June, September, and December.

The main objective of RESM is to provide an International academic platform for researchers to share scientific results related to all aspects of mechanical, civil and material engineering areas.

RESM aims the publication of original research articles, reviews, short communications technical reports, and letters to the editor on the latest developments in the related fields.

All expenditures for the publication of the manuscripts are most kindly reimbursed by *MIM Research Group*. Thus, authors do not need to pay for publishing their studies in the journal.

The scope of the journal covers (but not limited to) behavior of structures, machines and mechanical systems, vibration, impact loadings and structural dynamics, mechanics of materials (elasticity, plasticity, fracture mechanics), material science (structure and properties of concrete, metals, ceramics, composites, plastics, wood, etc.,), nano-materials performances of new and existing buildings and other structural systems, design of buildings and other structural systems, seismic behavior of buildings and other structural systems, repair and strengthening of structural systems, case studies and failure of structural systems, safety and reliability in structural and material engineering, use of new and innovative materials and techniques in energy systems and mechanical aspects of biological systems (biomechanics and biomimetics).

The topics covered in RESM include:

- Structural Engineering
- Mechanical Engineering
- Material Engineering
- Earthquake Engineering
- Nano-technology
- Energy Systems
- Biomechanics and Biomimetics

Abstracting and Indexing
Please visit http://www.jresm.org for more information.

Graphics and Design

H Ersen Balcıoğlu   ersen.balcioglu@usak.edu.tr

Yunus Demirtaş   yunus.demirtas@usak.edu.tr

RESEARCH on
ENGINEERING STRUCTURES &
MATERIALS

Advisory Board Members

Yaser Acikbas	Usak University	Turkey
Yasin Alemdag	Karadeniz Technical University	Turkey
Samim Ali	National Institute of Standards and Technology	USA
Duygu Alparslan	Yuzuncu Yıl University	Turkey
Irekti Amar	University M'Hamed Bougara of Boumerdes	Algeria
Carla Tatiana Mota Anflor	University of Brasilia	Brazil
Faezeh Atri	Tehran University of Medical Sciences	Iran
Massimiliano Avalle	Università degli Studi di Genova	Italy
Ozgur Avsar	Eskisehir Technical University	Turkey
Ayse Aytac	Kocaeli University	Turkey
Huseyin Ersen Balcıoglu	Usak University	Turkey
Raffaele Barretta	University of Naples Federico II	Italy
Kleber Bianchi	Universidade Federal de Goias	Brazil
Antonio Caggiano	University of Buenos Aires	Brazil
Sanjay Kumar Chak	Netaji Subhas Institute of Technology	India
Leda Coltro	Instituto de Tecnologia de Alimentos	Brazil
Sérgio Correia	Pólo II da Univ. de Coimbra	Portugal
Eduardo Costa Couto	Federal University of Pelotas	Brazil
Thiago da Silveira	Universidade Federal do Pampa	Brazil
Preeta Datta	North Carolina State University	USA
Hasan Demir	Osmaniye Korkut Ata University	Turkey
Ayse Pınar Demir	Usak University	Turkey
Umit Bilge Demirci	French National Centre for Scientific Research	France
Leonid Director	Russian Academy of Science	Russia
Halil Enginsoy	Usak University	Turkey

Advisory Board Members

Yavuz Ergun	Usak University	Turkey
Tuba Ersen Dudu	Yuzuncu Yıl University	Turkey
Saeed Farahani	Clemson University	USA
Carlos Eduardo Marcos Guilherme	Universidade Federal do Rio Grande	Brazil
Alper Gurarslan	Comftech Co.	Italy
Ahmet Gural	Gazi University	Turkey
Dulce Franco Henriques	Instituto Politécnico de Lisboa	Portugal
Saddam Hossain	Bangladesh University of Engineering and Technology	Bangladesh
Liércio André Isoldi	Universidade Federal do Rio Grande	Brazil
Berrin Ikizler	Ege University	Turkey
Zeynep İlbay	Usak University	Turkey
Ali Karaipekli	Cankırı Karatekin University	Turkey
Alp Karakoc	Aalto University	Finland
Jibran Khaliq	Northumbria University	UK
Mehdi Khorasanian	Shahid Chamran university of Ahvaz	Iran
João Paulo Silva Lima	Universidade Federal de Goias	Brazil
Gabriela Lujan Brollo	University of Campinas	Brazil
Ahmed Maamoun	McMaster University	Canada
Avik Mahata	Missouri University of Science and Technology	USA
K. K. Mahato	National Institute of Technology	India
Upendra K. Mallela	L&L Technology Services	India
Najoua Mekaddem	National Engineering School of Gabes	Tunisia
Suha Orcun Mert	Yuzuncu Yıl University	Turkey
Masoomeh Mirrashid	Semnan University	Iran
Mohsin Talib Mohammed	Kufa University	Iran

Advisory Board Members

Márcio Wrague Moura	Universidade Federal do Rio Grande	Brazil
Muhammad Muddassir	Institute for Composite Materials	Germany
Khurram Munir	RMIT University	Australia
Andrea Mura	Politecnico di Torino	Italy
Engin Nacaroglu	Pamukkale University	Turkey
Susmita Naskar	Johns Hopkins University	USA
Mu Naushad	King Saud University	Saudi Arabia
Olga Netskina	Boreskov Institute of Catalysis	Russia
Hayri B. Ozmen	Usak University	Turkey
Fehime Ozkan	Izmir Intitute of Technology	Turkey
Charlei Marcelo Paliga	Federal University of Pelotas	Brazil
Krishna Murari Pandey	National Institute of Technology	India
Ramon Peña-Garcia	Universidade Federal de Pernambuco	Brazil
Matheus Poletto	University of Caxias do Sul	Brazil
K. Venkatesh Raja	K.S.R. College of Engineering	India
Mauro de Vasconcellos Real	Federal University of Rio Grande	Brazil
Raif Sakin	Balıkesir University	Turkey
Kamyar Shirvani Moghaddam	Deakin University	Australia
Brijesh Singh	National Council for Cement and Building Materials	India
Bheemappa Suresha	The National Institute of Engineering	India
Gulsah Susurluk	Beykent University	Turkey
Selin Sahin Sevgili	İstanbul Cerrahpaşa University	Turkey
Hossein Taghipoor	Semnan University	Iran
Paulo Teixeira	Universidade de Lisboa	Portugal
Tugce Tezel	Akdeniz University	Turkey
Canan Uraz	Ege University	Turkey

Advisory Board Members

In This Issue

In This Issue

ABSTRACTING / INDEXING

The international journal of Research on Engineering Structures and Materials (RESM) is currently Absracted/Indexed by CrossRef, Google Scholar, Universal Impact Factor, Scientific Indexing Service, Research Bible, CiteFactor, Electronic Journal Library, Open Academic Journals Index, Global Impact Factor, Directory of Research Journals Indexing, Materials Science & Engineering Database (ProQuest) Engineering Journals (ProQuest), ULAKBİM TR Index (Tubitak) and under evaluation by many other respected indexes.

Check web site for current indexing info.
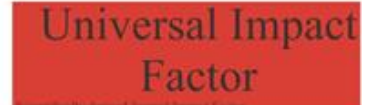
Research Article

Preparation of single- and double-layer antireflective coatings by sol-gel method

Berrin İkizler*,a

Department of Chemical Engineering, Ege University, Bornova, İzmir, Turkey

Article Info	Abstract
	Antireflective (AR) SiO_2 coatings were developed in this work to increase the transmittance of glass in the visible light range of 400-800 nm, due to their potential applications on solar energy systems. Also, double-layer AR coatings were prepared by covering AR SiO_2 layer with a dense TiO_2 layer with the aim of protecting AR layer from environmental effects. SiO_2 coatings were obtained with sol-gel and dip coating methods, by using acid- and base-catalyzed silica sols as precursors. Only 1% transmittance increase was gained with acid-catalyzed SiO_2 coating due to its dense structure. On the contrary, SiO_2 coatings formed by base-catalyzed sol have transmittance > 99% in the 460-660 nm range and of 99.8% at 550 nm, corresponding to the wavelength at maximum intensity of solar spectrum. This high values were attributed to the porous structure of the film revealed by SEM and AFM analysis, and to the optimized thickness of coating achieved at 90-120 mm/min withdrawal speeds. Transmittance of base-catalyzed SiO_2 coatings decreased to an average value of 96.2% after coated with high refractive index TiO_2 layer. However, still a 5-6% achievement in transmittance of glass in 400-800 nm range was attained by optimizing the thickness of each layer using different withdrawal speeds, and concentration and types of the precursor sols. Characterization of the coatings was performed with SEM, AFM, EDS and FTIR analysis.

1. Introduction

Antireflective (AR) coatings decrease the reflectance of the light directed towards them, thus resulting in a high degree of light transmittance. These optical coatings can be applied to all surfaces where a minimum loss of light is required. However, achieving a high transmission of light through glass is an important research subject especially for the solar energy systems, as in photovoltaic and solar thermal devices, to enhance their effectiveness [1-3]. AR coatings are widely applied to increase the solar radiation absorption in these systems, by reducing the natural reflectance loss (~8-9%) of glass components, such as, glass envelops of the receiver tubes in parabolic trough collectors, glass covers of solar collectors, and glass covers of photovoltaic devices to protect its components from outdoor environment [2-5]. AR coatings are also used in a great number of technological application areas like, high power laser systems, camera and telescope lenses, architectural glasses, eyeglasses, TV screens, display panels, touch screens, etc. [1,6-8].

AR coatings attain minimum or zero reflectance if their thickness and also refractive index are appropriately adjusted [8]. The refractive index of an AR coating (n_c) should satisfy the condition given in Eq. (1) to achieve, theoretically, zero-reflectance [8].

$$n_c = (n_0 \times n_s)^{1/2} \tag{1}$$

where n_0 and n_s are the refractive indexes of the medium and the substrate, respectively. Refractive index of glass material, the substrate, is known to be 1.47-1.57. Therefore, AR films applied on a glass surface must have a refractive index (RI) value of 1.21-1.25 to reach zero-reflectivity in air medium ($n_0 \approx 1.0$) [9]. The common materials used as AR coating in the visible range are SiO_2 (n_c=1.45), Al_2O_3 (n_c=1.65), MgF_2 (n_c=1.38), SiO (n_c=1.85) and ZnO (n_c=2.0) [9,10], but, none of these materials has such a low RI value. Among these materials, SiO_2 is generally preferred due to its relatively low RI value [11]. As the refractive index is proportional to the material density, having a porous structure will help to decrease a material's RI value to the desired levels [11].

Among many coating techniques, it is possible by sol-gel method to produce a porous structure required for achieving a low RI and to control the distribution of the pores within the structure [12]. This method has many advantages when compared to coating technologies such as CVD and sputtering: a simple and inexpensive process; easily coating of even large and complex surfaces, industrial applicability via dipping and spraying; and easy control of process parameters [12-14].

Single-layer AR coatings improve the light transmittance of a substrate effectively but only for narrow wavelength range. For the success in a broad spectrum range, double or multilayer AR coatings are required with an increased optical performance [10,15]. Production of such systems is needed to combine coating layers having different refractive indexes. It is of general practice to choose pairs of materials having high (2.0-2.3) and low (1.45-1.52) indexes [9]. In addition, thickness of each layer should be adjusted in such a way that a destructive interference of light between layers is created, which will consequently cause a low reflectance value. Double-layer AR coatings are generally developed by using a very low refractive index material, such as porous SiO_2 or fluorides, at the outer layer to achieve minimum reflectivity [8,9]. Although these systems attain excellent optical features by this way, their mechanical strength and long-term stability are reported to be relatively poor for outdoor applications [8,9]. Therefore, contrary to the most of the works given in literature [4,9], it is needed to develop double-layer AR systems by covering the inner SiO_2 layer with an outer layer, which will have a protective role against environmental factors [3]. Typically, the materials such as TiO_2, WO_3, ZrO_2, ZnO, SnO_2 and CdS are used for this purpose [3,8,9,16]. Among these, TiO_2 films are distinguished because of its high mechanical strength, high chemical stability and superhydrophilic property under UV light, besides its well-known self-cleaning feature [16]. Nevertheless, its refractive index, 2.3-2.5, is too high [16] so an outer TiO_2 layer will significantly reduce the light transmittance when used in double layer AR systems. Thus, development of multifunctional coatings, integrating the antireflective and durability characteristics into one stack and working in the whole visible light range, are still a challenging task [3]. One of the approaches for this purpose is to make a porous TiO_2 layer over the double layer system to lower its refractive index, and consequently increase the transmittance of the AR system. Removable organic templates (Pluronic F127, Triton X-100, PEG, etc.) are used in the sols as pore making agents, but these methods require high annealing temperatures, like 400-500°C to remove these organic materials [8,12,17]. Another approach is to use colloidal particles dispersed in a solvent [18]. After solvent removal, a porous titania layer is left over the surface. However Zhang et al. [18] found that, the resultant double-layer coating was not too effective to enhance the transmittance of glass. Thus, the goal of the present study is to produce AR double layer coatings

synthesized under very low temperatures with enhanced AR properties that will be applicable to any transparent substrate.

In this work, single-layer SiO_2 and double-layer SiO_2/TiO_2 coatings are developed to maximize the transmission of light through glass slides in the entire visible light range of 400-800 nm. AR features are gained by SiO_2 coatings and TiO_2 is selected to perform as a protective layer. Sol-gel and dip coating techniques are used in the deposition of the coatings. At first step, deposition conditions of single-layer SiO_2 and also single-layer TiO_2 films are optimized individually for a maximum light transmittance. Withdrawal speeds (30-240 mm/min) of the substrates are adjusted for an optimum film thickness of the films. SiO_2 films are obtained using both acid-and base-catalyzed sols in order to change the porosity of the resultant film. However, TiO_2 films are synthesized using only acid-catalyzed sols to form a dense film in the final AR coatings. As a second step, the optimized conditions are combined together to form double-layer SiO_2/TiO_2 coatings. The drawback appeared by the use of TiO_2 as top layer is overcame by controlling the thickness of each layer, so keeping the AR properties of the SiO_2 layer. Coating thickness is optimized by changing the withdrawal speed and concentration of titanium in the coating sol.

2. Materials and Methods

2.1. Materials

All chemicals used in the experiments were of analytical grade and purchased from Sigma-Aldrich. Tetraethyl orthosilicate (TEOS, $Si(OC_2H_5)_4$, 99%) and tetrabutyl orthotitanate (TBOT, $Ti(OC_4H_9)_4$, 97%) were used as the precursors of the silica and titania sols, respectively. NH_3 (28-30%) was used as the base catalyst in the system and HCl (37%), as the acid catalyst. Absolute ethanol (EtOH, 99.8%) was selected as the solvent of the sols. Ultrapure water (18.2 $M\Omega$.cm) was used in the experiments and obtained from Millipore Direct-Q8-UV water purification system. Soda-lime glass slides (2.6×7.6 cm, Marienfeld Co.) with thickness of 1 mm were used as substrates for the deposition of coatings. Glass substrates (G, in short) prior to usage were cleaned ultrasonically in acetone and ethanol for 15 min. They were then immersed in concentrated sulfuric acid for one week, followed by thorough washing with distilled water.

2.2. Preparation of Sols

2.2.1 Preparation of SiO₂ Sols

Silica sols were prepared by using either a base or an acid catalyst to investigate the effect of catalyst type on the AR properties. For the base-catalyzed sol, NH_3-EtOH mixture was added dropwise into TEOS-EtOH mixture under vigorous stirring. The resultant sol was stirred further for 2 h at 25°C. The transparent silica sol with a pale blue color was obtained after aging for 2 days at 25°C. The molar ratio of $TEOS:H_2O:NH_3:EtOH$ in the final solution was 1:2.37:1:38 [19], and the concentration of silicon ions was 0.4 mol/L (pH ≈ 10.8). Acid-catalyzed silica sol was prepared by the dropwise addition of H_2O-EtOH mixture into TEOS-HCl-EtOH mixture under vigorous stirring. The molar ratio of $TEOS: H_2O:HCl:EtOH$ in the final solution was 1:4:0.004:80.4 (pH ≈ 3) [20]. The transparent sol was aged for 2 days prior to usage. SiO_2 coatings obtained by using the base-catalyzed sol and by using the acid-catalyzed sol were shortly denoted as B-SiO_2 and A-SiO_2, respectively, in the text.

2.2.2 Preparation of TiO₂ Sols

Titania sols were prepared by hydrolyzing TBOT-HCl-EtOH mixture with the dropwise addition of H_2O-EtOH mixture under vigorous stirring. The resultant transparent acid-catalyzed sol was stirred further for 2 h and also aged for 2 days prior to usage. The molar ratio of $TBOT:H_2O:HCl:EtOH$ was 1:3.55:0.22:164 [20] with a final titanium concentration

of 0.1 mol/L (pH ≈ 1.6). In addition, a titania sol having 0.2 mol/L titanium concentration was also prepared by using the molar ratios of components as 1:3.55:0.22:78.3 (pH ≈ 1.3), to investigate the effect of titanium concentration on the AR properties.

2.3. Deposition of Coatings on Glass Surface

Single-layer SiO_2 (G/SiO_2) or single-layer TiO_2 (G/TiO_2) coatings were obtained by depositing appropriate sols onto the both sides of the clean substrates using dip coating technique. The as-coated films were then dried at 120°C for 3 h in an oven under ambient atmosphere. The effects of dip-coating parameters (withdrawal speed (WS) and also dwell time of the substrates in the sols) were investigated in detail to enhance the AR properties of single-layer coatings.

Double-layer coatings (G/SiO_2/TiO_2) were produced by coating the glass substrates first with SiO_2 layer (inner layer) and then with TiO_2 layer (outer layer). Each layer was heated at 120°C for 3 h. The following parameters were investigated to maximize the AR properties of the double-layer coatings: Withdrawal speeds, catalyst type of the SiO_2 coatings (A-SiO_2 and B-SiO_2) and titanium concentration in the TiO_2 sols (0.1 M and 0.2 M).

2.4. Characterization

Field emission scanning electron microscopy (SEM, ThermoScientific/Apreo S) was used in the morphological characterization of SiO_2 and TiO_2 coatings. The thickness of the coatings was determined from the cross-sectional SEM view of the samples. The elemental analysis of the coatings in terms of atomic percent was done by energy dispersive X-ray spectroscopy (EDS) connected to the SEM. The surface topography of the coatings was identified by BRUKER-Dimension Edge with ScanAsyst atomic force microscopy (AFM). AFM analysis was conducted in tapping mode for a scan area of 3 μm × 3 μm. The surface roughness values were obtained after the analysis of AFM images and represented in terms of root mean square roughness (R_q). Chemical structure of the films was detected by Fourier transform infrared spectrophotometer (FTIR, Perkin Elmer/Spectra100) with ATR attachment, working in the range of 4000-650 cm^{-1}. AR properties, optical transmittance and reflectance, of the glass substrates before and after coated with different films were determined with UV-Visible spectrophotometer having a 60 mm integrating sphere attachment (Shimadzu/UV-2600-ISR), in the wavelength range of 300-1000 nm.

3. Results and Discussions

3.1. Development of Antireflective SiO_2 Coatings

SiO_2 is used to form an AR layer over glass surface because of its low refractive index (RI) value. SiO_2 film is deposited on the surface with sol-gel polymerization of TEOS in ethanol and water under either acid- or base-catalyzed conditions. A network of Si–O–Si gel is obtained after the hydrolysis of the alkoxysilane, TEOS, as given in Eq. (2) and polycondensation of the hydrolyzed species (Eqs. (3)-(4)) [21].

$$\equiv Si - OC_2H_5 + H_2O \xrightarrow{H^+ or\ OH^-} \equiv Si - OH + C_2H_5OH \qquad (2)$$

$$\equiv Si - OH + \equiv Si - OC_2H_5 \xrightarrow{H^+ or\ OH^-} \equiv Si - O - Si \equiv\ + C_2H_5OH \qquad (3)$$

$$\equiv Si - OH + \equiv Si - OH \xrightarrow{H^+ or\ OH^-} \equiv Si - O - Si \equiv\ + H_2O \qquad (4)$$
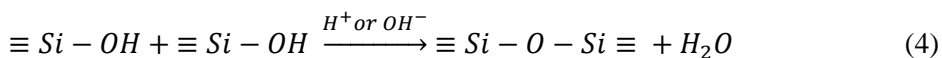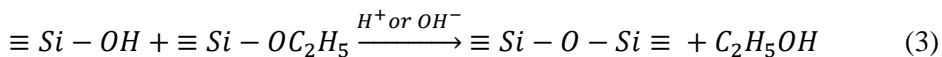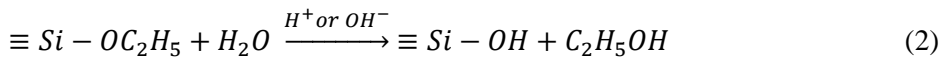
3.1.1 Effect of Catalyst Type

The hydrolysis and polycondensation reactions, in Eqs. (2)-(4), depend on many parameters like catalyst type, concentration of species, type of solvent, temperature, etc [22]. However, type of catalyst might have the utmost importance in determining the rate of hydrolysis and condensation reactions, thus in turn, the growth behavior of SiO_2 colloidal particles in a gel. Under acid-catalyzed conditions, primary silica particles tend to form linear or randomly branched polymeric chains. These chains entangle and are also cross-linked during growth stage, finally resulting in a dense gel film over the surface [23,24]. The porosity of this dense film is relatively low, therefore, coatings obtained from acid-catalyzed sols have a refractive index value of ~1.44 [23-26], nearly the same as that of bulk SiO_2 (n_c=1.45). Using a base catalyst instead leads to a spherically expanding particle (cluster) growth. The growth of these discrete colloidal particles leads to a network structure formation, where voids in nanometer scale are entrapped between them, eventually resulting in a porous film formation over the surface at the end of gelation. Thus, refractive index of SiO_2 coatings obtained by using the base-catalyzed sol (B-SiO_2) is reported to be in the range of 1.12-1.35 depending on the resultant pore volume [19,23,24,27]; remarkable lower than the one using the acid-catalyzed sol (A-SiO_2).

The dense and porous structure of the A-SiO_2 and B-SiO_2 coatings are assessed with SEM analysis, shown in Fig. 1(a) and (b), respectively. The films are coated at 120 mm/min withdrawal speed. Fig. 1(a) points out a smooth and dense surface structure for the acid-catalyzed SiO_2 coatings. This must be the consequence of dense packing of chain-like polymeric particle network. On the contrary, the surface of coatings deposited from the base-catalyzed sol shows a rather rough surface, as given in Fig. 1(b). Silica aggregates (light sides) and voids between them (darker sides) can be distinguished from the top surface view. Similar SEM images were also obtained by Xiao et al. [25] for both acid- and base-catalyzed SiO_2 coatings. The cross-sectional SEM views, given as an inset in Fig. 1(a) and (b), revealed that B-SiO_2 film are formed from individual silica clusters in spherical form while only a dense film is detected in A-SiO_2 coatings, probably because of its small primary particles. The thickness of A-SiO_2 and B-SiO_2 layers is measured as ~31±3 nm and ~140±4 nm, respectively. The EDS analysis performed during SEM study indicate the existence of only silicon and oxygen atoms in the coatings regardless of the catalyst type. Silicon atom at 33.33 at.% and oxygen atom at 66.67 at.% prove that silica film is in the oxide state, as given in Fig. 1(c) and (d) for A-SiO_2 and B-SiO_2, respectively.

AFM measurements are performed to elucidate more clearly the surface morphologies of SiO_2 coatings and their roughness profiles. The results are shown in Fig. 2 and confirm the SEM observations. Three-dimensional (3D) AFM images verify that acid-catalyzed SiO_2 coating consists of very tiny particles (Fig. 2(a)), whereas, base-catalyzed SiO_2 coating is formed from relatively bigger and discrete particles in spherical form (Fig. 2(b)). The size of particles measured from AFM images, are found to be in the range of 5-20 nm for A-SiO_2 and 30-70 nm for B-SiO_2 coatings, compatible with the mean particle sizes obtained by Vincent et al. [24]. Surface roughness of the coatings is also characterized by AFM analysis for the entire scan area of 3 μm x 3 μm. Root mean square roughness (R_q), the standard deviation of the distribution of profile heights, is measured as 0.47 nm for A-SiO_2 and 2.85 nm for B-SiO_2 films. The roughness values of the coatings are in good agreement with the R_q values of acid-catalyzed SiO_2 (0.394 nm) and porous SiO_2 (2.914 nm) coatings, deposited in the work of Wang et al. [28].The very low R_q value of A-SiO_2 proves that these coatings have atomically smooth surface structure, which could only be obtained by the dense packing of tiny particles. B-SiO_2 film have relatively rough surface when compared to A-SiO_2 film, apparently due to the size of its particles and the voids remained between these discrete particles. Representative cross-sectional views of the 3D images are depicted in Fig. 2(c) and (d) to reveal the height profile changes of the film surfaces

evidently. The height profile (peak heights/valley depths) of A-SiO$_2$ film remains within the ±1 nm range (Fig. 2(c)), verifying the smoothness of the surface. However, the larger amplitude peaks and valleys within the range of ±6 nm (Fig. 2(d)) for B-SiO$_2$ film can be attributed to its rough surface structure. Moreover, the peak widths in the surface profiles could be taken as an indication of the size of the particles. When compared to narrow peak widths of A-SiO$_2$ film, larger peak widths signify the bigger particle existence within the B-SiO$_2$ film. Smooth and relatively rough surface morphologies for acid- and base-catalyzed SiO$_2$ coatings were also demonstrated by Li and Shen [26] and Wu et al. [23] in their AFM analysis.
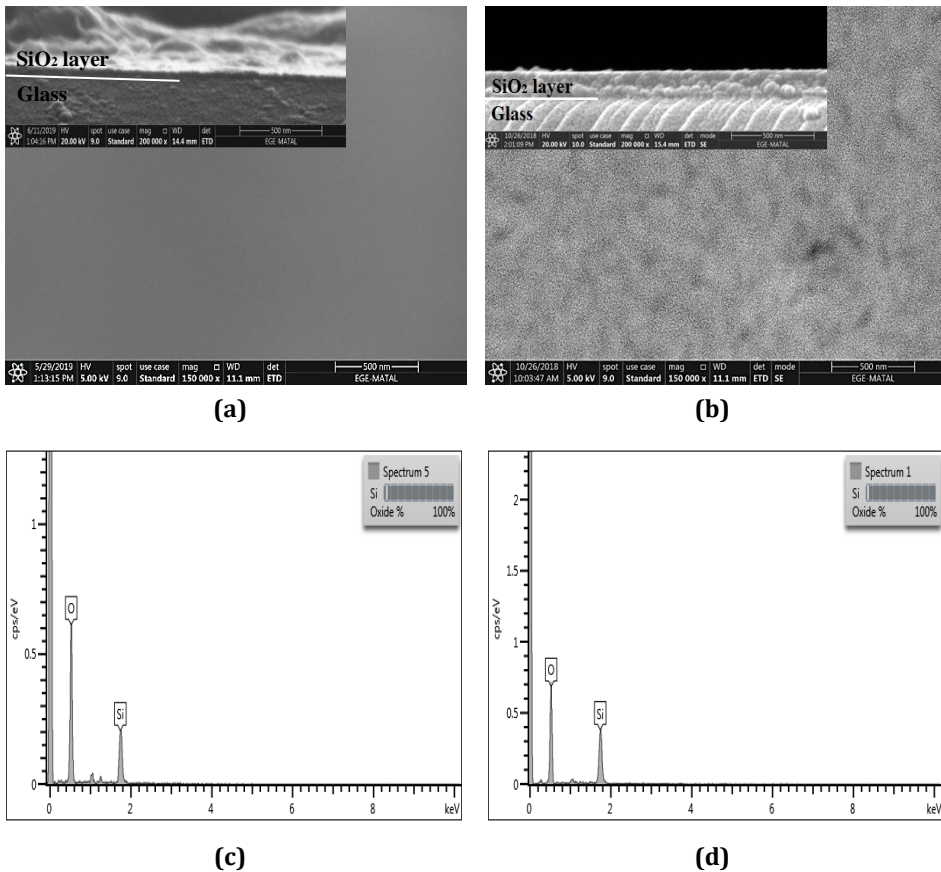

Fig. 1 SEM images of (a) acid-catalyzed and (b) base-catalyzed SiO$_2$ coatings (The insets show the cross-sectional views); and their corresponding EDS results in (c) and (d), respectively
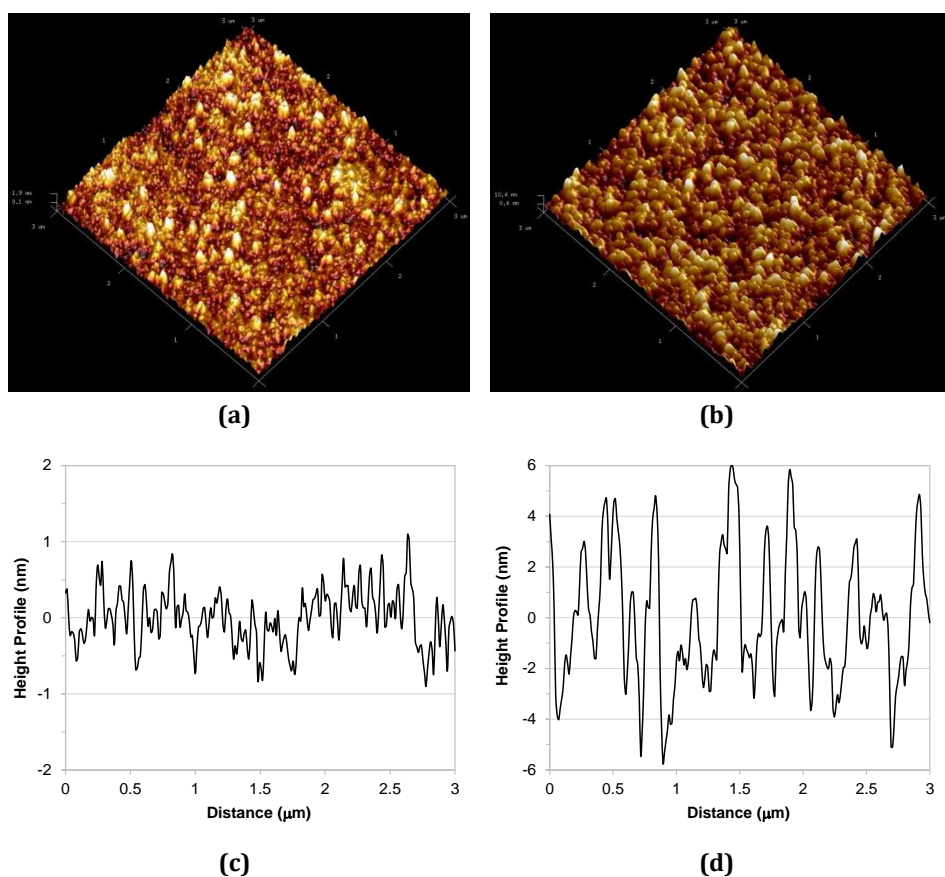
Fig. 2 3D AFM images of (a) acid-catalyzed and (b) base-catalyzed SiO₂ coatings and their cross-sectional scans of the surface profiles in (c) and (d), respectively

Chemical structure of SiO₂ films is confirmed with ATR-FTIR measurements and the results are given in Fig. 3 with the symbols showing the peak locations. Uncoated glass substrate (soda lime silica glass) shows two peaks at ~780-790 cm⁻¹ and ~900 cm⁻¹, indicating the symmetric stretching of Si–O–Si bonds and stretching vibrations of Si–OH bonds, respectively [21,29]. Beside peaks coming from the glass substrate, the most intense peak observed at 1060-1080 cm⁻¹ (indicating with an arrow) can be ascribed to the asymmetric stretching of Si–O–Si bonds [21,29]. The presence of this distinct absorption peak verifies the SiO₂ formation over the glass surface for both A-SiO₂ and B-SiO₂ coatings and its network structure, as also indicated by Qian et al. [21] and Ganbavle et al. [30]. Fig. 3 also shows that the intensity ratio of Si–O–Si to Si–OH peaks (at positions 1070 cm⁻¹ and 900 cm⁻¹) is higher for B-SiO₂ coatings than A-SiO₂ films, as also found by Vincent et al. [24]. They interpreted this ratio as an indication of the completion of the condensation reaction of silanol group (Si–OH) in SiO₂ films. Therefore it can be deduced that using a base catalyst increases the rate of condensation reaction of silanol group (Si–OH) to form siloxane groups (Si–O–Si) [22-25]. These findings verify that under the acid-catalyzed conditions, hydrolysis is fast and condensation is slow; on the other hand, the condensation rate is faster than hydrolysis rate under the base-catalyzed conditions [22,23,25,31]. Furthermore, the absence of peak at 1400 cm⁻¹ (bending of C–H bonds) in B-SiO₂ films implies the purity of the coatings since no residual ethoxy groups exist [19]. However, the

Fig. 2 3D AFM images of (a) acid-catalyzed and (b) base-catalyzed SiO_2 coatings and their cross-sectional scans of the surface profiles in (c) and (d), respectively

Chemical structure of SiO_2 films is confirmed with ATR-FTIR measurements and the results are given in Fig. 3 with the symbols showing the peak locations. Uncoated glass substrate (soda lime silica glass) shows two peaks at ~780-790 cm^{-1} and ~900 cm^{-1}, indicating the symmetric stretching of Si–O–Si bonds and stretching vibrations of Si–OH bonds, respectively [21,29]. Beside peaks coming from the glass substrate, the most intense peak observed at 1060-1080 cm^{-1} (indicating with an arrow) can be ascribed to the asymmetric stretching of Si–O–Si bonds [21,29]. The presence of this distinct absorption peak verifies the SiO_2 formation over the glass surface for both A-SiO_2 and B-SiO_2 coatings and its network structure, as also indicated by Qian et al. [21] and Ganbavle et al. [30]. Fig. 3 also shows that the intensity ratio of Si–O–Si to Si–OH peaks (at positions 1070 cm^{-1} and 900 cm^{-1}) is higher for B-SiO_2 coatings than A-SiO_2 films, as also found by Vincent et al. [24]. They interpreted this ratio as an indication of the completion of the condensation reaction of silanol group (Si–OH) in SiO_2 films. Therefore it can be deduced that using a base catalyst increases the rate of condensation reaction of silanol group (Si–OH) to form siloxane groups (Si–O–Si) [22-25]. These findings verify that under the acid-catalyzed conditions, hydrolysis is fast and condensation is slow; on the other hand, the condensation rate is faster than hydrolysis rate under the base-catalyzed conditions [22,23,25,31]. Furthermore, the absence of peak at 1400 cm^{-1} (bending of C–H bonds) in B-SiO_2 films implies the purity of the coatings since no residual ethoxy groups exist [19]. However, the

wide weak peak observed at 2985 cm^{-1} (asymmetric stretching of C–H bonds) in addition to the weak peak at 1400 cm^{-1} in A-SiO$_2$ coatings must be due to the unreacted TEOS precursor [19,30]. All these findings denote that SiO$_2$ reaction goes to the completion with a base catalyst under low drying temperatures [19].
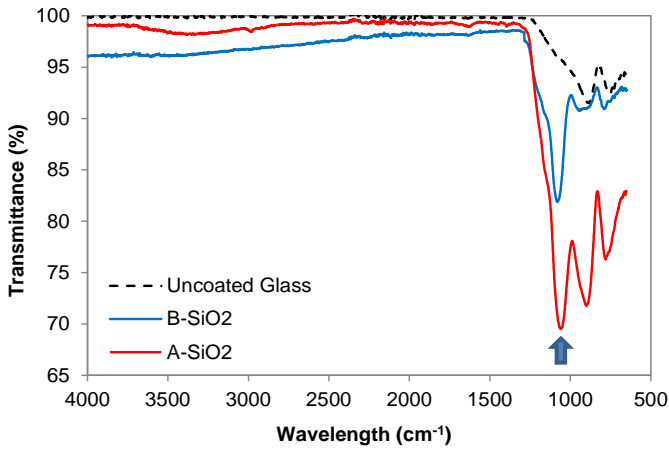

Fig. 3 FTIR spectra of uncoated and SiO$_2$ coated glass substrates

Optical transmittance (T) and reflectance (R) spectra of SiO$_2$ coatings obtained using both acid- and base-catalyzed sols are shown in Fig. 4(a) and (b), respectively. Single-layer SiO$_2$ coatings obviously increase the transmittance of the glass substrates for both catalysts when compared to uncoated one. Average transmittance of uncoated glass, in the whole visible light range of 400-800 nm, is calculated as 91%. Coating the glass surface with base-catalyzed SiO$_2$ film raises the average transmittance to 98.1% at this wavelength range but with acid-catalyzed SiO$_2$ film, only to 92.3%. In other words, ~7.1% increase in transmittance is gained with B-SiO$_2$ coating, compared to ~1.3% increase with A-SiO$_2$ coating. Substantially higher transmittance of B-SiO$_2$ film must be the results of its porous structure, as also confirmed by SEM and AFM images. It can be deduced that AR properties of glass is significantly enhanced by B-SiO$_2$ coatings. Fig. 4(b) also supports this inference. While ~9% of light is reflected from both sides of the air/uncoated glass interface in wavelength range of 400-800 nm, this average value can be reduced to 1.8% by coating the glass surface with B-SiO$_2$ film. Moreover, it can be lowered to even below 1% in the wavelength range of ~560-790 nm and to a lowest level of 0.4% at 655 nm. However, average reflectance value of glass can only be reduced to 7.7% by A-SiO$_2$ coating.

Glass substances coated with AR films attain zero-reflectivity in air medium if destructive interference can be created between light reflected from the coating/air interface and coating/glass interface. This condition can only be met if both refractive index and thickness of the applied coating are appropriately chosen [32]: (i). Refractive index value (n_c) of the coatings applied on glass surface should be between 1.21 and 1.25, as can be calculated from Eq. (1). (ii). thickness of coatings (d_c) should be adjusted so that destructive interference can occur at one quarter of the wavelength (λ) of incident light desired [32]:

$$d_c = (\lambda/4)/n_c \tag{5}$$

Reflectivity of base-catalyzed SiO$_2$ coating could be as low as 0.4% as shown in Fig. 4(b), so it can be inferred that, RI value of these coatings must be within 1.21-1.25 range. RI value of B-SiO$_2$ coating can be estimated using Eq. (5), considering the wavelength at minimum reflectance (λ = 655 nm) in Fig. 4(b) (or maximum transmittance in Fig. 4(a)), and its

coating thickness, $d_c \approx 140$ nm (from Fig. 1(b)). n_c is calculated as ~ 1.17, in agreement with the experimental n_c results of Xiao et al. [25], Suratwala et al. [19] and also Yan et al. [27] who used approximately the same molar ratio of components with this work. When compared to $n_c = 1.45$ of bulk SiO_2, this low RI value proves the porous nature of B-SiO_2 coatings. The base-catalyzed hydrolysis leads to bigger particle formation, as determined by AFM images. Void spaces are remained between these bigger particles during particle packing. A porous coating is finally formed at the end of gelation, where air can be entrapped within voids ($n_{air} \approx 1$), resulting in a lower refractive index compound, $n_c \sim 1.17$ [24,33,34]. On the contrary, tiny silica particles are obtained if an acid catalyst is used. When the particle size becomes smaller, void spaces between these particles decrease considerably during the particle packing. Hence, RI of this final dense film is high [24,33]. The reason of the very high transmittance values attained by B-SiO_2 coating compared to dense A-SiO_2 coating must be the lower refractive index of the base-catalyzed film. Therefore, this work is mainly focused on base-catalyzed SiO_2 coatings to achieve zero-reflectivity.
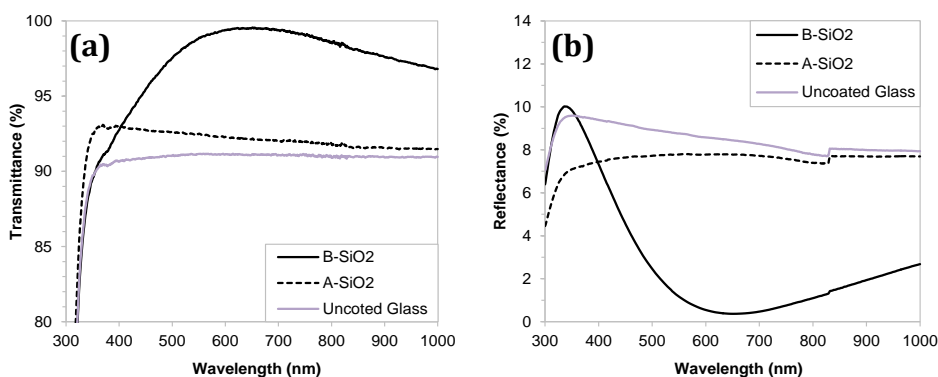

Fig. 4 Effect of catalyst type on (a) transmittance and (b) reflectance spectra of single-layer SiO_2 coatings (WS=120 mm/min)

Surface topography of the coatings must also be taken into consideration to prevent light scattering for attaining zero-reflectivity. A rough surface may lead to optical scattering loss in the transmitted light (transmission haze), especially if the magnitude of the surface roughness is close to the working wavelength of light [3,24,26,35]. Vincent et al. [24] calculated the scattering loss in transmitted light ($T_{diffuse}/T_{total}$ ratio at $\lambda = 550$ nm) caused by the surface roughness of their acid- ($R_q = 0.3$ nm) and base-catalyzed ($R_q = 4.5\text{-}16.2$ nm) silica films. No any significant surface light scattering was detected in their work and 0.67% maximally, for the base-catalyzed films having $R_q = 16.2$ nm. In addition, using the Rayleigh scattering model (roughness dimensions are lower than the wavelength of light), Mozumder et al. [3] evaluated Rayleigh scattering in the visible region (at $\lambda = 532$ nm) as negligible for silica ($n_c = 1.43$) surfaces if roughness is smaller than 100 nm. Since R_q roughness of both A-SiO_2 ($R_q = 0.5$ nm) and B-SiO_2 ($R_q = 2.9$ nm) coatings in this work is less than 3 nm, it can be inferred that, intensity of the scattering loss in transmitted light can be accepted as negligible in the working wavelength range of $\lambda = 400\text{-}800$ nm with these very small roughness values of either catalyst type [28,36]. The optical results of this work are the results of total light transmittance (or reflectance) measurements obtained by the integrating sphere attachment. Transmission haze, the percentage ratio of the diffusely (scattered) transmitted light to the total transmitted light ($T_{diffuse}/T_{total}$ or (T_{total}-T_{direct})/T_{total}), can be estimated if the intensity of the directly transmitted light values are known [35]. By this approximation, transmission haze is found as 0.4% and 0.9% for A-

SiO_2 and $B-SiO_2$ coatings, respectively, consistent with the roughness values. In addition, if the thickness of coatings is increased, a maximum haze of 1.1% is observed, showing the high direct transmittance and low transmission haze of the coatings [24,28,35,36].

3.1.2 Effect of Withdrawal Speed

Thickness of coating can be adjusted for minimum reflectivity by changing the withdrawal speed (WS) in the dip coating technique, keeping all other parameters constant. The effect of WS, ranging from 30 to 240 mm/min, on the optical properties of base-catalyzed SiO_2 coatings is shown in Fig. 5. Transmittance spectra in Fig. 5(a) show that $B-SiO_2$ coatings increase the transmittance of glass for all speeds. However, highest transmittance value (the maximum peak point of the broad spectrum) of 99.8% is reached at WS=90 mm/min. Withdrawal speeds >90 mm/min result in very slight decrease in maximum peak values, from 99.8% to 98.5%. In addition, maximum transmittance peak positions shift towards longer wavelengths with the increase in WS, as noted in Table 1. The red-shift in wavelengths for WS> 90 mm/min can be attributed to an increase in coating thickness, as also detected by Yuan et al. [37] in their working WS range of 48-120 mm/min for porous SiO_2 films and by many others [24,27,29,38]. Considering Eq. (5), this red-shift behavior must be the results of better matching between the refractive index ($n_c \sim 1.17$) and thickness of the coatings, d_c [38]. The theoretical thicknesses are calculated to satisfy the quarter-wave condition at wavelength of maximum transmittance [9,20,38,39]. The d_c results are given in Table 1 and the real film thicknesses measured from the SEM views are in good agreement with these computed d_c values with a maximum difference of 9 nm. The similarity between computed and measured thickness values for AR coatings is also confirmed by Prado et al. [38], Ye et al. [20] and, Han and Kim [39]. In addition, it is calculated that coating thickness increases with increasing WS (> 90) according to the relation, $d_c \sim WS^{0.5}$ (R^2=0.9942); in accordance with the thickness evolution of the dip-coated films (Theoretically at high withdrawal speeds, viscous drag forces is balanced with gravitational force in the thickness evolution) [17,40]. On the other hand for lower WS (≤ 60 mm/min), the resultant coatings must be too thin and probably more amorphous than the thicker films obtained at WS > 60 mm/min. This might be the reason of relatively lower transmittance values and inconsistency in peak positions at these low speeds. The same trends and findings are also detected in reflectance measurements given in Fig. 5(b). $B-SiO_2$ coatings significantly decrease the reflectance of glass and minimum reflectance values, changing from 0.3% at 90 mm/min to 0.6% at 240 mm/min, are achieved with a red-shift in the spectra. Hence, it is possible to obtain AR coatings having minimum reflectance at different wavelengths, which will be applicable to different optical end-uses. Effect of WS on acid-catalyzed SiO_2 films was also investigated but only 1.5% gain in transmittance was detected maximally.

Transmittance and reflectance values at 550 nm are drawn in Fig. 5(c) to compare the effectiveness of AR coatings in solar radiation spectrum, since 550 nm wavelength corresponds nearly to the maximum intensity of the solar radiation spectrum [34]. Transmittance increases with the increase in WS up to 90 mm/min, at which maximum transmittance of 99.8% coincides with transmittance at 550 nm wavelength. This value is higher than the transmittance values found in previous reports: e.g. 99% (λ=548 nm) obtained by Vincent et al. [24] at WS=85 mm/min, 99.4% (λ=500 nm) achieved by Prado et al. [38] at WS=150 mm/min, 97.5% (λ=500 nm) found by Mahadik et al. [36] at WS=80 mm/min and 98.78% (λ=550 nm) found by Xu et al. [34] at WS=162 mm/min. Although the coating parameters are too different in these studies, the coating thicknesses are varied between 100-110 nm. The SEM thickness of $B-SiO_2$ coating at 90 mm/min is measured as 108±5 nm. Hence, the very high transmittance value attained in this work must be the result of proper adjustment of the required thickness (Table 1) for maximum transmittance at 550 nm based on quarter-wavelength rule. Additionally, the roughness of

the B-SiO$_2$ coatings is negligibly small to create any scattering loss. With the increase in coating thickness further, WS > 90 mm/min, a nearly linear decrease in transmittance at 550 nm is observed; and it is reduced to 92.7% at 240 mm/min, still higher than that of uncoated glass. Reflectance values show the mirror-image similarity with the transmittance data. A minimum reflectance of ~0.3% is achieved at 90 mm/min and it increases linearly with the increase in WS.

Transmittance values at 550 nm are also compatible with their corresponding average values, calculated in the wavelength range of 400-800 nm and given in Table 1. High average transmittance values of 98.8-94.2% and also low average reflectance values of 1.2-5.1% verify the effectiveness of all B-SiO$_2$ coatings in the entire visible light range. Nevertheless, the films obtained by WS ≥ 150 mm/min will be more effective at longer wavelengths, as inferred from their higher average transmittance values than their transmittance values at 550 nm. Also, the significant red shift in wavelengths at maximum transmittance for WS ≥ 150 mm/min given in Table 1 substantiates this inference.

Table 1 Transmittance (T) values of single-layer B-SiO$_2$ coatings deposited at different withdrawal speeds

Coating Name	Withdrawal Speed (mm/min)	Maximum T (%)	Wavelength at Maximum T (nm)	Film Thickness (nm)	Average T at 400-800 nm range (%)
Uncoated Glass (G)	-	-	-	-	91.0
G/B-SiO$_2$	30	98.2	670	-	96.8
	60	98.7	610	-	98.0
	90	99.8	550	118	98.8
	120	99.5	655	140	98.1
	150	99.2	720	154	97.0
	180	99.3	790	169	95.9
	200	98.8	820	175	95.1
	240	98.5	890	190	94.2

On the whole, it can be deduced that WS of 90 and also 120 mm/min seem to be the optimum conditions for B-SiO$_2$ films because of their high transmittance values in terms of both average (98.1-98.8%) and maximum (99.5-99.8%). In terms of average, 7.8% gain at WS = 90 mm/min and 7.1% gain at WS = 120 mm/min shows their effectiveness in the whole visible light range. Furthermore, transmittance of these films is greater than 97% nearly in the entire visible light range and greater than 99% in the broad wavelength range of visible light (460-660 nm at 90 mm/min and 560-760 nm at 120 mm/min). The average transmittance values of 98.8-98.1% at 90-120 mm/min are greater than the average transmittance value of 96.6% at WS = 96mm/min in the work of Yuan et al. [37] corresponding to B-SiO$_2$ films of the same RI values.
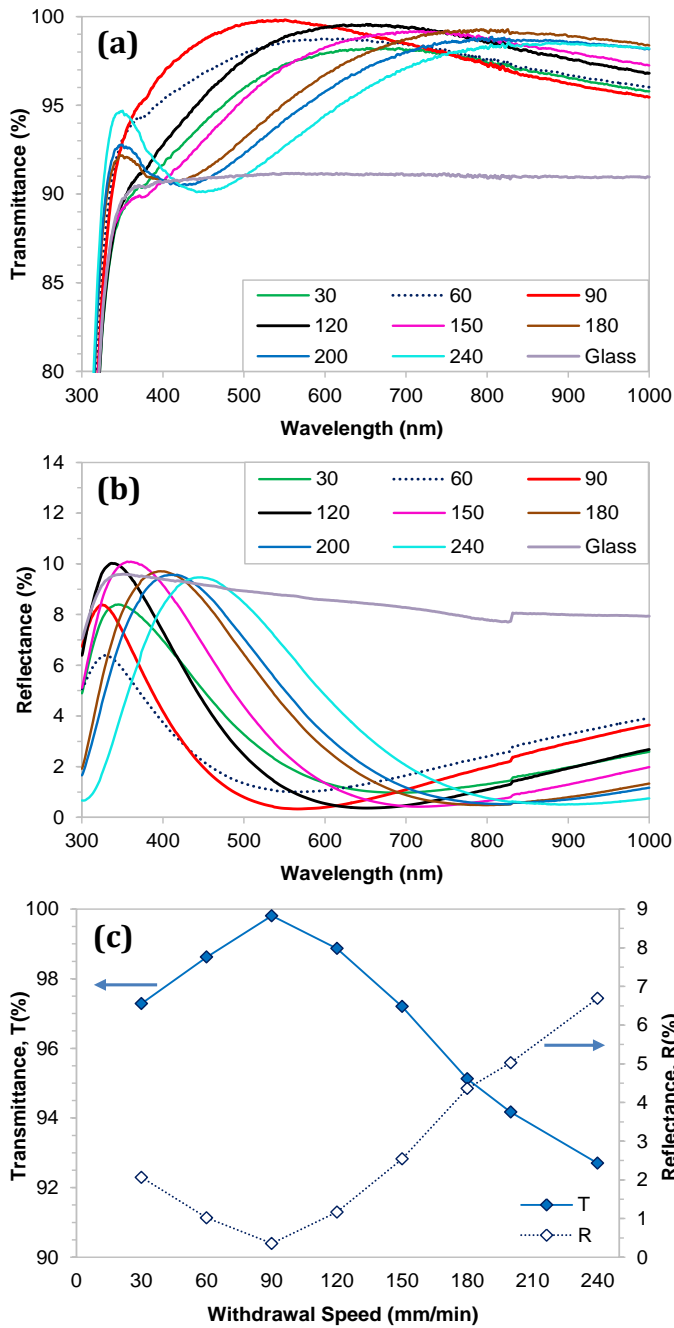
Fig. 5 AR performance of single-layer B-SiO₂ coatings obtained by different withdrawal speeds: (a) transmittance spectra; (b) reflectance spectra; (c) transmittance and reflectance values at 550 nm wavelength

3.2. Development of TiO$_2$ Coatings

Although base-catalyzed SiO$_2$ coatings improve the light transmittance of glass considerably, their durability is reported to be quite low because of their porous structure [31]. The connections between spherical particles within the porous film are all point-contacts, thus leading to low durability against scratches and environmental factors [26,31]. Moreover, as the pores get affected by humidity, optical properties of the porous film will get reduced by time [25,26]. Thus, AR coatings also have to possess high durability besides its AR properties for their usage especially in outdoor applications (e.g. solar collectors). In this work, it is aimed to protect porous silica layer from the external factors by coating it with a TiO$_2$ layer, which have excellent chemical and mechanical durability in addition to well-accepted self-cleaning and superhydrophilic features [32]. The only disadvantage of the TiO$_2$ film in AR applications is its high refractive index value, $n_c \approx 2.3$-2.5 [32,41], since the required condition given in Eq. (1) cannot be not satisfied. Therefore, at first, optimization of the dip-coating process parameters in single-layer TiO$_2$ film production is performed to maximize the transmittance, before being applied to the multiple coatings.

Transmittance change of TiO$_2$ films obtained from the sols with different titanium concentrations is shown in Figs. 6(a) with respect to withdrawal speed (Transmittance spectra of TiO$_2$ coating for WS = 90 and 120 mm/min are given in Fig. 9). TiO$_2$ film layer reduces the transmittance of glass substrate remarkably below to its uncoated level. Since acid-catalyzed sols are used in TiO$_2$ deposition, the final dense film must be the reason of low transmittance values. The same results were also found by Miao et al. [41] and they attributed this decline to dense and non-porous film structure of TiO$_2$. Maximum transmission of light is found at WS = 60-120 mm/min range for all titanium concentrations but the highest at 90 mm/min. Transmittance tends to diminish with further increase in WS (i.e. coating thickness), because of the higher light absorption capacity of the thicker films. An increase in titanium concentration also causes an increase in film thickness [42], so, a further fall in the transmittance of films is detected for [Ti] = 0.2 M sols. Maximum transmittance of 87.4% is achieved at 0.1 M titanium concentration corresponding to a film thickness of 28±4 nm, while it falls to 80.1% at 0.2 M case and even up to 70% at 0.3 M (data not shown here). Parado et al. [38] found transmittance of 41 nm thick dense titania films (WS=150 mm/min) as 79% at 550 nm, by using nearly the same sol composition of [Ti]=0.2 M. Higher titanium concentration of 0.9 M was studied by Touam et al. [43] for three different WS of 10, 20 and 30 mm/min. They obtained only a slight increase with the increase in WS, but transmittance at λ=550 nm is measured as ~68% for these thick (80-123 nm) titania films. Mohallem et al. [44] investigated the optical transmittance of TiO$_2$ films for low withdrawal speeds of 12-90 mm/min. The thickness of their films were changed from 40 to 800 nm, depending on the WS, but none of their film achieved to reach over the transmittance of glass (~78% at λ=550 nm for 40 nm thick TiO$_2$ films). The results of this work are in good agreement with the previous findings, and transmittance enhancement up to 87.4% is attained by decreasing titanium concentration to 0.1 M and WS to 90 mm/min.

The effect of dwell time at constant WS (120 mm/min) is also investigated, as shown in Fig. 6(b). The substrates are immersed in the sol and allowed for different durations to be completely wetted by the sols before taken out. Extending dwell time does not give much change to the final transmittance of the TiO$_2$ coatings. However, it is selected as 10 min to ensure that glass surface is uniformly wetted by the sol all over the entire surface.
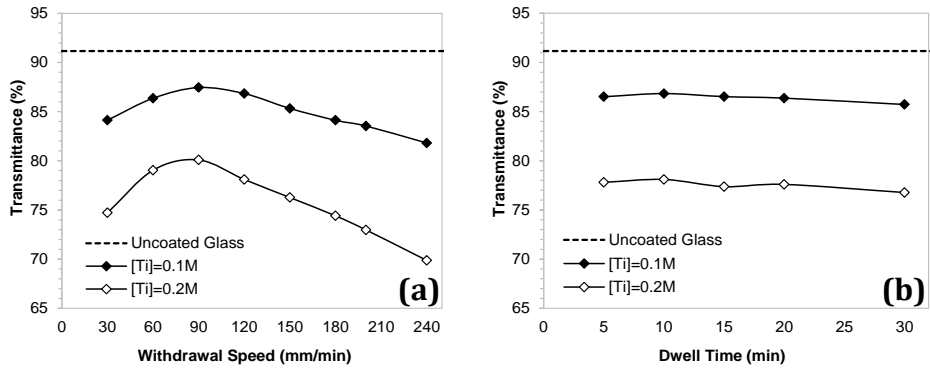
Fig. 6 Transmittance values at 550 nm wavelength of single-layer TiO_2 coatings obtained by different (a) withdrawal speeds, and (b) dwell time
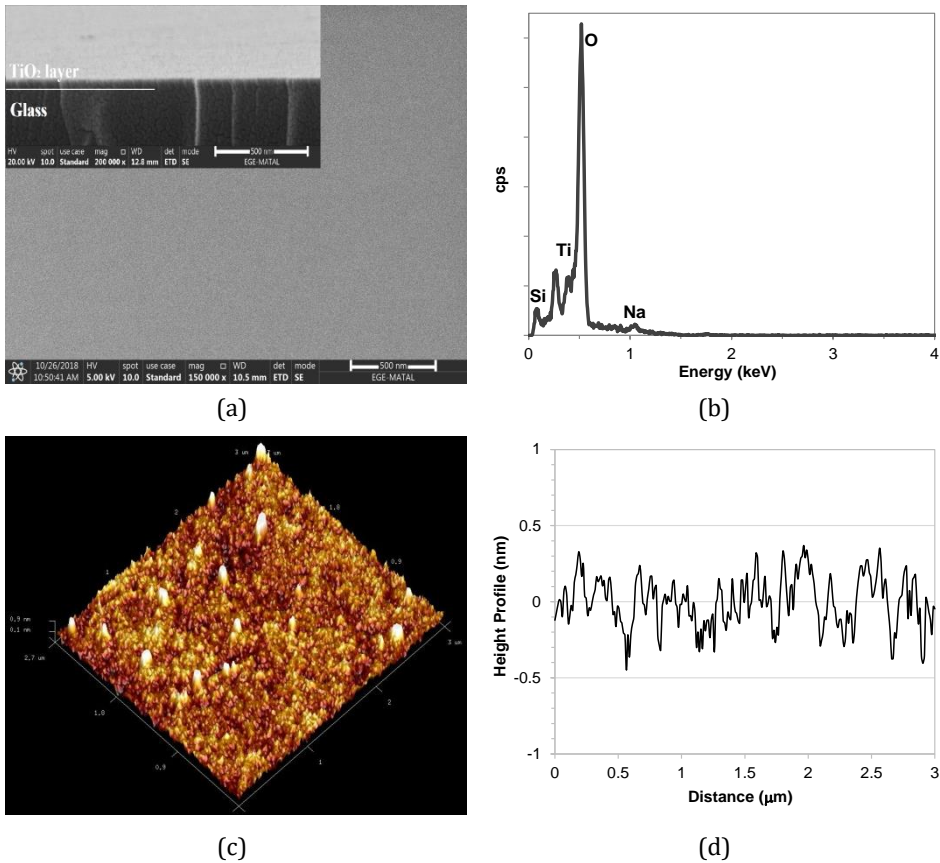

Fig. 7 SEM (a,b) and AFM (c,d) analysis of TiO_2 coatings (WS=120 mm/min): (a) Top view SEM image (inset: cross-sectional view), (b) EDS result, (c) 3D AFM images, (d) AFM cross-sectional scan

SEM view of the TiO_2 coatings, obtained from the sol having 0.1 M titanium concentration, is given in Fig. 7(a). The SEM image verifies a dense, smooth and non-porous film formation over the glass surface. The cross-sectional view of the coatings, represented in Fig. 7(a) as an inset, points out a very thin continuous TiO_2 film formation. The thickness of the film is measured as 34 ± 4 nm for WS=120 mm/min. EDS measurement given in Fig. 7(b) demonstrates the titanium and oxygen existence in the coatings. Since TiO_2 film is too thin, additional peaks (like Si, Na) coming from the glass surface are also detected. FTIR spectra of TiO_2 coatings show the only peaks belonging to the glass substrate, since the characteristic Ti–O bond at around 500-600 cm^{-1} wavelength range is out of the measurement range (650-4000 cm^{-1}) of the ATR-FTIR (used for film samples) instrument. X-ray diffraction measurements of TiO_2 films are also conducted; however, no peaks could be detected in the XRD pattern. The absence of peaks must be the result of amorphous structure of TiO_2 films. The similar phenomena are also observed in the XRD analysis of the SiO_2 films. Touam et al. [43] for TiO_2 films and also Mahadik et al. [36] for SiO_2 films could not be detected any peaks in their XRD analysis. They attributed the absence of peaks to the amorphous nature of the resultant films.

AFM results confirm the SEM observations. 3D AFM image presented in Fig. 7(c) shows that the surface of the coating is very smooth and covered by tiny particles. The *Rq* roughness of the film is only 0.24 nm, even smaller than the dense A-SiO_2 films, probably due to high acid concentration of titanium sols. A representative line scan of this surface is illustrated in Fig. 7(d). The height profile fluctuations of the coatings changes only within the ±0.5 nm range (Fig. 2(c)), verifying the smoothness of the surface. As the details are given in Section 3.1.1, acid-catalyzed reactions lead to the growth of linearly or randomly branched polymeric particle chains with fast hydrolysis and slow condensation [31,43]. Therefore, the resultant film has a dense structure. These results are in good agreement with several works reported in the literature [20,31,42-44].

3.3. Development of Double-Layer Coatings

Double-layer AR coatings, SiO_2/TiO_2, are produced by coating the antireflective B-SiO_2 layer with TiO_2 layer. The thickness of outer TiO_2 layer is altered by depositing from sols with different titanium concentrations (0.1 M or 0.2 M). Transmittance change of the resultant double-layer coatings at 550 nm wavelength are drawn in Fig. 8 together with their corresponding single-layer coatings. When porous B-SiO_2 film is coated with 34 ± 4 nm thick TiO_2 films, corresponding to 0.1 M titanium sol concentration, transmittance of the resultant stack falls in between to that of single-layer B-SiO_2 and single-layer TiO_2 (0.1 M). Although transmittance of B-SiO_2/TiO_2 (0.1 M) double-layer coatings falls short of the single-layer B-SiO_2 coatings (from 98.9% to 96.3%), B-SiO_2/TiO_2 (0.1 M) system improves the transmittance of glass considerably, ~5% gain. When the thickness of TiO_2 layer is increased to 49 ± 3 nm in B-SiO_2/TiO_2 system by using 0.2 M titanium concentration, transmittance decreases further to 85.8%, which is quite below than that of uncoated glass (91.2%). Lari et al. [45] observed a decline in transmittance of glass to ~89.8% at 550-630 nm range, by coating with SiO_2/porous-TiO_2 double-layer system (WS=25 mm/min) having nearly the same thickness of layers, 150 nm/30 nm, of this work. Miao et al. [41] attained 3.4% gain in transmittance in 400-800 nm range using a porous TiO_2 outer layer in their porous-SiO_2/porous-TiO_2 (48.6 nm/22.5 nm) system. Kesmez et al. [42] also produced SiO_2/TiO_2 coatings with 4-5% gain in transmittance of glass. Hence, ~5% achievement with a dense TiO_2 film can be considered as a good result when compared to previous SiO_2/TiO_2 studies even possessing an outer porous TiO_2 layer. This high gain must be the results of using a very thin TiO_2 layer above the porous SiO_2 layer having very high transmittance [41]. Kesmez et al. [42] emphasized that TiO_2 thickness should be kept as low as possible by decreasing the Ti concentration in order to preserve the AR properties of SiO_2 layer. Furthermore, the results of Ramirez-Garcia et al. [46] showed that outer TiO_2

layer of very small thickness (20-50 nm) still gives improved abrasion resistance and lower transmission haze to the resultant SiO_2/TiO_2 bilayers. If dense $A-SiO_2$ film is used in the double-layer system, transmittance of the resultant stack falls to 87.1% by coating with 0.1 M TiO_2 layer and further to 77.1% by coating with 0.2 M TiO_2 layer. It can be deduced that, no any improvement in transmittance of glass could be obtained with $A-SiO_2/TiO_2$ double-layer system when nonporous, dense structures are used in both layers. Thus, the introduction of nano pores into the structure seems to be a requisite for higher optical properties.
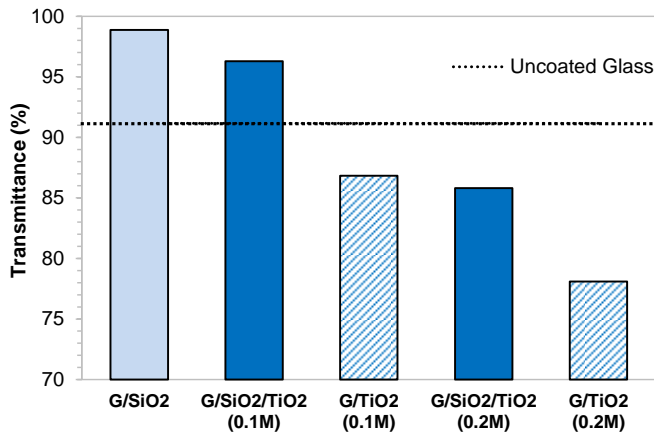

Fig. 8 Transmittance values at 550 nm wavelength of single- and double-layer coatings, obtained by using base-catalyzed SiO_2 film as the inner layer (WS=120 mm/min; the values in parenthesis denote the titanium concentration in TiO_2 sols)

Thickness of each layer in the $B-SiO_2/TiO_2$ (0.1M) system is varied by differentiating the withdrawal speeds to investigate any further improvement in transmittance. The results at 550 nm wavelength are given in Table 2. When $B-SiO_2$ layer is deposited at WS of 90 mm/min ($d_c \approx 108\pm5$ nm), as in 90/90 (T=94.3%) and 90/120 (T=93.9%) coatings, transmittance nearly remains constant with the change in TiO_2 film thickness. The single-layer thicknesses of TiO_2 films are 28±4 nm and 34±4 nm for WS = 90 and 120 mm/min, respectively. Nonetheless, when $B-SiO_2$ layer is coated at 120 mm/min speed ($d_c \approx 140\pm4$ nm), highest transmittance of 96.3% is achieved if TiO_2 layer is also coated as thick with 120 mm/min. Another point of view is that, if the outer TiO_2 layer is applied as thick (as in 90/120 and 120/120 coatings), the inner $B-SiO_2$ layer must be thick also, and vice versa. These results imply that the light waves reflected from the interfaces of the layers interfere destructively mainly in the 120/120 coatings, that is, by the thicknesses of layers obtained at WS=120 mm/min. The thickness of each layer in 120/120 double-layer system is measured using the cross-sectional SEM views, and are found as ~138 nm and ~37 nm for $B-SiO_2$ and TiO_2 layers, respectively. The results are compatible with the single-layer thickness measurements. In addition, the existence of silicon and titanium atoms in the double-layer coatings is confirmed with EDX analysis, performed at the same time with SEM measurements.

The AR performance of the $B-SiO_2/TiO_2$ double-layer coatings in the whole visible light range (400–800 nm) is evaluated with the transmittance spectra given in Fig. 9, with their corresponding single-layer coatings for comparison. Transmittance of single-layer dense TiO_2 coatings is significantly lower than that of uncoated glass in the entire range. However, the inclusion of an inner $B-SiO_2$ layer beneath the TiO_2 coatings results in highly effective double-layer coatings. Although their transmittance is not as high as that of

single-layer B-SiO₂ films, AR characteristics of the inner SiO₂ layer are still preserved. B-SiO₂/TiO₂ coated glass, of each layer deposited at 120mm/min, transmits light higher than the uncoated glass in the whole measurement range. Moreover, transmittance ≥96% is achieved for wavelengths >530 nm and 98% transmittance is obtained maximally at $\lambda = 750$ nm. When the WS of TiO₂ film is decreased to 90 mm/min, transmittance of 120/90 coatings reaches over to that of uncoated glass after $\lambda > 450$ nm but is still lower than that of 120/120 coatings for all wavelengths. The same phenomena are also observed in 90/90 and 90/120 coatings if thinner B-SiO₂ films of 90 mm/min is used.

Table 2 Transmittance (T) values of single- and double-layer coatings deposited at different withdrawal speeds

Coating Name	Withdrawal Speed, (mm/min)		T at 550 nm, (%)	Average T at 400-800 nm range, (%)
	B-SiO₂ Layer	TiO₂ Layer		
G (Uncoated Glass)	-	-	91.2	91.0
G/SiO₂/TiO₂ (90/90)	90	90	94.3	94.4
G/SiO₂/TiO₂ (90/120)	90	120	93.9	94.1
G/SiO₂/TiO₂ (120/90)	120	90	93.8	94.1
G/SiO₂/TiO₂ (120/120)	120	120	96.3	96.2

The average transmittance of coatings at 400–800 nm wavelength range is also calculated and given in Table 2. Average values are in consistency with the values at 550 nm. Table 2 points out that, all double layer coatings bring about an average of 3-5% gain in transmittance to glass slides in the whole visible range. Moreover, in the broad range of wavelength from ~500 to 800 nm, an average gain of 6% (or T ≥ 97.2%) and 7% gain maximally is achieved with the 120/120 coatings, while an average gain of 4% (or T ≥ 95.1%), with all other double-layer coatings. In addition to solar applications [3], transmittance improvement in this wavelength range is also important in the development of high power laser systems [26].
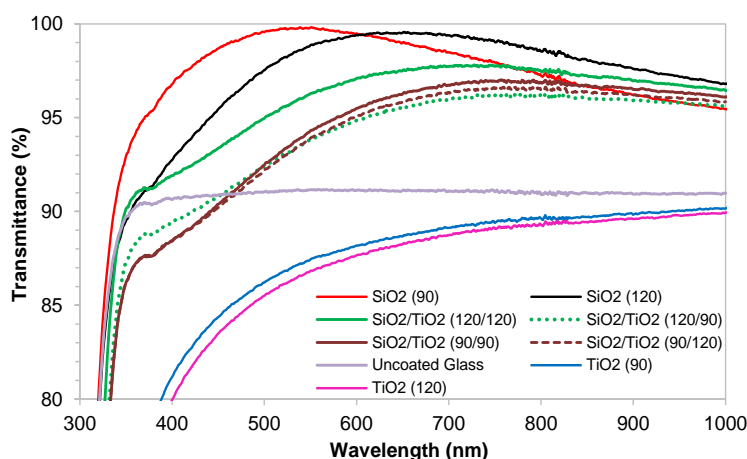

Fig. 9 Transmittance spectra of single- and double-layer coatings (values in parenthesis are the WS of each layer)

4. Conclusion

Single- and double-layer antireflective coatings are developed using sol-gel and dip coating methods to function in the whole visible light range of 400-800 nm. SiO_2 is used as the AR layer and TiO_2 is selected to perform as a protective coating. At first, the optimized conditions in the deposition of single-layer films are determined; then, double-layer coatings of SiO_2/TiO_2 are developed by taking these optimized conditions into account to achieve a high transmittance.

Effect of catalyst type of silica sols (for the porosity change), and also withdrawal speed (for the thickness change) are investigated in the deposition of single-layer SiO_2 films. It is found that, base catalysts gives rise to the formation of a porous $B-SiO_2$ film, so leading to a decrease in the refractive index value up to ~ 1.17. Hence, an average of 7-8% gain in transmittance in 400-800 nm range is achieved with $B-SiO_2$ films when compared to uncoated glass. The results also show that the maximum transmittance of 99.8-99.0% at 550 nm is achieved at 90-120 mm/min speeds corresponding to a coating thickness of $\sim 110-140$ nm. Moreover, $B-SiO_2$ coatings with maximum transmittance working at different wavelengths can be achieved by increasing coating thicknesses further. On the other hand, acid-catalyzed $A-SiO_2$ coatings have dense structures, resulting in a slight increase in transmittance (only 1-2% gain).

AR coatings have to possess high durability besides their AR properties for the usage in outdoor applications. For this reason, double-layer AR coatings are prepared by covering inner $B-SiO_2$ layer with an outer TiO_2 film, since the excellent chemical and mechanical durability of TiO_2 is well-accepted in the literature. The inclusion of a nonporous and high RI TiO_2 coating leads to a decrease in transmittance, compared to single-layer $B-SiO_2$ coatings. However, adjustment of thickness of each layer (to create destructive interference) and the usage of porous SiO_2 film as the inner layer, allow SiO_2/TiO_2 coatings to transmit light higher than the uncoated glass. 5-6% achievement in transmittance of glass, in the whole visible range of 400-800 nm, shows that these coatings can be used in solar energy systems such as glass covers of solar collectors and photovoltaic panels; and also be used in the development of high power laser systems. In addition, these AR coatings can be applied to the all type of transparent surfaces since this production method do not require high temperatures. This work only focuses on the optical properties of double-layer coatings, their durability is under investigation.

Acknowledgements

References

[1] Huang X, Yuan Y, Liu S, Zhang L, Hong R. Preparation of hydrophobic broadband antireflective SiO2coating on flexible poly(methyl methacrylate) substrates. Colloids and Surfaces A: Physicochemical and Engineering Aspects, 2018; 538: 519 - 525. https://doi.org/10.1016/j.colsurfa.2017.11.027

[2] Agustín-Sáenz C, Machado M, Tercjak A. Antireflective mesoporous silica coatings by optimization of water content in acid-catalyzed sol-gel method for application in glass covers of concentrated photovoltaic modules. Journal of Colloid and Interface Science, 2019; 534: 370 - 380. https://doi.org/10.1016/j.jcis.2018.09.043

[3] Mozumder MS, Mourad A-H I, Pervez H, Surkatti R. Recent developments in multifunctional coatings for solar panel applications: A review. Solar Energy Materials and Solar Cells, 2019; 189: 75 - 102. https://doi.org/10.1016/j.solmat.2018.09.015

[4] Ye H, Zhang X, Zhang Y, Ye L, Xiao B, Lv H, Jiang B. Preparation of antireflective coatings with high transmittance and enhanced abrasion-resistance by a base/acid two-step catalyzed sol-gel process. Solar Energy Materials & Solar Cells, 2011; 95: 2347 - 2351. https://doi.org/10.1016/j.solmat.2011.04.004

[5] Grosjean A, Soum-Glaude A, Neveu P, Thomas L. Comprehensive simulation and optimization of porous SiO2 antireflective coating to improve glass solar transmittance for solar energy applications. Solar Energy Materials and Solar Cells, 2018; 182: 166 - 177. https://doi.org/10.1016/j.solmat.2018.03.040

[6] Xu YJ, Liao JX, Cai QW, Yang XX. Preparation of a Highly-Reflective TiO2/SiO2/Ag Thin Film with Self-Cleaning Properties by Magnetron Sputtering for Solar Front Reflectors. Solar Energy Materials & Solar Cells, 2013; 113: 7 - 12. https://doi.org/10.1016/j.solmat.2013.01.034

[7] Huang WH, Lin CS. Robust superhydrophobic transparent coatings fabricated by a low-temperature sol-gel process. Applied Surface Science, 2014; 305: 702 - 709. https://doi.org/10.1016/j.apsusc.2014.03.179

[8] Raut HK, Ganesh VA, Nair AS, Ramakrishna S. Anti-reflective coatings: A critical, in-depth review. Energy Environ. Sci., 2011; 4: 3779 - 3804. https://doi.org/10.1039/c1ee01297e

[9] Priyadarshini BG, Sharma AK. Design of multi-layer anti-reflection coating for terrestrial solar panel glass. Bull. Mater. Sci., 2016; 39(3): 683 - 689. https://doi.org/10.1007/s12034-016-1195-x

[10] Kavaklı İ.G., Kantarlı K. Single and Double-Layer Antireflection Coatings on Silicon. Turkish Journal of Physics, 2002; 26: 349 - 354.

[11] Biswas PK, Sujatha Devi P, Chakraborty PK, Chatterjee A, Ganguli D. Porous Anti-Reflective Silica Coatings with a High Spectral Coverage by Sol-Gel Spin Coating Technique. Journal of Materials Science Letters, 2003; 22: 181 - 183. https://doi.org/10.1023/A:1022241707860

[12] Atkinson C, Sansom CL, Almond HJ, Shaw CP. Coatings for concentrating solar systems - A review. Renewable and Sustainable Energy Reviews, 2015; 45: 113 - 122. https://doi.org/10.1016/j.rser.2015.01.015

[13] Nagamedianova Z, Ramirez-Garcia RE, Flores-Arevalo SV, Miki-Yoshida M, Arroyo-Ortega M. Solar heat reflective glass by nanostructured sol-gel multilayer coatings. Optical Materials, 2011; 33: 1999 - 2005. https://doi.org/10.1016/j.optmat.2011.04.006

[14] Vicente GS, Bayon R, German N, Morales A. Long-term durability of sol-gel porous coatings for solar glass covers. Thin Solid Films, 2009; 517: 3157 - 3160. https://doi.org/10.1016/j.tsf.2008.11.079

[15] Chen D, Yan Y, Westenberg E, Niebauer E, Sakaitani N, Chaudhuri SR. Development of Anti-Reflection (AR) Coating on Plastic Panels for Display Applications. Journal of Sol-Gel Science and Technology, 2000; 19: 77 - 82. https://doi.org/10.1023/A:1008714205813

[16] Ennaceri H, Erfurt D, Wang L, Köhler T, Taleb A, Khaldoun A, El Kenz A, Benyoussef A, Ennaoui A. Deposition of multifunctional TiO2 and ZnO top-protective coatings for CSP application. Surface & Coatings Technology, 2016; 298: 103 - 113. https://doi.org/10.1016/j.surfcoat.2016.04.048

[17] Zhang W, Tu J, Long W, Lai W, Sheng Y, Guo T. Preparation of SiO2 anti-reflection coatings by sol-gel method. Energy Procedia, 2017; 130: 72 - 76. https://doi.org/10.1016/j.egypro.2017.09.398

[18] Zhang H, Fan D-W, Yu T-Z, Wang C-L. Antireflective and Self-cleaning Properties of SiO2/TiO2 Double-Layer Films Prepared by Cost-Effective Sol-Gel Process. Chinese Journal of Chemical Physics, 2015; 28: 777 - 780. https://doi.org/10.1063/1674-0068/28/cjcp1504074

[19] Suratwala TI, Hanna ML, Miller EL, Whitman PK, Thomas IM, Ehrmann PR, Maxwell RS, Burnham AK. Surface chemistry and trimethylsilyl functionalization of Stöber silica sols. Journal of Non-Crystalline Solids, 2003; 316: 349 - 363. https://doi.org/10.1016/S0022-3093(02)01629-0

[20] Ye L, Zhang Y, Zhang X, Hu T, Ji R, Ding B, Jiang B. Sol-gel preparation of SiO2/TiO2/SiO2-TiO2 broadband antireflective coating for solar cell cover glass. Solar Energy Materials & Solar Cells, 2013; 111: 160 - 164. https://doi.org/10.1016/j.solmat.2012.12.037

[21] Qian Z, Wang S, Ye X, Liu Z, Wu Z. Corrosion resistance and wetting properties of silica-based superhydrophobic coatings on AZ31B Mg alloy surfaces. Applied Surface Science, 2018; 453: 1 - 10. https://doi.org/10.1016/j.apsusc.2018.05.086

[22] Thomas IM. Methods for the preparation of porous silica antireflection coatings varying in refractive index from 1.22 to 1.44. Applied Optics, 1992; 31(28): 6145 - 6149. https://doi.org/10.1364/AO.31.006145

[23] Wu G, Wang J, Shen J, Yang T, Zhang Q, Zhou B, Deng Z, Fan B, Zhou D, Zhang F. A novel route to control refractive index of sol-gel derived nano-porous silica films used as broadband antireflective coatings. Materials Science and Engineering, 2000; B78: 135 - 139. https://doi.org/10.1016/S0921-5107(00)00529-8

[24] Vincent A, Babu S, Brinley E, Karakoti A, Deshpande S, Seal S. Role of catalyst on refractive index tunability of porous silica antireflective coatings by sol-gel technique. Journal of Physical Chemistry C, 2007; 111: 8291 - 8298. https://doi.org/10.1021/jp0700736

[25] Xiao Y, Shen J, Xie Z, Zhou B, Wu G. Microstructure Control of Nanoporous Silica Thin Film Prepared by Sol-Gel Process. J. Mater. Sci. Technol., 2007; 23(4): 504 - 508.

[26] Li X, Shen J. A scratch-resistant and hydrophobic broadband antireflective coating by sol-gel method. Thin Solid Films, 2011; 519: 6236 - 6240. https://doi.org/10.1016/j.tsf.2011.03.114

[27] Yan G, Yuan Y, Hong R. Preparation of broadband antireflective coatings with ultra-low refractive index layer by sol-gel method. Construction and Building Materials, 2018; 176: 75 - 80. https://doi.org/10.1016/j.conbuildmat.2018.05.016

[28] Wang J, Yang C, Liu Y, Zhang C, Zhang C, Wang M, Zhang J, Cui X, Ding R, Xu Y. Broadband antireflective double-layer mesoporous silica coating with strong abrasion-resistance for solar cell glass. RSC Adv., 2016; 6: 25191 - 25197. https://doi.org/10.1039/C6RA02281B

[29] Nielsen KH, Orzol DK, Koynov S, Carney S. Large area, low cost anti-reflective coating for solar glasses. Solar Energy Materials & Solar Cells, 2014; 128: 283 - 288. https://doi.org/10.1016/j.solmat.2014.05.034

[30] Ganbavle VV, Bangi UKH, Latthe SS, Mahadik SA, Rao AV. Self-cleaning Silica Coatings on Glass by Single Step Sol-gel Route. Surface & Coatings Technology, 2011; 205: 5338 - 5344. https://doi.org/10.1016/j.surfcoat.2011.05.055

[31] Wang X, Shen J. Sol-gel derived durable antireflective coating for solar glass. Journal of Sol-Gel Sci. Technology, 2010; 53: 322 - 327. https://doi.org/10.1007/s10971-009-2095-y

[32] Yao L, He J. Recent progress in antireflection and self-cleaning technology - From surface engineering to functional surfaces. Progress in Materials Science, 2014; 61: 94 - 143. https://doi.org/10.1016/j.pmatsci.2013.12.003

[33] Choi J, Han K, Kim JK. Enhanced Near Infrared Reflectance of TiO2/SiO2/TiO2 Multilayer Structure Using a Base-catalyzed SiO2 Film. Thin Solid Films, 2014; 569: 100 - 103. https://doi.org/10.1016/j.tsf.2014.08.036

[34] Xu J, Liu Y, Du W, Lei W, Si X, Zhou T, Lin J, Peng L. Superhydrophobic silica antireflective coatings with high transmittance via one-step sol-gel process. Thin Solid Films, 2017; 631: 193 - 199. https://doi.org/10.1016/j.tsf.2017.03.005

[35] Zhao L, Strobach E, Bhatia B, Yang S, Leroy A, Zhang L, Wang AN. Theoretical and experimental investigation of haze in transparent aerogels. Optics Express, 2019; 27: A39 - A50. https://doi.org/10.1364/OE.27.000A39

[36] Mahadik DB, Lakshmi RV, Barshilia HC. High performance single layer nano-porous antireflection coatings on glass by sol-gel process for solar energy applications. Solar Energy Materials & Solar Cells, 2015; 140: 61 - 68. https://doi.org/10.1016/j.solmat.2015.03.023

[37] Yuan Y, Lu X, Yan G, Hong R. Sol-gel preparation of antireflective coatings with abrasion resistance by base/acid double catalysis and surface treatment. Solar Energy, 2017; 155: 1366 - 1372. https://doi.org/10.1016/j.solener.2017.08.003

[38] Prado R, Beobide G, Marcaide A, Goikoetxea J, Aranzabe A. Development of Multifunctional Sol-Gel Coatings: Anti-reflection Coatings with Enhanced Self-Cleaning Capacity. Solar Energy Materials & Solar Cells, 2010; 94: 1081 - 1088. https://doi.org/10.1016/j.solmat.2010.02.031

[39] Han K, Kim JH. Reflectance modulation of transparent multilayer thin films for energy efficient window applications. Materials Letters, 2011; 65: 2466 - 2469. https://doi.org/10.1016/j.matlet.2011.05.006

[40] Hwang J, Shoji N, Endo A, Daiguji H. Effect of Withdrawal Speed on Film Thickness and Hexagonal Pore-Array Dimensions of SBA-15 Mesoporous Silica Thin Film. Langmuir, 2014; 30: 15550 - 15559. https://doi.org/10.1021/la5037713

[41] Miao L, Su LF, Tanemura S, Fisher CAJ, Zhao LL, Liang Q, Xu G. Cost-effective nanoporous SiO2-TiO2 coating on glass substrates with antireflective and self-cleaning properties. Applied Energy, 2013; 112: 1198 - 1205. https://doi.org/10.1016/j.apenergy.2013.03.043

[42] Kesmez Ö, Çamurlu HE, Burunkaya E, Arpaç E. Sol-gel preparation and characterization of anti-reflective and self-cleaning SiO2-TiO2 double-layer nanometric films. Solar Energy Materials & Solar Cells, 2009; 93: 1833 - 1839. https://doi.org/10.1016/j.solmat.2009.06.022

[43] Touam T, Atoui M, Hadjoub I, Chelouche A, Boudine B, Fischer A, Boudrioua A, Doghmane A. Effects of dip-coating speed and annealing temperature on structural, morphological and optical properties of sol-gel nano-structured TiO2 thin films. The European Physical Journal of Applied Physics, 2014; 67: 30302. https://doi.org/10.1051/epjap/2014140228

[44] Mohallem NDS, Viana MM, Lopes de Jesus MA, Moraes, Gomes GHM, Lima LFS, Alves EDL. Pure and Nanocomposite Thin Films Based on TiO2 Prepared by Sol-Gel Process: Characterization and Applications, Titanium Dioxide- Material for a Sustainable Environment, Edt. Dongfang Yang, IntechOpen, 2018. https://doi.org/10.5772/intechopen.74335

[45] Lari N, Ahangarani S, Shanaghi A. Effect of Different TiO2-SiO2 Multilayer Coatings Applied by Sol-Gel Method on Antireflective Property. Journal of Materials Engineering and Performance, 2015; 24: 2645 - 2652. https://doi.org/10.1007/s11665-015-1547-5

[46] Ramírez-García RE, Perez-Garcia SAA, Gonzalez-Rodriguez JA, Arroyo-Ortega M, Licea-Jimenez L. Engineered TiO2 and SiO2-TiO2 Films on Silica Coated Glass for Increased Thin Film Durability Under Abrasive Conditions. International Journal of Applied Ceramic Technology, 2017; 14: 39-49. https://doi.org/10.1111/ijac.12614

Research Article

A research on effect of process parameters on mechanical properties of B₄C reinforced aluminum matrix composites fabricated by mechanical milling and hot press sintering route

Mutlu Karasoglu*[1,a], Serdar Karaoglu[2,b], Taylan Sinan[2,c], Tugce Tekin[2,d]

[1]Department of Mechanical Engineering, Eskisehir Technical University, Eskisehir, Turkey
[2]Department of Mechanical Engineering, Ege University, Izmir, Turkey

Article Info	Abstract
	The aim of this study is to investigate the effect of mechanical milling and hot pressing process parameters on the density and strength of Al-10%B₄Cp composites. For this research, powder mixtures consisting of Al matrix and B₄C reinforcement particles were prepared by mechanical milling. Powder mixtures were milled for different times (5, 10, 15 and 20 hours) in a high energy planetary ball mill. In the milling vials, 10wt% B₄C particle reinforcements were added to aluminum matrix powders. Average particle size of B₄C and Al powders were 77μm and 63μm respectively. Powder mixtures were compacted as cylindrical samples by uniaxial hot pressing at 30 MPa. Specimens were hot pressed in nitrogen atmosphere at temperatures of 500-550-600 °C for 15-30-45 minutes. Effects of milling and hot pressing variables on microstructure and mechanical properties were investigated by means of density and hardness measurements and compression tests. Microstructures of powders and compacts were investigated by microscopy techniques. Density measurements showed that compressibility of powders decreased with increasing milling times. Density, hardness and compressive yield strength values were increased with increasing hot pressing temperature and durations.

1. Introduction

In recent years, the importance of aluminum based composites have increased in terms of manufacturing structural components over ferrous materials in transportation industries on account of unique properties including, low density, excellent mechanical properties and high wear resistance[1]. Aluminum MMC materials serves excellent properties compared to monolithic materials hence, they have been applied in different industries for high performance, economical benefit and environmental concerns. Lower carbon emission, less noise and lower fuel consumption are the utmost advantages of aluminum MMC in traffic engineering that environmental regulations and fuel economy concerns increases use of aluminum MMC in transportation industries[2]. Aluminum has several advantages including low density (2,71 g/cm3), excellent corrosion resistance, high toughness, high conductivity and low manufacturing cost that make aluminum one of the most appropriate matrix material[3, 4]. Therefore, there are many published studies on aluminum matrix composites with various reinforcement materials including alumina Al₂O₃)[5, 6], silicon carbide(SiC)[7], magnesium oxide(MgO)[8, 9], carbon nano tube(CNT)[10] and boron carbide (B₄C)[11, 12]. Relatively high hardness (9.5+ in Mohs

scale), elevated wear and impact resistance, high melting temperature and low density (2.52 g/cm3) are the outstanding features of boron carbide (B₄C) which make B₄C a potential reinforcement for MMC applications[13, 14]. Showordi et al., compared three aluminum metal matrix composites containing reinforcing particles of B₄C, SiC and Al₂O₃ and showed that B₄C exhibited better interfacial bonding than the others[15]. Pul, have also made a comparative study on aluminum matrix composite with SiC, B₄C and mixture of SiC and B₄C. It is reported that 20% wt. B₄C samples displayed highest wear resistance[16]. B₄C reinforced composites are being used in many applications including computer hard disk substrate, armor plate materials and structural neutron absorber an account of its superior properties[17].

It has been revealed by researchers that mechanical performance of Al matrix with B₄C reinforced composites were affected by many parameters. Raj and Thakur investigated the effect of particle size and volume fracture of B₄C particle on microstructural and tensile properties of aluminum matrix composite. They have reported that both volume fracture and particle size have influences on activation of different strengthening mechanisms[18]. Karakoç et al., showed that increasing volume fraction of B₄C particle reinforcement in the range of 0-20% improved the hardness, transverse rupture strength and tensile strength, on the other hand impact toughness was decreased[19]. Behm et al., have observed improved plasticity with both nano (40 nm) and submicron (500 nm) particle sized B₄C reinforcement over micron sized counterparts at the cost of reduced yield strength[20]. However, accumulation tendency of nano particle reinforcement due to robust Van der Waals forces between the particles must be considered[21]. Production method is also another parameter which yields different results in terms of mechanical and microstructural properties. Al/B₄C composites have been produced through a number of production technique such as stir casting[22], centrifugal casting[23] powder metallurgy[24], microwave sintering [25], spark plasma sintering[26], and shock compaction[27].

Liquid state methods and solid state methods are two main group of production route of metal matrix composites. Reaction between liquid aluminum and B4C generate undesirable reaction product including Al₃BC, AlB₂₄C₄ (AlB₁₀), Al₈B₄C₇, Al₃B₄₈C₂ (b-AlB₁₂), AlB₂, AlB₁₂C₂, AlB₄₈C₂, Al₄ C₃ and a-Alb₁₂.7[28]. Powder metallurgy (PM) is a solid state processing technique which have several advantages over liquid state methods such as uniform distribution of reinforcement, precision forming and prevention from undesirable chemical reactions[29, 30]. Oxide layer on the surface of aluminum powders is a concern which must be taken into account in PM of aluminum matrix composites due to the fact that it behaves as a diffusion barrier during sintering and inhibit inter-particle diffusion[31]. One of the main methods to eliminate the unfavorable effect of the oxide layer is to apply high compaction pressure which breaks layers and promote metal-metal contact. The other methods are employing oxide reduction additives including Mg, Zn and Si and liquid phase sintering[32]. Mechanical milling (MM) is a PM technique which can overcome this problem by fracturing detrimental oxide layer on the surface of aluminum powders for sintering [33]. Uniform distribution of reinforcement particles into the metal matrix, which is critical issue in PM to reach high performance, can be accomplished by MM[34]. Meignanamoorthy and Ravichandran synthesized AA8079 aluminum matrix composites contain various weight percentages (0, 5, 10 and 15) of B₄C through mechanical milling and powder metallurgy route. They have demonstrated that reinforcement phases were homogenously distributed in the matrix powder without agglomeration subsequent to milling operation[35]. Carreño-Gallardo et al., fabricated 2024 aluminum alloy matrixed B₄C reinforced composite via mechanical milling followed by cold compaction, sintering and T6 heat treatment. They have showed homogenously dispersion of B₄C particles by SEM images and attributed high microhardness and

compression yield strength values to distribution of the reinforcements[36]. Furthermore, MM refines grain size of matrix material occurs by severe plastic deformation due to collusion of milling balls during the process that increases mechanical properties of composite materials[37]. Khakbiz and Akhlaghi, obtained 57 nm crystal size by carrying out 16 hours mechanical milling to Al 6061/B_4C composite powders[38]. Alizadeh et al., also reported nanocrystalline aluminum matrix reinforced with B_4C by mechanical milling and they have reached extremely high strength (1.1 GPa)[39].

Porosity is also a critical issue in PM technology which must be taken into account and reduced as low as possible in order to obtain good mechanical properties[40]. Porosity is a critical issue for mechanically milled powders especially by virtue of decreasing compressibility of powders during MM process. It is well known that powders undergo severe plastic deformation during MM which increases hardness of powder particles[41]. Karasoglu et al., reported low bulk densities for longer milling durations and they have attributed poor density results to decreased compressibility of milled powder due to excessive work hardening [42].

Hot pressing is a powder consolidation technique which makes possible achieving nearly full density in a wide range of materials by applying powder pressing and sintering at the same time during consolidation. This method is convenient for consolidation of material with poor sintering characteristic[43]. Mohammad Sharifi et al., consolidated nano particle B_4C incorporated nanocrystalline aluminum powders by hot press technique under 300 MPa at 450 °C for 30 min., subsequent to mechanical milling. The relative density value of the hot pressed samples was measured to be about 98%[44]. Zhang et al., have also achieved nearly full dense Al/B_4C composite samples (>98.5%) via vacuum hot pressing[45].

In this study, boron carbide reinforced aluminum matrix composite fabricated by MM and hot pressing processes and influences of milling time and hot press parameters including, temperature, time and pressure were investigated.

2. Experimental Procedure

Pure aluminum powder with an average particle size of 63 μm was selected as matrix material and 10 wt_0% B_4C with an average particle size of 77 μm opted as reinforcement. Mixture of matrix and reinforcement powders was blended in a tubular mixer for 2h. Prior to blending, 2 wt.% zinc stearate was added to the powder mixture as a process control agent (PCA) in order to reduce cold welding propensity of ductile aluminum powders during MM process. After blending, MM was performed in a planetary ball milling machine for durations of 5, 10, 15 and 20 hours under argon atmosphere. Ball to powder weight ratio and milling speed were adjusted to 10:1 and 200 rpm, respectively.

Subsequent to milling, powders were consolidated through hot press sintering route. In order to determine optimum sintering parameters, sintering temperature and time were set at 500-550-600 °C and 15-30-45 min., respectively. All sintering processes were carried out in a graphite mold at 30 MPa uniaxial sintering pressure. Density of the sintered samples was measured geometrically. Morphology of powders and microstructures of bulk samples were investigated with an optical microscope (OM) and a scanning electron microscope (SEM). Hardness of sintered samples was measured under a test load of 500 gf by using a Vickers indenter. Compression tests were performed at a strain rate of 0.05 mm/min.

3. Results

3.1. Microscopy

Microstructural examination of milled powders obtained by a microscopy analysis is given in Figure 1. A predominantly flake-like morphology is observed in all milled powders (5-20h). Complete transformation from flake-like to equiaxial particle morphology could not be obtained even after 20 hours of milling time. The thickness of flakes decreased with increasing milling time (See also Fig.3). Rather than fracture, deformation and cold welding seem to be the dominant mechanisms. Very ductile nature of pure aluminum matrix, insufficient PCA, or relatively low milling speed (200 rpm) might be the reasons for the morphology of milled powders.

It has also been observed that various reinforcing particles are embedded in the soft matrix particles (Fig.2), which is one of the major aims of the MM process of ductile-brittle systems. However, steady state with equiaxial particles containing homogenous distribution of refined embedded reinforcement particles could not be obtained.
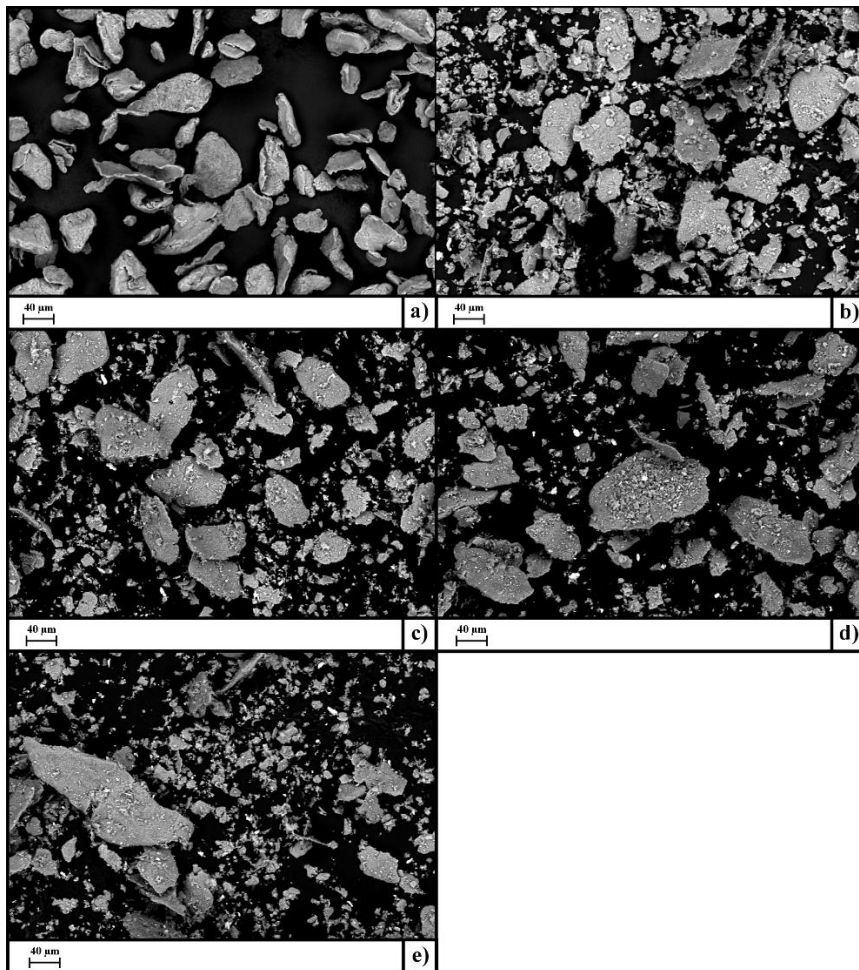

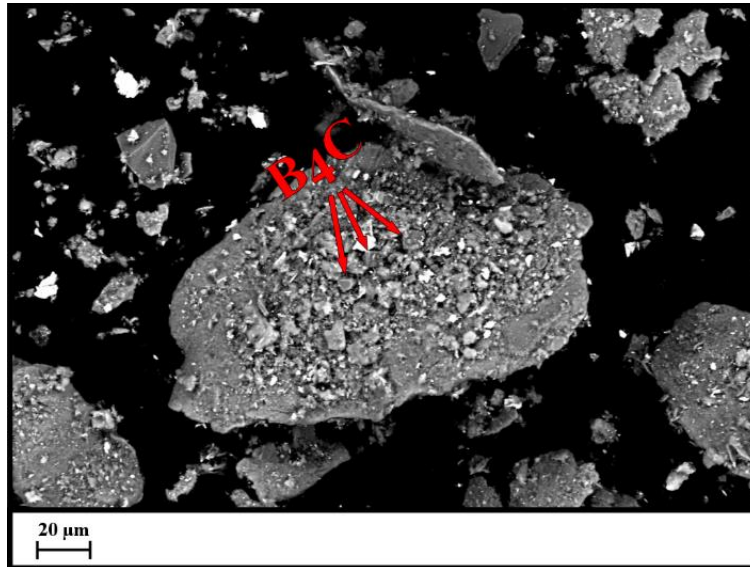Fig. 1 Morphology of samples a) un-milled, b) 5h milled, c)10h milled, d)15h milled, e) 20h milled

Fig. 2 B₄C reinforcement particles embedded in Al matrix powder

Optical micrographs of some hot pressed samples are given in Figure 3. A predominance of deformed flake-like particles is seen in milled samples. It is also seen that; the average particle size of the reinforcing particles decreases with increasing milling time. At the same time the refined particles are more homogeneously distributed in the matrix.
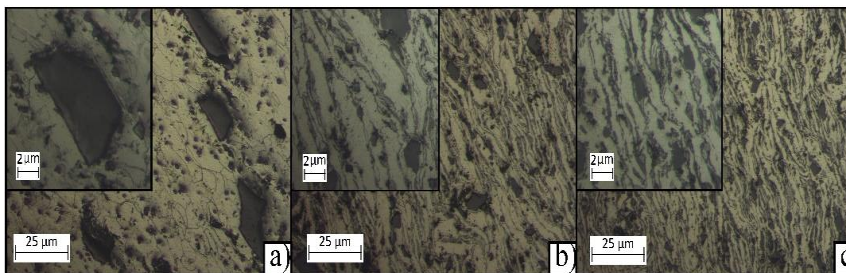

Fig. 3 a) reference sample b) 5h milled, sintered at 500 °C and 45 min c) 20h milled, sintered at 600 °C and 45 min.

3.2 Porosity

Figure 4 shows porosity levels of hot pressed samples. It indicates that mechanically milled samples have higher porosity levels than un-milled reference samples. This is because the hardness of milled powders is higher than as-received powders due to severe plastic deformation. Predominantly flake-like structure of the milled powders is another reason for low compressibility. Dispersion strengthening effect of reinforcing B₄C particles, which were refined and embedded into Al matrix, also makes the compressibility of the milled powders difficult.

Thus, milled powders have less compressibility which can be attributed to high porosity levels of sintered samples. Furthermore, porosity results depicted that increasing milling time decreased densities. Therefore, it was argued that reduced compressibility due to enhanced deformation hardening in the particles with increased milling times, may have adversely affected the consolidation rate, thus leading to relatively low densities after sintering.
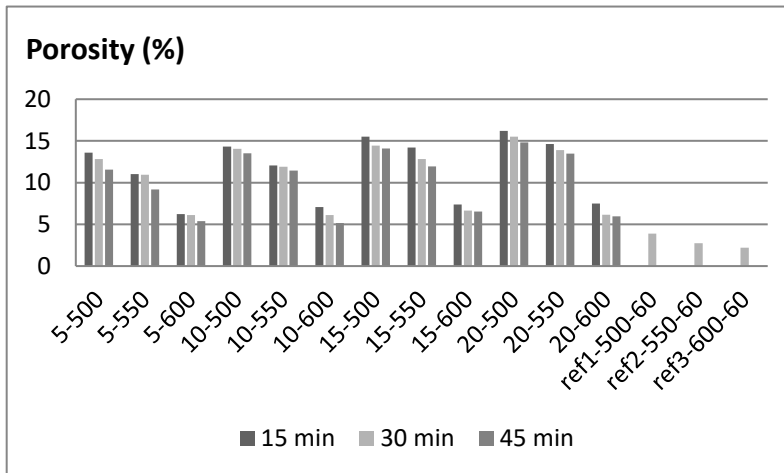

Fig. 4 Porosity of hot pressed samples

It can be concluded from Figure 4 that increasing hot pressing temperature led to formation of denser structure as a result of higher diffusion rates. Thus, the sintering temperature plays a major role as an important parameter in sintering process. Equation (1) explains this phenomenon[46] ;

$$D = D_0 exp\left(\frac{-Q}{RT}\right) \tag{1}$$

where D is the diffusion coefficient, D_0 is constant, Q is the activation energy, R is Boltzman's constant and T is the temperature. As expected, the relative density also increased with the sintering time prolonged which is expressed in equation 2[46];

$$r = 2.4\sqrt{Dt} \tag{2}$$

where r is radial distance, D is the diffusion coefficient and t is the sintering time. It appears that the lower sintering time did not allow for the formation of adequate inter-particle bonds required to consolidate the parts.

3.3 Compression and Hardness Tests

Compressive yield strength (CYS) and hardness values of hot pressed samples are demonstrated in Figure 5 and Figure 6 respectively. As seen in the figures, hardness and compressive strength values are very compatible with each other. It can obviously be seen that mechanically milled samples have higher CYS and hardness values compared to samples produced with as-received powders.
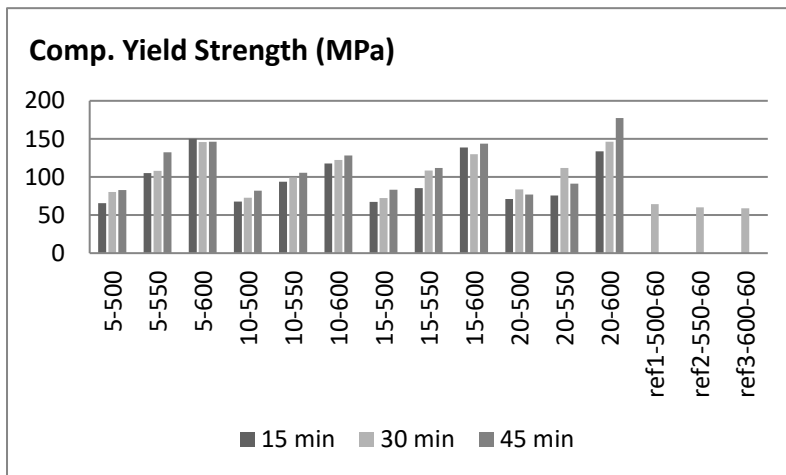
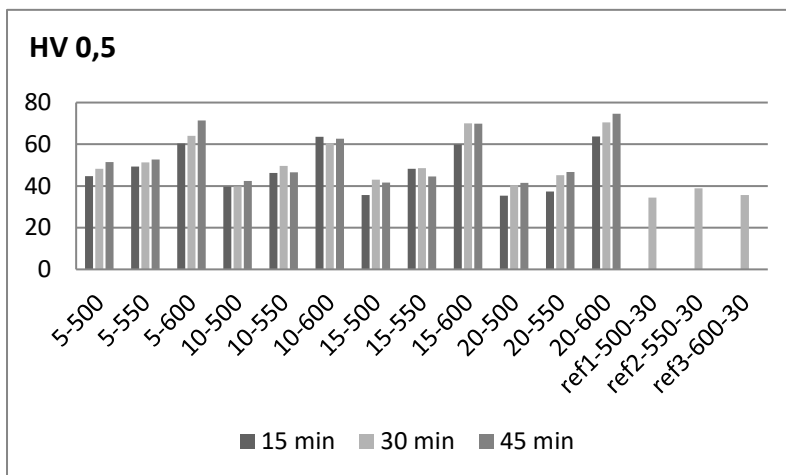Fig. 5 Compressive yield strength of hot pressed samples

Fig. 6 Hardness of hot pressed samples

Higher CYS and hardness values can be attributed to finer grain size of the aluminum matrix of milled samples. It is well known that MM operation begets to grain refinement of metals by severe plastic deformation [14]. It can be seen from the microstructure of the samples that (Figure 3) while MM'ed samples have morphologically flattened matrix particles indicating heavily deformation, matrix particles of reference samples are equiaxed and free of deformation. Although milled samples have lower densities, grain refinement of matrix material and dispersion of finer reinforcement effects compensate the loss of density in terms of CYS and hardness. The relation between matrix grain size and the increase in strength can be explained by the Hall-Petch equation which is given by[47];

$$\sigma_y = \sigma_0 + kd^{-\frac{1}{2}} \tag{3}$$

where σ_0 is the friction stress, k is a constant of yielding and d is the average grain size of the matrix. In Figure 3., finer reinforcement particles in MM'ed samples can be seen clearly. Particle size of reinforcement have pronounced effect on mechanical properties of composites. It is reported that reducing the particle size of reinforcement, greatly improves the strength of material[48].

Another significant factor affecting physical and mechanical properties of composite is distribution of reinforcement particles in the matrix phase. Mechanical milling is a process producing uniform dispersion of reinforcement particles in the matrix by repeated welding–fracturing–welding of a mixture of powder particles[49]. More uniform distribution of reinforcement particles of milled samples can be seen in Figure 3-c obviously, which may contribute higher CYS and hardness despite of low densities. Strength values were increased with increasing hot press temperature and time which is consistent with density results. High densities on account of higher diffusion rates explained above, may have led to stronger interfacial bonding and resulted higher CYS levels. It is well known that if the interfacial bonding between the matrix and second phase is strong, the load transfer mechanism becomes active. Enhancement in yield strength by load transfer based on the modified shear lag model is expressed as[50];

$$\Delta\sigma_y = \frac{1}{2}.f.\sigma_m \qquad (4)$$

where f is the volume fraction of the reinforcement and σ_m is the yield strength of the matrix.

In Figure 7, it can be seen that bright white colored second phase particles appeared in milled sample. These particles may be iron particles which could be formed from wearing of steel vial and balls during mechanical milling operation. These particles may have also behaved as reinforcements and led to an improvement in strength and hardness of the material.
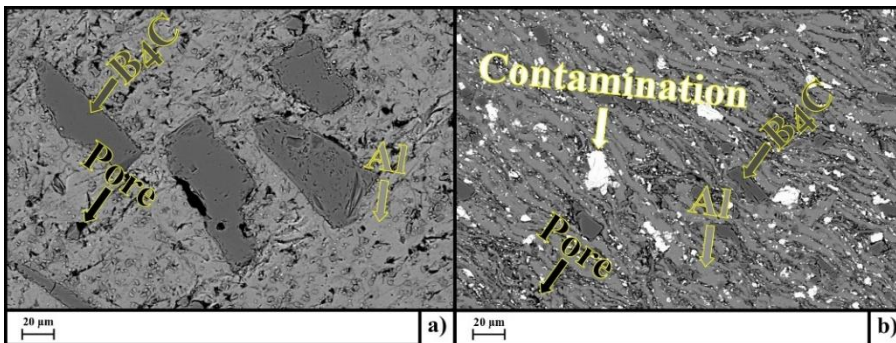

Fig. 7 SEM images of a) reference sample b) 20h milled, sintered at 600 °C and 45 min.

Although mechanical milling has a prominent effect on CYS and hardness, influence of milling time is not certain. Results did not follow expectation of increasing strength with increasing milling time. Instead, a fluctuation appeared in compression test measurement. This situation may be related to densities.

4. Conclusion

The influence of the milling time, sintering temperature and sintering time on the mechanical properties of the Al matrix B_4C reinforced composites produced through

mechanical milling and hot pressing route was investigated. The major findings of this study can be summarized as follows.

- A predominance of deformed flake-like particles was observed even in 20 h milled samples. Rather than fracture, deformation and cold welding were dominant mechanisms in mechanical milling processes.
- Strengthening of powders by work hardening, grain boundary hardening and dispersion hardening during mechanical milling decreased their compressibility. Porosity level of samples increased with increasing mechanical milling time.
- Density is one of the most important factors determining strength of the samples. High hardness and compressive yield strength require high density.
- Increasing sintering time and temperature increased the density of the samples which increased the compressive yield strength and hardness values.
- Despite their lower density, higher strength values were observed in the milled samples than in the un-milled samples. Much higher strength values can be achieved if higher densities can be obtained in milled powders. Since the pressure that can be applied in the graphite hot pressing molds is limited, a cold prepressing operation can be performed in the metal molds to increase the density.

References

[1] Padmavathi C, Upadhyaya A. Densification, microstructure and properties of supersolidus liquid phase sintered 6711 Al-Sic metal matrix composites. Science of sintering. 2010;42(3):363-82. https://doi.org/10.2298/SOS1003363P

[2] Surappa M. Aluminium matrix composites: Challenges and opportunities. Sadhana. 2003;28(1-2):319-34. https://doi.org/10.1007/BF02717141

[3] Torralba Jd, Da Costa C, Velasco F. P/M aluminum matrix composites: an overview. Journal of Materials Processing Technology. 2003;133(1-2):203-6. https://doi.org/10.1016/S0924-0136(02)00234-0

[4] Baghchesara MA, Abdizadehb H. Production and microstructural investigation of A356 aluminum alloy based Magnesium oxide particles reinforced metal-matrix nanocomposites. J Ceram Process Res. 2014;15:418-23.

[5] Kok M. Production and mechanical properties of Al2O3 particle-reinforced 2024 aluminium alloy composites. Journal of Materials Processing Technology. 2005;161(3):381-7. https://doi.org/10.1016/j.jmatprotec.2004.07.068

[6] Rahimian M, Ehsani N, Parvin N, reza Baharvandi H. The effect of particle size, sintering temperature and sintering time on the properties of Al-Al2O3 composites, made by powder metallurgy. Journal of Materials Processing Technology. 2009;209(14):5387-93. https://doi.org/10.1016/j.jmatprotec.2009.04.007

[7] Karaşoğlu M, Karaoğlu S. TozMetalurjisi İle Üretilen Alüminyum Matrisli Kompozitlerde Proses Ve Malzeme Değişkenlerinin Mikroyapı Ve Mekanik Özelliklere Etkisi. Mühendis ve Makina. 2014;55(649):17-23.

[8] Abdizadeh H, Ebrahimifard R, Baghchesara MA. Investigation of microstructure and mechanical properties of nano MgO reinforced Al composites manufactured by stir casting and powder metallurgy methods: A comparative study. Composites Part B: Engineering. 2014;56:217-21. https://doi.org/10.1016/j.compositesb.2013.08.023

[9] Yar AA, Montazerian M, Abdizadeh H, Baharvandi H. Microstructure and mechanical properties of aluminum alloy matrix composite reinforced with nano-particle MgO. Journal of Alloys and Compounds. 2009;484(1-2):400-4. https://doi.org/10.1016/j.jallcom.2009.04.117

[10] George R, Kashyap K, Rahul R, Yamdagni S. Strengthening in carbon nanotube/aluminium (CNT/Al) composites. Scripta Materialia. 2005;53(10):1159-63. https://doi.org/10.1016/j.scriptamat.2005.07.022

[11] Kerti I, Toptan F. Microstructural variations in cast B4C-reinforced aluminium matrix composites (AMCs). Materials letters. 2008;62(8-9):1215-8. https://doi.org/10.1016/j.matlet.2007.08.015

[12] Baradeswaran A, Perumal AE. Influence of B4C on the tribological and mechanical properties of Al 7075-B4C composites. Composites Part B: Engineering. 2013;54:146-52. https://doi.org/10.1016/j.compositesb.2013.05.012

[13] Kennedy A, Brampton B. The reactive wetting and incorporation of B 4 C particles into molten aluminium. Scripta Materialia. 2001;7(44):1077-82. https://doi.org/10.1016/S1359-6462(01)00658-3

[14] Lee B-S, Kang S. Low-temperature processing of B4C-Al composites via infiltration technique. Materials Chemistry and Physics. 2001;67(1-3):249-55. https://doi.org/10.1016/S0254-0584(00)00446-6

[15] Shorowordi KM, Laoui T, Haseeb A, Celis J-P, Froyen L. Microstructure and interface characteristics of B4C, SiC and Al2O3 reinforced Al matrix composites: a comparative study. Journal of Materials Processing Technology. 2003;142(3):738-43. https://doi.org/10.1016/S0924-0136(03)00815-X

[16] Pul M. Effect of sintering on mechanical property of SiC/B4C reinforced aluminum. Materials Research Express. 2018;6(1):016541. https://doi.org/10.1088/2053-1591/aacee1

[17] Asghar Z, Latif MA, Rafi-ud-Din, Nazar Z, Ali F, Basit A, et al. Effect of distribution of B4C on the mechanical behaviour of Al-6061/B4C composite. Powder Metallurgy. 2018;61(4):293-300. https://doi.org/10.1080/00325899.2018.1501890

[18] Raj R, Thakur D. Effect of particle size and volume fraction on the strengthening mechanisms of boron carbide reinforced aluminum metal matrix composites. Proceedings of the Institution of Mechanical Engineers, Part C: Journal of Mechanical Engineering Science. 2019;233(4):1345-56. https://doi.org/10.1177/0954406218771997

[19] Karakoç H, Karabulut Ş, Çıtak R. Study on mechanical and ballistic performances of boron carbide reinforced Al 6061 aluminum alloy produced by powder metallurgy. Composites Part B: Engineering. 2018;148:68-80. https://doi.org/10.1016/j.compositesb.2018.04.043

[20] Behm N, Yang H, Shen J, Ma K, Kecskes LJ, Lavernia EJ, et al. Quasi-static and high-rate mechanical behavior of aluminum-based MMC reinforced with boron carbide of various length scales. Materials Science and Engineering: A. 2016;650:305-16. https://doi.org/10.1016/j.msea.2015.10.064

[21] Ma K, Lavernia EJ, Schoenung JM. Particulate reinforced aluminum alloy matrix composites-a review on the effect of microconstituents. Rev Adv Mater Sci. 2017;48:91-104.

[22] Shirvanimoghaddam K, Khayyam H, Abdizadeh H, Akbari MK, Pakseresht A, Ghasali E, et al. Boron carbide reinforced aluminium matrix composite: Physical, mechanical characterization and mathematical modelling. Materials Science and Engineering: A. 2016;658:135-49. https://doi.org/10.1016/j.msea.2016.01.114

[23] Durnev M, Eidelman E. Distribution of supercritical nucleation centers during the crystallization process in the presence of a flow as illustrated by the example of boron carbide-reinforced aluminum. Наносистемы: физика, химия, математика. 2017;8(3). https://doi.org/10.17586/2220-8054-2017-8-3-360-364

[24] Gomez L, Busquets-Mataix D, Amigo V, Salvador M. Analysis of boron carbide aluminum matrix composites. Journal of composite materials. 2009;43(9):987-95. https://doi.org/10.1177/0021998308097731

[25] Ghasali E, Alizadeh M, Ebadzadeh T, hossein Pakseresht A, Rahbari A. Investigation on microstructural and mechanical properties of B4C-aluminum matrix composites prepared by microwave sintering. Journal of Materials Research and Technology. 2015;4(4):411-5. https://doi.org/10.1016/j.jmrt.2015.02.005

[26] Ghasali E, Alizadeh M, Ebadzadeh T. Mechanical and microstructure comparison between microwave and spark plasma sintering of Al-B4C composite. Journal of Alloys and Compounds. 2016;655:93-8. https://doi.org/10.1016/j.jallcom.2015.09.024

[27] Bond G, Inal O. Shock-compacted aluminum/boron carbide composites. Composites Engineering. 1995;5(1):9-16. https://doi.org/10.1016/0961-9526(95)93975-2

[28] Viala J, Bouix J, Gonzalez G, Esnouf C. Chemical reactivity of aluminium with boron carbide. Journal of Materials Science. 1997;32(17):4559-73. https://doi.org/10.1023/A:1018625402103

[29] Vani VV, Chak SK. The effect of process parameters in aluminum metal matrix composites with powder metallurgy. Manufacturing Review. 2018;5:7. https://doi.org/10.1051/mfreview/2018001

[30] Fan G, Xu R, Tan Z, Zhang D, Li Z. Development of flake powder metallurgy in fabricating metal matrix composites: a review. Acta Metallurgica Sinica (English Letters). 2014;27(5):806-15. https://doi.org/10.1007/s40195-014-0148-x

[31] MacAskill I, Hexemer Jr R, Donaldson I, Bishop D. Effects of magnesium, tin and nitrogen on the sintering response of aluminum powder. Journal of Materials Processing Technology. 2010;210(15):2252-60. https://doi.org/10.1016/j.jmatprotec.2010.08.018

[32] Oh MC, Byungmin A. Effect of Mg composition on sintering behaviors and mechanical properties of Al-Cu-Mg alloy. Transactions of Nonferrous Metals Society of China. 2014;24:s53-s8. https://doi.org/10.1016/S1003-6326(14)63288-X

[33] Arik H. Production and characterization of in situ Al4C3 reinforced aluminum-based composite produced by mechanical alloying technique. Materials & design. 2004;25(1):31-40. https://doi.org/10.1016/S0261-3069(03)00163-8

[34] Kamrani S, Simchi A, Riedel R, Seyed Reihani S. Effect of reinforcement volume fraction on mechanical alloying of Al-SiC nanocomposite powders. Powder Metallurgy. 2007;50(3):276-82. https://doi.org/10.1179/174329007X189621

[35] Meignanamoorthy M, Ravichandran M. Synthesis, properties and microstructure of sintered and hot extruded boron carbide reinforced AA8079 (Al-Cu-Fe-Si-Zn) matrix composites. Materials Research Express. 2018;5(11):116508. https://doi.org/10.1088/2053-1591/aadc57

[36] Carreño-Gallardo C, Estrada-Guel I, López-Meléndez C, Ledezma-Sillas E, Castañeda-Balderas R, Pérez-Bustamante R, et al. B4C particles reinforced Al2024 composites via mechanical milling. Metals. 2018;8(8):647. https://doi.org/10.3390/met8080647

[37] Khan AS, Farrokh B, Takacs L. Effect of grain refinement on mechanical properties of ball-milled bulk aluminum. Materials Science and Engineering: A. 2008;489(1-2):77-84. https://doi.org/10.1016/j.msea.2008.01.045

[38] Khakbiz M, Akhlaghi F. Synthesis and structural characterization of Al-B4C nano-composite powders by mechanical alloying. Journal of Alloys and Compounds. 2009;479(1-2):334-41. https://doi.org/10.1016/j.jallcom.2008.12.076

[39] Alizadeh A, Maleki M, Abdollahi A. Preparation of super-high strength nanostructured B4C reinforced Al-2Cu aluminum alloy matrix composites by mechanical milling and hot press method: microstructural, mechanical and tribological characterization. Advanced Powder Technology. 2017;28(12):3274-87. https://doi.org/10.1016/j.apt.2017.10.007

[40] Torralba JM, Campos M. Toward high performance in powder metallurgy. Rev Metal. 2014;50(2):e017. https://doi.org/10.3989/revmetalm.017

[41] Enayati M, Mohamed F. Application of mechanical alloying/milling for synthesis of nanocrystalline and amorphous materials. International Materials Reviews. 2014;59(7):394-416. https://doi.org/10.1179/1743280414Y.0000000036

[42] Karasoglu M, Karaoglu S, Arslan G. Mechanical properties of Mg-based materials fabricated by mechanical milling and spark plasma sintering. Proceedings of the Institution of Mechanical Engineers, Part L: Journal of Materials: Design and Applications. 2018:1464420718805119. https://doi.org/10.1177/1464420718805119

[43] Upadhyaya G. Powder metallurgy technology: Cambridge Int Science Publishing; 1997.

[44] Sharifi EM, Karimzadeh F, Enayati M. Fabrication and evaluation of mechanical and tribological properties of boron carbide reinforced aluminum matrix nanocomposites. Materials & Design. 2011;32(6):3263-71. https://doi.org/10.1016/j.matdes.2011.02.033

[45] Zhang L, Wang Z, Li Q, Wu J, Shi G, Qi F, et al. Microtopography and mechanical properties of vacuum hot pressing Al/B4C composites. Ceramics International. 2018;44(3):3048-55. https://doi.org/10.1016/j.ceramint.2017.11.065

[46] Porter DA, Easterling KE, Sherif M. Phase Transformations in Metals and Alloys, (Revised Reprint): CRC press; 2009.

[47] Hall E. The deformation and ageing of mild steel: III discussion of results. Proceedings of the Physical Society Section B. 1951;64(9):747. https://doi.org/10.1088/0370-1301/64/9/303

[48] Slipenyuk A, Kuprin V, Milman Y, Goncharuk V, Eckert J. Properties of P/M processed particle reinforced metal matrix composites specified by reinforcement concentration and matrix-to-reinforcement particle size ratio. Acta Materialia. 2006;54(1):157-66. https://doi.org/10.1016/j.actamat.2005.08.036

[49] Abdoli H, Salahi E, Farnoush H, Pourazrang K. Evolutions during synthesis of Al-AlN-nanostructured composite powder by mechanical alloying. Journal of Alloys and Compounds. 2008;461(1-2):166-72. https://doi.org/10.1016/j.jallcom.2007.07.054

[50] Han B, Dunand DC. Microstructure and mechanical properties of magnesium containing high volume fractions of yttria dispersoids. Materials Science and Engineering: A. 2000;277(1-2):297-304. https://doi.org/10.1016/S0921-5093(99)00074-X

Research Article

Comparison of wood and knot on wear behaviour of pine timber

Samiul Kaiser[1,a], Mohammad Salim Kaiser*[,2,b]

[1]*Department of Civil Engineering, Bangladesh University of Engineering and Technology, Dhaka-1000, Bangladesh*
[2]*Directorate of Advisory, Extension and Research Services, Bangladesh University of Engineering and Technology, Dhaka-1000, Bangladesh*

Article Info	Abstract
	The wear behaviour of the wood and knot of pine timber is evaluated at ambient conditions. The experiment is carried out under dry sliding conditions using a pin-on-disc apparatus. Wear testing parameters are chosen as 20N load, sliding velocity of 0.64 ms^{-1} and sliding distance ranging from 200m-4500m. The worn surfaces are characterized by optical microscope and scanning electron microscopy. Hardness of wood and knot samples is measured in Durometer hardness tester, tensile testing by an Instron testing machine and density of the samples is calculate from the data of volume and weight. The results of the wear test reveal that the knot shows the better wear properties due to higher strength and density. SEM study of the knot and wood disclose that the knot contents compact cell wall than that of wood.

1. Introduction

A knot is a particular type of imperfection in a piece of wood. It affects the physical and mechanical properties as increase the compression strength, hardness, and shear characteristics of the wood and decrease the tensile and bending strength. It causes uneven wear on the surfaces, give trouble because of the checking with moisture changes, make difficulty in painting and increase for cutting forces [1-4]. In a longitudinally sawn plank, a knot will appear as a roughly circular "solid" piece of wood around which the grain of the rest of the wood "flows". Within a knot, the direction of the wood grain is up to 90 degrees different from the grain direction of the regular wood. Pine is an inexpensive, lightweight wood that can be yellowish or whitish with brown knots [5, 6].

The strength of wood depends on its density. Whet the density increases the strength also increase. When evaluating the density of wood, the level of moisture in which its mass and volume were measured must always be known. Usually the density of wood is specified as dry air density [7, 8]. The strength of the wood is basically affected by the direction in which it is loaded in relation to the grain. Knots are portions of branches that become included into the tree trunk during growth and influence the strength properties of a piece wood. Knots decrease the strength of wood mainly because of interrupting the direction of grain, localized steep slope of grain concentrates around knots. As the proportion of knot

on the cross section increases, density increases. Shrinkage values are not deferent especially in the specimens containing small knots [9-11].

Development of composite material specifically reinforced plastic composites has made a significant contribution since last few decades. However natural fiber reinforced composite has carved an important place made out of waste of organic materials. In this context composites prepared out of wood waste such as saw dust has been considered to replace artificial fiber reinforced composites owing to its ecofriendly nature and reasonably sound mechanical properties [12, 13]. So the frictional properties of wood may be an important factor in these regards.

The mechanical properties of clear wood are well known while for defects such as knots they are relatively unknown. The aim of this study is to understand the wear as well as the physical and mechanical properties of individually wood and knot of pine timber.

2. Experimental Details

The frictional and wear behaviors of the wood and knot were investigated in a pin-on disc type wear apparatus by following ASTM Standard G99-05. The samples of 12 mm length and 5 mm diameter were obtained from the wood and knot of pine timber for this study. Mild steel discs were used as the counter-body material. One of the surfaces of the disc was grinded by surface grinding machine and cleaned with cotton. The hardness and surface roughness of the mild steel discs was RC 50 and 0.31 μm respectively. During the wear tests, the end surfaces of the pin samples were pressed against horizontal rotating mild steel disc. Load of 20N was used throughout the test, which yielded nominal contact pressures of 1.0MPa. The tests were conducted at the sliding speed of 0.64 ms^{-1} with varying sliding distances ranging from 200m-4500m. All the tests were carried out in ambient air (humidity 70%) under dry sliding condition. The experimental photograph of setup is shown in Fig. 1. At least three tests were done for each type of material. The sliding distances were calculated by knowing the track diameter and speed of rotation of the disc. Volume loss was calculated from average values of weight-loss measurements. Wear rate and co-efficient of friction were determined with the help of following equations [14, 15]:

$$WR = \frac{\Delta V}{SD \times L} \tag{1}$$

$$\mu = \frac{FF}{L} \tag{2}$$

Where (WR) is the wear rate of the sample, (ΔV) is the volume loss by sample after each wear test, (SD) is the sliding distance, L is the load applied on sample, μ is the friction co-efficient of the sample and FF is the friction factor of the sample.

Hardness of wood and knot samples was measured in Durometer Hardness tester. An average of ten concordant readings was taken as the representative hardness of a sample. Tensile testing was carried out in an Instron testing machine, using cross head speed to maintain the strain rate of 10^{-3}/s. The samples used were according to ASTM specification. Tensile test was determined using five test pieces for each test. Density of the wooden sample at various states was calculated from the data of volume and weight. Microstructural observation of the worn specimens was done by using USB digital microscope and some selected photomicrographs were taken. The SEM investigation was conducted by using a JEOL scanning electron microscope.
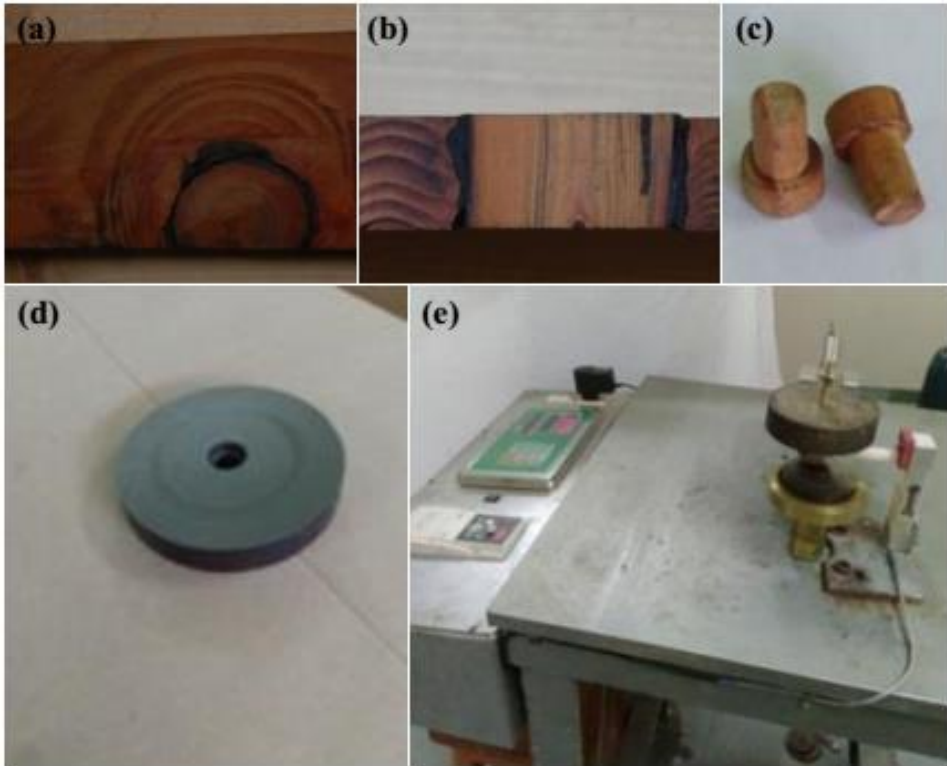
Fig. 1 Experimental pine wood a) top view, b) front view, c) wear sample of wood and knot, d) MS counter disk and e) wear testing machine

3. Results and Discussion

3.1. Physical and Mechanical Properties

Fig. 2 shows the density, hardness, ultimate tensile strength and elongation of wood and knot of pine timber. The knot shows the higher hardness as well as the tensile strength due to higher compactness of cells present in to the knot. The minimum variation of elongation may be due to the higher bound water into the cell at hand in the knot. Knot itself is different in density usually higher. Its grain orientation is more or less perpendicular to the surrounding wood. So shrinkage is greater across the knot than the surrounding wood [16]. Wood is a heterogeneous, hygroscopic, cellular and anisotropic material. It is composed of cells and the cell walls are composed of micro-fibrils of cellulose and hemicelluloses' impregnated with lignin. The density of wood is an important property to consider since the stiffness, strength and shrinkage properties are all dependent on the density. Lignin and hemicelluloses are material constituents of wood that absorb water and swell, which affects the volume and the weight of a wood sample [17].
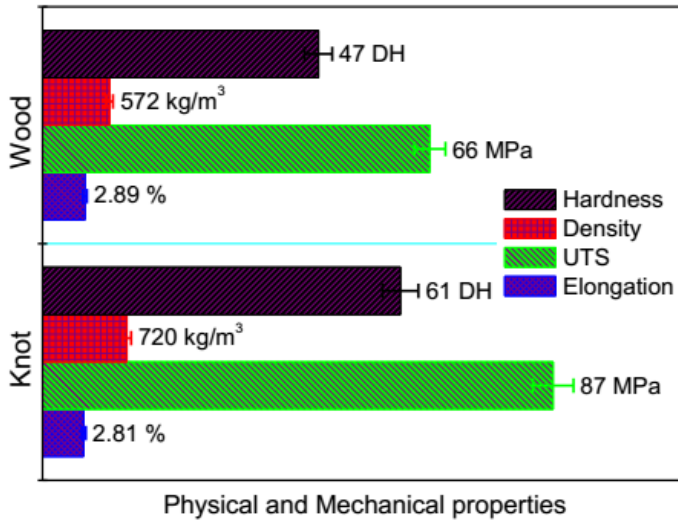
Fig. 2 Experimental result of physical and mechanical properties of the wood and knot of pine timber

3.2. Wear Behavior

Fig. 3 shows the volume loss of pine wood and knot as a function of sliding distance at normal load of 20N and sliding speed of 0.64 ms^{-1}. It is generally known that with increasing sliding distance, the volume loss increases due to more intimate contact time between the contact surfaces of the specimen with the rotating disc. However, less volume loss was observed in case of the knot compared to the wood at higher sliding distance. With increase in sliding distance causes a rise in interface temperature results in thermal softening of the material causing removal of the thin metal layer from the surface. The continuous fracture of thin layer leads to higher volume loss [18-20].

Fig. 4 presents the wear rate vs. sliding distance plot for wood and knot of pine timber. It can be observed that wear rate increased at a steep rate initially for wood and knot and after a certain point onwards attained a constant value for wood and the decreases trend for the knot. Initially maximum wear rate was observed because abrasive mild steel was fresh. With consecutive runs wear rate decreased gradually because the abrasive grits become smooth and less effective. The wear debris filled the space between the abrasives, which reduced the depth of penetration in the sample. As a tree grows and increases the circumference of its trunk, the growing trunk begins to overtake the branches that grow out from it. Knots form around these branches, building up trunk material as the tree continues to expand. Since the branches are still growing as they are overtaken by the trunk, the knot that forms is solid and contains living wood throughout. The wood of the knot is typically tougher than the surrounding wood and may form a bulge around the branch emerging from its centre. That is why the wear rate of the knot is minimum than that of wood.

The relationships between the coefficient of friction and the sliding distance for the wood and knot on the mild steel counter body is shown in Fig. 5. These differences in the coefficient of friction are considered to be due to both adhesion and deformation components of friction between wood and counter face material. The frictional force is higher for knot sample than that of wood sample. The reason could be due to the presence of fine grain structure in the knot sample and the coarse grain structure in the wood sample. The fine grains have greater surface area per unit volume than the large and

irregular grains. The higher bound water increases the moister content of the knot. It is also another reason for higher coefficient of friction [21]. The coefficient of friction decreased linearly with sliding distance. Interface temperature increases with increment in sliding distance that may promote the surface oxidation and reduce the direct contact hence there is slight decline in frictional coefficient [22]. In case of wood the rate of decreases of friction coefficient is relatively higher because of minimum adsorbed water into the cell wall. It softens the cellulose/lignin material of the cell water. Therefore, it reduces all strength and stiffness properties; that weakens the wood [23]
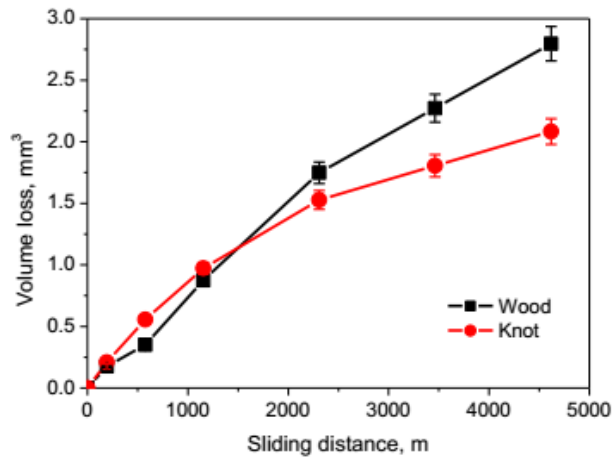
Fig. 3 Variation of volume loss with sliding distance at applied pressure of 1.0MPa and sliding velocity of 0.64 ms^{-1}
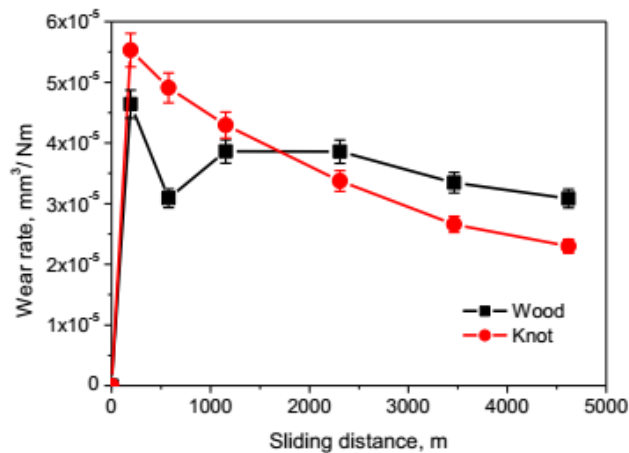
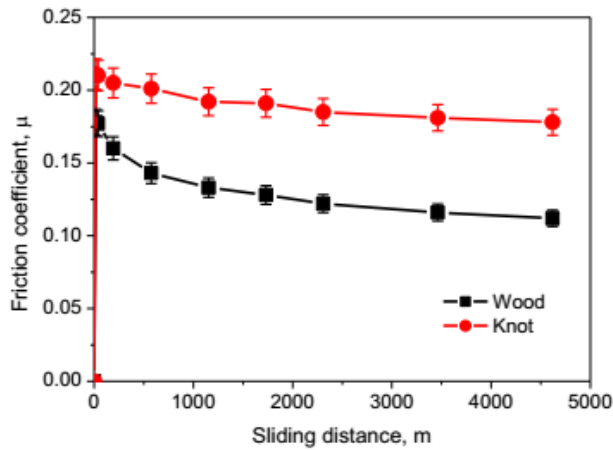Fig. 4 Variation of wear rate with sliding distance at applied pressure of 1.0MPa and sliding velocity of 0.64 ms^{-1}

Fig. 5 Variation of friction coefficient with sliding distance at applied pressure of 1.0MPa and sliding velocity of 0.64 ms^{-1}

Fig. 6 shows the comparison of the variation of friction coefficient with normal load for wood and knot. These results show that friction coefficient decreases with the increase in normal load. Increased surface roughness and a large quantity of wear debris are believed to be responsible for the decrease in friction with the increase in normal load. Similar behavior is obtained for wood [24-26] i.e. friction coefficient decreases with the increase in normal load.
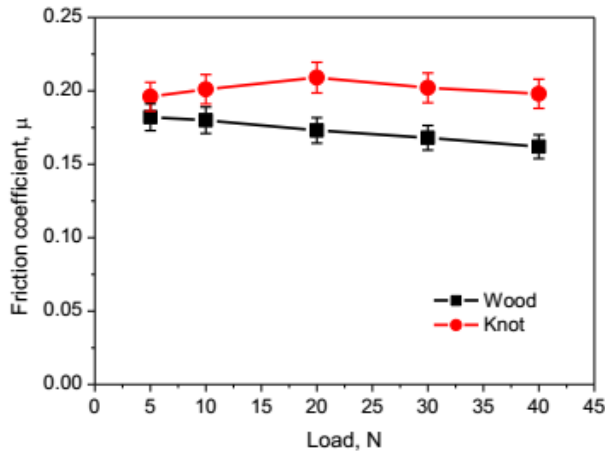

Fig. 6 Variation of friction coefficient with applied load at sliding velocity of 0.64 ms^{-1}

3.3. Optical Microscopic Observation

In Fig. 7 are presented the worn surfaces for the wood and knot at different sliding distances. Before wear the microstructure of the wood and knot show the smooth cell wall (Fig. 7a and 7b). In case of knot some spots are observed as it contents dead cells [27]. After wear for 200m the wood and knot microstructure show the lines in the direction of weariness (Fig. 7c and 7d). The damaged surface due to the adhesion wear, distortion took place in the surface of the specimen. It can also be observed that the surfaces of wood and knot as the sliding distance increase the wear marks becomes more visible and deep (Fig. 7e and 7f).
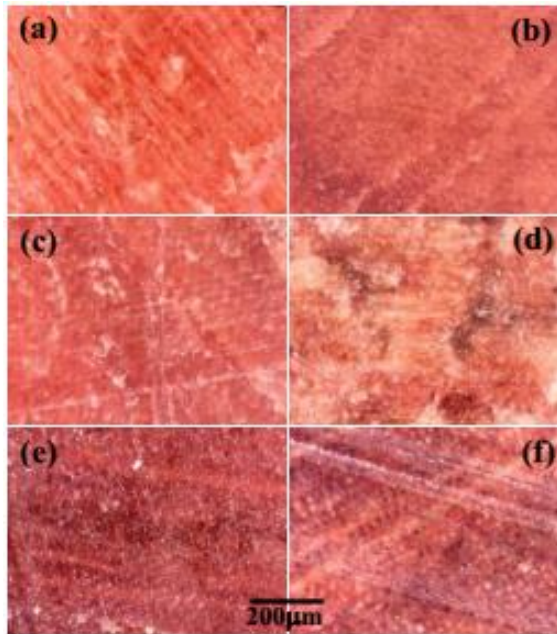
40

Fig. 7 Optical micrograph of worn surfaces of the wood and knot at different sliding distances at applied pressure of 1.0 MPa and sliding velocity 0.64 ms^{-1}

Fig. 8 shows the surfaces of MS counter-body which contents the dust of wood and knot generated during wear experiment at different sliding distances. Fig. 8a and 8b contains the dust of wood and knot after wear for 200m and Fig. 8c and 8d after wear for 4500m respectively. It shows that the higher sliding distance produces the higher amount of dust on the MS counter body. In this study, the dust is generated during the wear experiments from knot, contain higher amounts of large sized particles. This is due to fact that the knot contents compact cell wall. Whereas, the small sized particles produced from wood because of the losses cell wall.
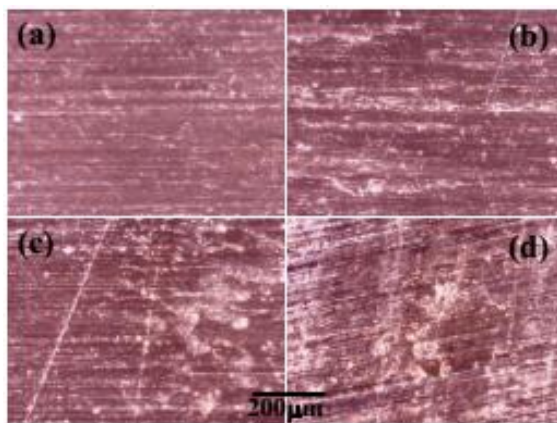

Fig. 8 Optical micrograph of MS disc surfaces for the wood and knot at different sliding distances at applied pressure of 1.0 MPa and sliding velocity 0.64 ms^{-1}

3.4. Scanning Electron Microscopy

The SEM micrographs of the wood and knot of pine timber are shown in Fig. 9a and 9b respectively. The wood fiber is basically built up of the polymers: cellulose, hemicelluloses, and lignin. Pectin, inorganic compounds, and extractives are also present in wood, although only as minor components. Wood consists of regular cell with larger cavity than that of knot. The higher number of compact cells is observed in the knot structure. The knot stays perpendicular from the grain direction of the regular wood. During growth the tree compresses the knot which results the compact cell [28, 29].
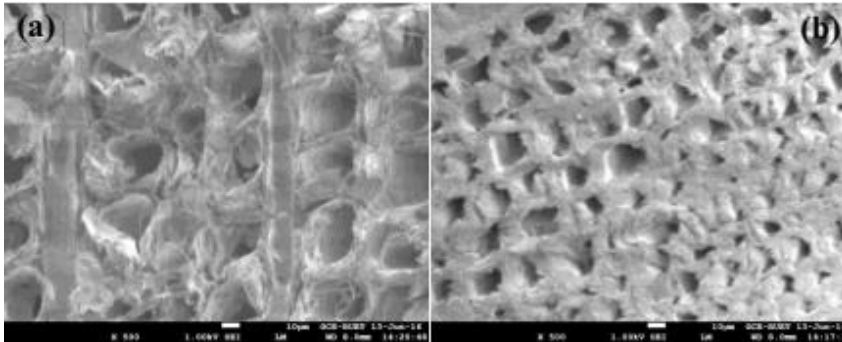

Fig. 9 SEM images of the a) wood and b) knot of pine timber

4. Conclusion

The knot itself is harder, denser, often more resinous and shrinks in a manner different from that of the surrounding tissue. Knot itself shows the higher mechanical properties than that of the wood. Wear rate increases to a maximum for wood and knot then attain a plateau for wood and decreases for knot with increasing sliding distance. The superior mechanical property of the knot leads to its better wear resistance. Regular cells with larger cavity are observed in wood structure and the knot contains the compact cell wall in the structure.

Acknowledgement

References

[1] As N, Geker Y, Dundar T. Effect of Knots on the physical and mechanical properties of scots pine. Wood Research, 2006; 51: 51-58.

[2] Gupta R, Basta C, Kent SM. Effect of knots on longitudinal shear strength of douglas-fir using shear blocks. Forest Products Journal, 2004; 54: 77-83.

[3] Kunesh RH, Johnson JW. Effect of single knots on tensile strength of 2-by 8- inch douglas-fir dimension lumber. Forest Products Journal, 1972; 22: 32-37.

[4] Guindos P, Polocoser T. Numerical calculations of the influence of the slope of grain on the effect of knots. European Journal of Wood and Wood Products, 2015; 73: 271-273. https://doi.org/10.1007/s00107-014-0876-7

[5] Green DW, Winandy JE, Kretschmann DE. Mechanical properties of wood, Madison: Department of Agriculture, Forest Service, Forest Products Laboratory; USA; 1999.

[6] Koman S, Feher S, Abraham J, Taschner R. Effect of knots on the bending strength and the modulus of elasticity of wood. Wood Research 2013; 58(4): 617-626.

[7] Thomas S, Montagu KD, Conroy JP. Temperature effects on wood anatomy, wood density, photosynthesis and biomass partitioning of Eucalyptus grandis seedlings. Tree Physiology, 2007; 27: 251-260. https://doi.org/10.1093/treephys/27.2.251

[8] Jamala GY, Olubunmi SO, Mada DA, Abraham P. Physical and mechanical properties of selected wood species in tropical rainforest ecosystem, Ondo State, Nigeria. IOSR Journal of Agriculture and Veterinary Science, 2013; 5(3): 29-33. https://doi.org/10.9790/2380-0532933

[9] Kollmann F, Cote WA. Principles of wood science and technology. Solid Wood, Springer, 1968. https://doi.org/10.1007/978-3-642-87928-9

[10] Takeda T, Hashizume T. Differences of tensile strength distribution between mechanically high-grade and low-grade Japanese Larch Lumber II: Effect of knots on tensile strength distribution. Journal of Wood Science, 1999; 45(3): 207-212. https://doi.org/10.1007/BF01177727

[11] Reiterer A, Stanzl-Tschegg SE. Compressive behaviour of softwood under uniaxial loading at different orientations to the grain. Mechanics of Materials, 2001; 33:705-71. https://doi.org/10.1016/S0167-6636(01)00086-2

[12] Mishra A. Dry sliding wear of teak wood -epoxy composites. 2015; 13(8): 13-23.

[13] Dwivedi UK, Navin C. Influence of wood flour loading on tribological behavbiour of epoxy composites, Polymer Composites, 2008; 29 (11): 1189-1192. https://doi.org/10.1002/pc.20548

[14] Ameen HA, Hassan KS, Mubarak EMM. Effect of loads, sliding speeds and times on the wear rate for different materials. American Journal of Scientific and Industrial Research, 2011, 2(1): 99-106 https://doi.org/10.5251/ajsir.2011.2.1.99.106

[15] Alshammari FZ, Saleh KH, Yousif BF, Alajmi A, Shalwan A, Alotaibi JG. The influence of fibre orientation on tribological performance of jute fibre reinforced epoxy composites considering different mat orientations. Tribology in Industry, 2018; 40(3): 335-348. https://doi.org/10.24874/ti.2018.40.03.01

[16] McArthur H. Engineering Materials Science, Properties, uses, degradation and remediation. 1st edition, Woodhead publishing limited, Philadelphia: USA; 2004.

[17] Persson K. Micromechanical modelling of wood and fibre properties. Department of Mechanics and Materials, Doctoral Thesis, LTH, Lund University, Sweden; 2000.

[18] Briscoe BJ, Sinha SK. Wear of polymers. Proceedings of the Institution of Mechanical Engineers, Part J: Journal of Engineering Tribology, 2002; 216(6): 401-413. https://doi.org/10.1243/135065002762355325

[19] Sarkar P, Modak N, Sahoo P. Effect of normal load and velocity on continuous sliding friction and wear behavior of woven glass fiber reinforced epoxy composite. Materials Today: Proceedings, 2017; 4(2): 3082-3092. https://doi.org/10.1016/j.matpr.2017.02.191

[20] Sudheer M. Evaluation of abrasive wear behavior of dual ceramic whisker reinforced epoxy composites. Materials Discovery, 2016; 6: 17-27. https://doi.org/10.1016/j.md.2017.04.002

[21] Murase Y. Friction of wood sliding on various materials. Journal- Faculty of Agriculture, Kyushu University, 1984; 28: 147-160.

[22] Bryant, PJ, Lavik M, Salomon G. Mechanisms of Solid Friction. American Elsevier Publishing Company, New York, USA; 1964.

[23] Stalnaker JJ, Harris EC. Structural Design in Wood. Newyork: Springer Science; 1989. https://doi.org/10.1007/978-1-4684-9996-4

[24] Bhushan B. Tribology and Mechanics of Magnetic Storage Devices. 2nd edition, Springer-Verlag, New York, USA; 1996. https://doi.org/10.1007/978-1-4612-2364-1

[25] Blau, PJ. Scale Effects in Sliding Friction: An experimental study, in fundamentals of friction: macroscopic and microscopic processes, Kluwer Academic, Dordrecht, Netherlands; 1992. https://doi.org/10.1007/978-94-011-2811-7_26

[26] Chowdhury MA., Khalil MK., Nuruzzaman DM., Rahaman ML. The effect of sliding speed and normal load on friction and wear property of aluminum. International Journal of Mechanical & Mechatronics Engineering, 2011; 11: 53-57.

[27] Lorna JG. The hierarchical structure and mechanics of plant materials, Journal of the Royal Society Interface, 2012; 9(76): 2749-2766. https://doi.org/10.1098/rsif.2012.0341

[28] Daval V, Pot G, Belkacemi M, Meriaudeau F, Collet R. Automatic measurement of wood fiber orientation and knot detection using an optical system based on heating conduction. Optics Express, 2015; 23(26): 33529-33539. https://doi.org/10.1364/OE.23.033529

[29] Goring DAI, Timell TE. Molecular weight of native cellulose. Tappi, 1962; 45(6): 454-460.

Research Article

The electroless metal plating process over ABS plastic by using ionic liquids

Canan Uraz*

Department of Chemical Engineering, Engineering Faculty, Ege University, Turkey.

Article Info	Abstract
	Electroless metal plating is a coating technique which relies on reduction of metal ions with an autocatalytic chemical reduction process. Ionic liquids are defined as compounds that are sensitive to the environment due to their low pressure that can be negligible, their high heat resistance, and a higher ionic conductivity, to be electrochemically rich, to have wide open liquid range, to have a range of high polar solubility. In this study, the effects of ionic liquids were investigated in the electroless metal plating process over ABS plastic. For this purpose electroless baths were prepared by using two different types of ionic liquids (EMIC & DCA) for copper and nickel plating. Experiments were carried out with 120-500 grit sandpaper and at 80°C plating bath temperature for 30-120 minutes of deposition time and at different pH values as 8-9. X-Ray XDL-B System, X-ray Diffraction (XRD) and Scanning Electron Microscopy (SEM) were used for the characterization and the amount of deposits. According to the experimental and analytical results, the metal plating on ABS plastic was succeeded with two different ionic liquid additions. On the contrary of the traditional processes with chromic and sulphuric acids, the etching and the plating processes were performed with environmentally friendly chemicals. In this way, both it will be provided a significant benefit to public health, and it will be brought innovation to the metal plating industry with the environmentally friendly ionic liquid catalyst.

1. Introduction

Acrylonitrile butadiene styrene (ABS) is a thermoplastic polymer made by polymerizing styrene and acrylonitrile in the presence of polybutadiene. 15 to 35% acrylonitrile, 5 to 30% butadiene and 40 to 60% styrene are the composition of ABS. Plating of plastic materials is providing a long term use to the materials. Especially ABS plastic is very suitable to this work. ABS plastic is an important chemical reagent an engineering material with high thermal stability, high mechanical strength and high resistance [1]. Ionic liquids (ILs) are electrically conductive liquids composed merely of ions. Ionic liquids at room temperature (RTIL) are the salts having very low gas pressure or close to zero. So missing amount of ionic liquids are little both evaporation or using as catalyst or solvent at high temperature. They have a wide liquid range and are very stable at high temperature. Two types of room temperature ionic liquids are EMIC, 1-ethyl-3-methyl imidazolium chloride ($C_6H_{11}N_2Cl$) and DCA, 1-ethyl 3-methylimidazolium dicyanamide ($C_8H_{11}N_5$). For instance 1-ethyl 3-methyl imidazolium trifloromethylsufonit has a liquid range of 471^0C with melting point -15^0C and deformation temperature 455^0C [2]. The characteristic make RTILs applicative for reactions [3]. At the research conducted with RTIL has positive effect on the

plating performance. In the study, while aluminum did not coat in the electrolitic aqueous solution, at the room temperature the plating is performed with ionic liquid [4]. At the other study, 1-ethyl 3- methyl imidazolium dicyanamide is used for nickel plating and this ionic liquid is approved for metal plating electrode [5]. Electroless plating is the main part of the electroplating process. In this part plastic material has a conductive behavior. It provides homogeneous distribution, durability and preferred thickness. It is nonmagnetic and because of the higher stretching ratio there is no break into pieces under distortion or elongation. The difference of the electroless plating from the electroplating is about energy. Electroless plating does not need electrical energy. So the plating film appears with uniform structure. This method is widely used because of superior features such as providing uniform surface film and resistance of abrasion and corrosion [6, 7]. At related studies, catalysts and activation solutions for the electroless bath are mainly consisting of colloidal suspension of palladium metal and tin ions. The function of the bath is precipitating colloidal palladium (palladium-tin) on the porous ABS surface. Palladium is used as catalyst and the nickel and copper electroless precipitation reaction is begun. Two metals (nickel and copper) are most widely used metals at the decorative plating of the plastics [8-10]. Electroless metal plating technique begins to apply by using catalyst. Many researchers have attempted to deposit metals by using electroless plating technique. For example, electroless nickel and copper plating was obtained over carbon nanotubes and graphite [8, 11]. Fukuhara and coworkers implemented electroless plating process by preparing copper surface catalysts [12]. At another study, Song and friends coated silver by using nickel phosphite catalyst [13]. The surface characterization of the activated ABS plastic was obtained by using Scanning Electron Microscopy (SEM) and Ni coating was also characterized by X-Ray diffraction (XRD) [1].

The main goal of this study is to search the effects of ionic liquids in the electroless metal plating process over ABS plastic. For this purpose electroless baths were prepared by using environmentally friendly chemicals (EMIC & DCA) for copper and nickel plating processes on ABS plastic. On the contrary of the traditional processes with chromic and sulphuric acids, the etching and the plating processes were performed with environmentally friendly chemicals.

2. Material and Method

The electroless copper and nickel plating on ABS plastic material experiments were performed in fume hood at atmospheric pressure and at different plating temperatures. The experiments consist of four steps: preparing the chemicals and materials, etching, plating and the analysis of samples. The investigated parameters were sandpaper size, plating time, plating temperature and effects of ionic liquid types (RTIL).

2.1 Electroless metal plating procedure

1. Initially, 20 mm x 35 mm x 1.5 mm ABS plastic samples are grounded with the 120-320-500 grit sandpaper size.
2. Then the samples are dried in a 65^0C oven for 4 to 5 h.
3. And then the samples are taken from oven and layered in a 10g/L NaOH alcoholic solution.
4. After then, this NaOH alcoholic solution is placed in a water bath at 35-40 ^{0}C for 30 min.
5. Then, the samples are put in a mixture. The composition and the amounts of the chemicals are given in Table 1.

Table 1. Chemicals and amounts of aqueous solution [14]

Chemical	Density (g/ cm3)	Mass (g)	Volume (mL/L)
HNO_3	1.51	378.2 - 453.9	250 - 300
H_2O_2	1.45	13.6 – 20.41	9.38 – 14.08
NH_4F	1.009	2 - 4	1.98 – 3.96

6. Prepared mixture is replaced in an ultrasonic bath for 30 min [14].
7. The resultant samples are washed with deionized water.
8. For the material pretreatment solution of $CuCl_2$ and ionic liquid are weighed with the molar ratio 2:1 and the specimen is immersed in the ionic solution and is left for a week.
9. The specimen is placed at 80^0C plating bath containing the plating solution prepared with the chemicals at Table 2 and Table 3 for Copper and Nickel plating, respectively.

Table 2. Contents of the plating bath for Copper [14]

Chemical	Formula	Concentration (g/L)
Copper Sulfate	$CuSO_4 \cdot 5H_2O$	12-15
EDTA-2Na	$C_{10}H_{14}N_2Na_2O_8 \cdot 2H_2O$	40-45
2,2-Dipyridyl	$C_{10}H_8N_2$	0.04-0.05
Formalin	CH_2O	20-25

Table 3. Contents of the plating bath for Nickel [15]

Chemical	Formula	Concentration (g/L)
Nickel Chloride	$NiCl_2 \cdot 6H_2O$	20
Sodium Hypophosphate	$NaH_2N_2PO_3 \cdot H_2O$	20
Sodium Citrate	$Na_3C_6H_5O_7 \cdot H_2O$	45
Ammonium Chloride	NaH_4Cl	30

10. NaOH is added slowly to the plating bath to adjust the pH. For Copper plating, pH is adjusted at 11-12 and for Nickel plating, this pH value is adjusted at 8-9.
11. At the beginning of the process (10 min to 20 min), no bubbles are seen. But after 50 min to 60 min, a lot of bubbles are obtained according to the reaction.
12. Then samples are purified with deionized water and then the metal plated sample is dried at 45 ^0C in an oven.
13. At the end of the experiments, some characterization techniques (XRD, SEM-EDX) and the plating amount of the final samples (X-Ray XDL-B System) are obtained.

3. Results and Discussions

The results of the analyses were evaluated and the effects of plating time and sand paper size on the amount of deposits were investigated. According to the obtained results amount of deposits versus plating time and sand paper size graphs were plotted (Figures 1-4).
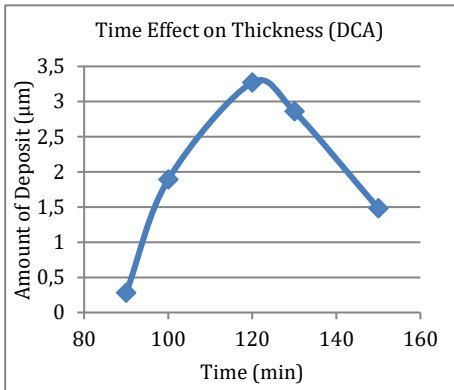
Fig. 1 Time Effect on Amount of Deposit for DCA and 120 grit size Sandpaper.
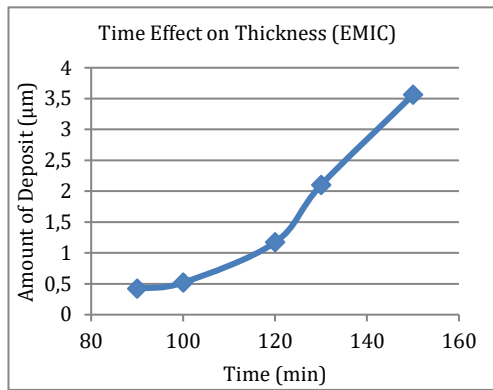
Fig. 2 Time Effect on Amount of Deposit for EMIC and 120 grit size Sandpaper.

According to the results from X-Ray analysis of DCA, stable increase could not be obtained. When plating time increases, firstly the amount of deposit increases from 0.28 to 3.27; however, after 120 min, it decreases from 3.27 to 1.48. But the amount of deposit decreased with increasing plating time of the substrate at constant temperature (80^0C) for DCA. The maximum amount of the deposit is found as 3.27 µm for 120 min by using DCA (Figure 1). The amount of deposit increased with increasing plating time of the substrate at constant temperature (80^0C) by using EMIC (Figure 2). The maximum amount of the deposit was about 3.67 µm for 150 min for EMIC. As a result, it is concluded that EMIC is more suitable ionic liquid then DCA type ionic liquid as catalyst for metal plating on ABS plastic.

Results obtained from X-Ray analysis are evaluated and thickness versus sandpaper size graphs are plotted (Figures 3, 4). It is shown from Figure 4 that, the thickness of the copper film increases when sandpaper size increases by using EMIC. The maximum amount of the deposit was about 3.92 µm for 500 grit of sand paper. Although sandpaper size increases, increase in the thickness of the copper film could not be obtained by using DCA (Figure 3). The reason can be stated that stable increase could not be obtained according to the ingredients of plating bath solution that includes nitric acid, hydrogen peroxide and ammonium fluoride.

After X-ray measurements, the XRD and SEM analyses were performed for the best plated specimens. Figures 5 and 6 were obtained for Cu and Ni plating process, respectively. It can be said from these figures that, there are only Cu (Fig. 5) and Ni (Fig.6) peaks and no additional elements beside them. According to the literature, the results of XRD analysis were obtained as expected [14, 1]. Diffraction peaks were obtained at approximately 45, 50, and 75 degree for Copper and at 20, 35 and 45 degree for Nickel.
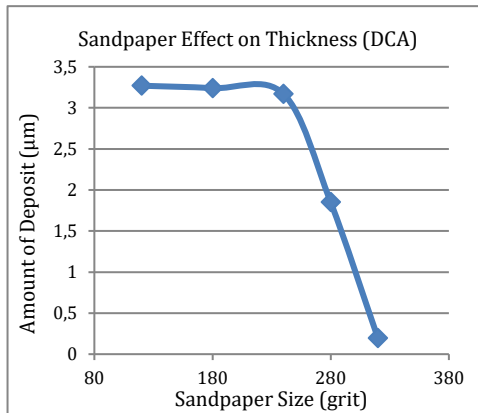
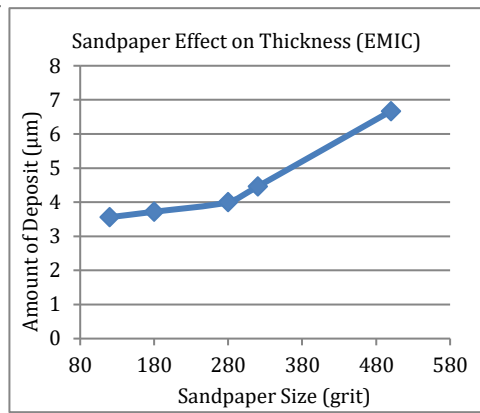Fig. 3 Amount of Deposit versus Sandpaper Size for DCA and 120 minutes.

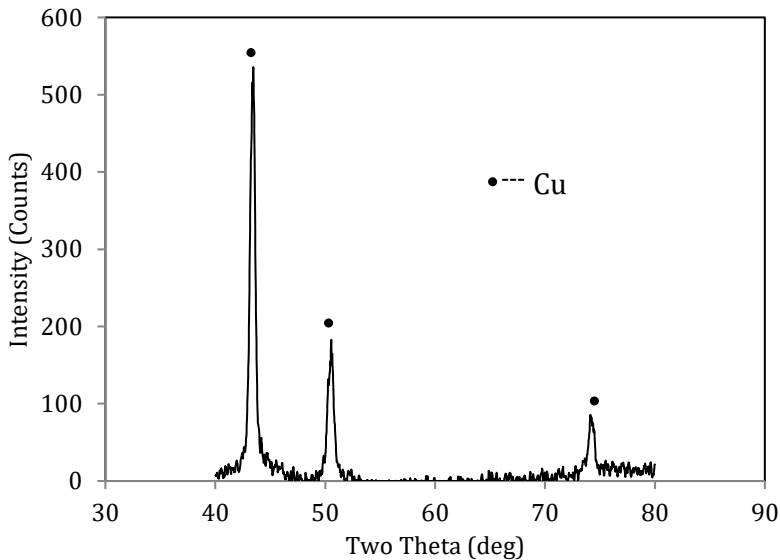Fig. 4 Amount of Deposit versus Sandpaper Size for EMIC and 120 minutes.

Fig. 5 XRD Analysis for Copper plating with EMIC.

A SEM analysis was obtained for the surface of the Cu and Ni-plated specimens using RTIL. Morphology of deposits are shown in Figures 7 and 8, so materials were deposited on the surface of the substrate and these proves that electroless plating took place. The elemental mapping result using SEM-EDS also indicated that the plating film consisted of Copper and Nickel only, and the metal was homogeneously distributed on the surface of the film.
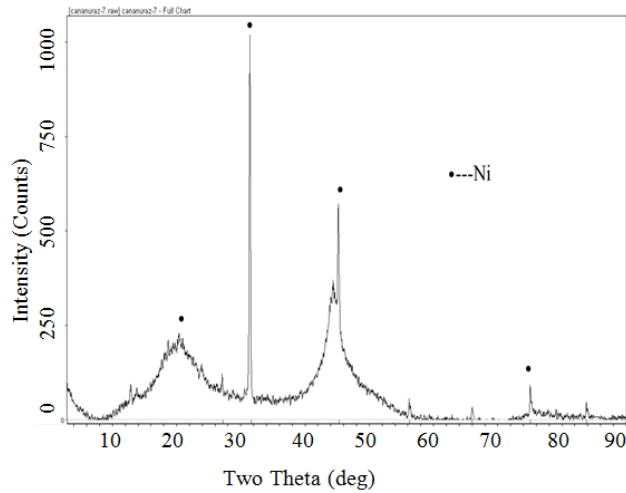
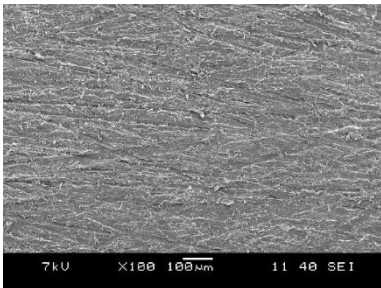Fig. 6 XRD Analysis for Nickel plating with EMIC.

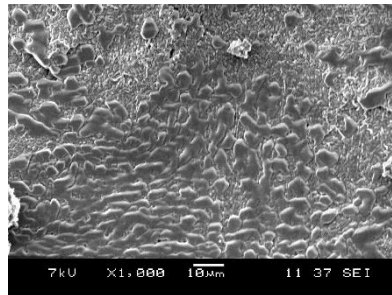Fig. 7 SEM Analysis of copper plated sample which obtained by using EMIC with 120 grit size sandpaper at 60 minutes.

Fig. 8 SEM Analysis of nickel plated sample which obtained by using EMIC with 120 grit size sandpaper at 60 minutes.

4. Conclusion

The effects of ionic liquids were investigated in the electroless metal plating process over ABS plastic in this experimental study. For this purpose two different electroless baths were prepared by using environmentally friendly chemicals (EMIC & DCA) for copper and nickel plating processes on ABS plastic. On the contrary of the traditional processes with chromic and sulphuric acids, the etching and the plating processes were performed with environmentally friendly chemicals. The investigated parameters were the thickness of plate, plating time, sandpaper size effect on the plating amount in the electroless metal plating process over ABS plastic. From the results of this experimental study, the following conclusions can be drawn:

- It is succeeded in demonstrating the electroless plating of dense, smooth, and pure copper and nickel from a RTIL, EMIC.

- The maximum amount of the deposit was achieved about 3.67 μm for 150 min for EMIC.
- XRD results indicated that the deposited films were copper and nickel. The plating film consisted of Copper and Nickel only, and the metals were plated over the surface of the ABS plastic homogeneously.
- The elemental mapping results of SEM-EDS indicated that the plating film consisted of Copper and Nickel only, and the metals were homogeneously distributed on the surface of the film.
- It was concluded that, EMIC that was one of the room temperature ionic liquid used in this experimental study was more suitable ionic liquid then DCA type ionic liquid as catalyst for electroless metal plating on ABS plastic.
- On the contrary of the traditional processes with chromic and sulphuric acids, the etching and the plating processes were performed with environmentally friendly chemicals. In this way, both it will be provided a significant benefit to public health, and it will be brought innovation to the metal plating industry with the environmentally friendly ionic liquid catalyst.

Acknowledgements

References

[1] Tang XBC, Han C., Zhang B. A New Palladium Free Surface Activation Process for Ni Electroless Plating on ABS Plastic. Materials Letters, 2009; 63: 840-842. https://doi.org/10.1016/j.matlet.2009.01.006

[2] Ngo HL, LeCompte K., Hargens L., McEwen AB. Thermal properties of imidazolium ionic liquids. Thermochimica Acta, 2000; 357-358, 97-102. https://doi.org/10.1016/S0040-6031(00)00373-7

[3] Murugesan S, Linhardt RJ. Ionic liquids in carbohydrate chemistry-current trends and fture directions. Current Organic Synthesis, 2005; 2: 437-451. https://doi.org/10.2174/157017905774322640

[4] Koura N, Nagase H, Sato A, Kumakura S, Takeuchi K, Ui K, Tsuda T, Loong C K. Electroless Plating of Aluminum from a Room-Temperature Ionic Liquid Electrolyte. Journal of Electrochemical Society, 2007; 155: 155-157. https://doi.org/10.1149/1.2817880

[5] Deng MJ, Sun IW, Chen PY, Chang JK, Tsai WT. Electrodeposition behavior of nickel in the water- and air-stable 1-ethyl-3-methylimidazolium-dicyanamide room-temperature ionic liquid. Electrochimica Acta, 2008; 53(19):5812-5818. https://doi.org/10.1016/j.electacta.2008.03.040

[6] Linka G, Riedel W. Galvanotechnik, 1987; 568.

[7] Kılıçarslan A, Toptan F, Kerti I. Akımsız Nikel Kaplama Yöntemi ve Seramik Partiküllerine Uygulanması, Türk Mühendis ve Mimar Odaları Birliği Metalurji Mühendisleri Odası, http://www.metalurji.org.tr/dergi/dergi154/d154_3337.pdf

[8] Ang LL, Hor TSA, Xu GQ, Tung CH, Zhao SP, Wang JLS. Decoration of Activated Carbon Nanotubes with Copper and Nickel. Carbon, 2000; 38: 363-372. https://doi.org/10.1016/S0008-6223(99)00112-8

[9] Liu Z, Chen Y. Spectroscopic Studies on Tetragonal ZrO_2-Supported MoO_3 and NiO-MoO_3 Systems. Journal of Catalysis, 1998; 17: 314-324. https://doi.org/10.1006/jcat.1998.2123

[10] Rudnik E, Kokoszka K, Łapsa J. Comparative Studies on the Electroless Deposition of Ni-P, Co-P and Their Composites with SiC Particles. Surface & Coatings Technology, 2008; 202: 2584-2590. https://doi.org/10.1016/j.surfcoat.2007.09.026

[11] Caturla F, Molina F, Molina-Sabio M, Rodriguez-Reinoso F, Esteban A. Electroless Plating of Graphite with Copper and Nickel. Journal of Electrochemical Science, 1995; 142: 4084-4091. https://doi.org/10.1149/1.2048468

[12] Fukuhara C, Ohkura H, Gonohe K, Igarashi A. Low-Temperature Water-Gas Shift Reaction of Plate-Type Copper-Based Catalysts on an Aluminum Plate Prepared by Electroless Plating. Applied Catalysis A: General, 2005; 279: 195–203. https://doi.org/10.1016/j.apcata.2004.10.036

[13] Song L, Li W, Wang G, Zhang M, Tao K. A New Route to Prepare Supported Nickel Phosphide/Silica-Alumina Hydrotreating Catalysts from Amorphous Alloys. Catalysis Today, 2007; 125: 137-14. https://doi.org/10.1016/j.cattod.2007.02.033

[14] Luo LM, Lu Z, Huang X, Tan X, Ding X, Cheng J, Zhu L, Wu Y. Electroless Copper Plating on PC Engineering Plastic with a Novel Palladium-Free Surface Activation Process. Surface & Coating Technology, 2014; 251: 69-73. https://doi.org/10.1016/j.surfcoat.2014.04.005

[15] Sudagar J, Lian J, Sha W. Electroless nickel, alloy, composite and nano coatings - A critical review. Journal of Alloys and Compounds, 2013; 571: 183-204. https://doi.org/10.1016/j.jallcom.2013.03.107

Research Article

Compression after impact properties of glass fiber/epoxy/MWCNT composites

Özgür Demircan*

Metallurgical and Materials Engineering Department, Faculty of Engineering, Ondokuz Mayıs University, Samsun, Turkey
Department of Nanoscience and Nanotechnology, Graduate School of Science, Ondokuz Mayıs University, Samsun, Turkey

Article Info	Abstract
	Glass fiber/epoxy resin/multi-walled carbon nanotubes (MWCNTs) were used to fabricate the nano materials integrated thermoset composite materials in this study. Thermoset composites with and without nano materials were fabricated using resin transfer molding (RTM) methods. The fabricated samples were tested with compression after impact and charpy impact tests. The samples with MWCNTs demonstrated the best improvement of the compression after impact modulus and strength with 31% and 5.6% compared to the samples without carbon nanotubes. The nano materials integrated specimens showed 10.2% improvement of charpy impact strength against specimens without carbon nanotubes in 90° degree direction. Due to the existing of the carbon nanotubes between fiber and polymer matrix was the reason of the improvement of the mechanical properties of carbon nanotubes integrated composites.

1. Introduction

The using of thermoplastics and thermosets polymeric composite materials were considerably developed in recent years. Nano materials can be used as an assistant factor for strengthening of the composites. Carbon nanotubes (CNTs) have superior properties such as, strength and stiffness, with high aspect ratio. Because of unique properties of CNTs (such as Young's modulus of ca. 1 TPa and tensile strength of ca. 200 GPa), CNTs has become an ideal candidate for polymer reinforcement [1].

In the literature, some studies were done about the mechanical properties of CNT modified laminates [2-6]. Flexural properties of glass fiber/epoxy/MWCNT composites were investigated by Demircan et al [2]. In their study, MWCNTs integrated specimens showed the best improvement of the flexural modulus and strength with 19% and 7% compared to the samples without MWCNTs. Bilisik et al. [3] studied short beam shear of nanoprepreg/nanostitched three dimensional carbon/epoxy multiwall carbon nanotubes composites. They found that stitching and MWCNTs addition enhanced the short-beam strength of the composites. Bilisik et al. [4] studied mechanical properties of plain para-aramid/phenolic multiwall carbon nanotubes prepreg/multistitched preform composites. In their study, the fracture toughness (GIC) of the stitching and nanostitched composites showed 42 fold and 41 fold (beam theory), 18 fold and 21 fold (modified beam theory) increased compared to the control. Preparation and mechanical properties of carbon

*Corresponding author: ozgur.demircan@omu.edu.tr
orcid.org/0000-0001-8235-3966

nanotube grafted glass fabric/epoxy multi-scale composites were investigated by Eskizeybek et al [5]. Tensile tests were conducted on fabricated multi-scale composites, indicating the grafting CNTs on glass fabric resulted a decrease (11%) in ultimate tensile strength while toughness of the multi-scale composite laminates were increased up to 57%. Mode I interlaminar fracture toughness of chemically carbon nanotube grafted glass fabric/epoxy multi-scale composite structures were investigated by Eskizeybek et al [6]. Grafting CNTs onto PWGFs improved both initial and steady-state toughness more than double as measured by Mode I interlaminar fracture testing.

In the literature, some articles were found addressing the compression-after-impact (CAI) properties of CNT modified laminates [7-11]. Mannov et al. [7] studied improvement of compressive strength after impact in fibre reinforced polymer composites by matrix modification with thermally reduced graphene oxide. They significantly improved residual compressive properties of the laminates for the modified specimen, with the glass fibre laminates showing the highest improvement of 55% when compared to unmodified specimens. Gorbatikh et al. [8] studied impact and residual after impact properties of carbon fiber/epoxy composites modified with carbon nanotubes. They showed that CNTs network had a positive influence on the properties of the composites. Ye et al. [9] reviewed interlaminar fracture toughness and CAI strength of fibre-reinforced composites with nanoparticles. They reviewed that nanoparticles as additional reinforcing phases in fibre-reinforced polymer (FRP) laminates (especially with brittle thermosetting resins) can enhance interlaminar fracture toughness and CAI strength.

In the literature, few articles were found addressing the charpy impact properties of CNT modified laminates [12-13]. Sharma et al. [12] reported impact behavior and fractographic study of carbon nanotubes grafted carbon fiber-reinforced epoxy matrix multi-scale hybrid composites. In this study, CNTs grafted carbon fiber epoxy composites showed 48.7% and 42.2% higher energy absorption compared to reference composites in charpy and izod impact tests. Structural composites hybridized with epoxy compatible polymer/MWCNTs nanofibrous interlayers was studied by Papila et al. [13]. They found that interlayered charpy impact specimens absorbed 20% more energy than the non-interlayered ones.

In the literature, it was found some researchers who they coated the surface of the reinforcements using nano materials. Lagoudas et al. [14] studied effect of carbon nanotubes on the interfacial shear strength of T650 carbon fiber in an epoxy matrix. Their results of the single-fiber fragmentation tests indicated an improvement in interfacial shear strength with the addition of a nanotube coating. Kim et al. [15] studied tensile strength of glass fibers with carbon nanotube–epoxy nanocomposite coating. They found that a more uniform strength distribution and higher strengths of the rovings impregnated with the CNT nanocomposite than those impregnated with the neat epoxy. The effect of adding carbon nanotubes to glass/epoxy composites in the fibre sizing and/or the matrix was reported by Godara et al. [16]. They found that an increasing in resistance of crack initiation fracture toughness by +10% by the presence of CNTs in the sizing, but a lowering in crack propagation toughness of -53%. Interfacial shear strength of a glass fiber/epoxy bonding in composites modified with carbon nanotubes was reported by Gorbatikh et al. [17]. The results of their tests revealed that an increase of interfacial shear strength (IFSS) in specimens.

Wang et al. [18] studied an effective surface modification of carbon fiber (CF) for improving the interfacial adhesion of polypropylene (PP) composites. They significantly enhanced the mechanical performance of PP composites with 0–30 wt. % CFs by CF surface treatment in combination with maleic anhydride grafted PP (MAPP) modification. Demircan et al. [19] investigated the effect of CNTs on the mechanical properties of

LPET/glass fiber thermoplastic composites. They found about 7% and 33% in tensile and flexural modulus and about 3% and 65% in tensile and flexural strength of composites by using carbon nanotubes in the fiber sizing.

In the literature, to the best of the authors' knowledge, it was found no research about the compression after impact and charpy impact properties of the glass fiber/epoxy resin/MWCNTs integrated thermoset composites reinforced with the biaxial warp-knitted fabrics. The purpose of this research was to study the effect of the nano material incorporation on the CAI and charpy impact properties of the thermoset composites. The CAI and charpy impact properties of 0.0 wt% and 0.4 wt% MWCNTs incorporated specimens were investigated. In order to design of the new thermoset composite materials, the results from our research can be used.

2. Experimental procedure

2.1. Constituents of Thermoset Composites

In order to fabricate nano materials integrated thermoset composites, the non-crimp fabrics (NCF) with glass fibers (Metyx Composites Ltd., Turkey), epoxy resin (DTE 1200, Duratek, Turkey) and hardener (DTS 1155, Duratek, Turkey) were used. The properties of the NCF are shown in Table 1.

Table 1 Properties of non-crimp fabric (NCF) of composites

E glass samples	Biaxial yarn 0° (warp) fibers, tex	Biaxial yarn 90° (weft) fibers, tex	Area weight of 0° warp fibers (g/m²)	Area weight of 90° weft fibers (g/m²)	Fabric weight (warp, weft and binding fibers) (g/m²)
LT1200E 05B 0/90	2400	1200	566	614	1187

The carbon nanotubes were supplied from Ege Nanotek Kimya Sanayi Limited Sirketi, Izmir, TURKEY. The properties of the MWCNTs were demonstrated in Table 2.

Table 2 Properties of MWCNTs

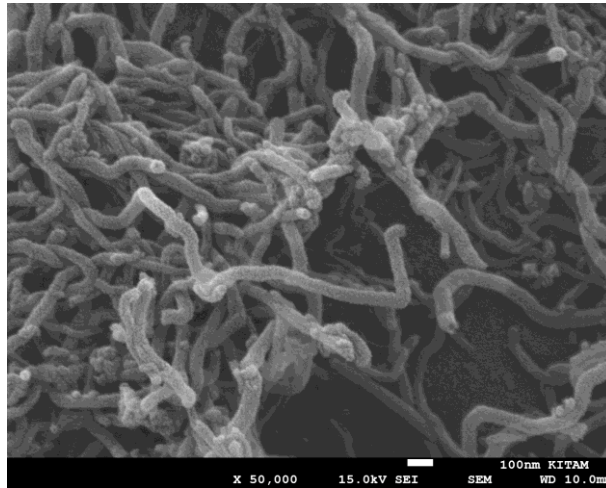| Parameter	Value
Outer diameter (nm)	10-20
Interior diameter (nm)	5-10
Length (μm)	10-30
Surface area (m2/g)	>200
Color	black
Electrical conductivity (S/cm)	>100
Density (tap) (g/cm3)	0.28
Density (true) (g/cm3)	2.1

Fig. 1 SEM images of MWCNTs

2.2. Fabrication Method of Thermoset Composites

In order to fabricate the thermoset composites with nano materials, the resin transfer method (RTM) was chosen to manufacture four layers biaxial warp-knitted (BWK) reinforced composites plates as shown in Figure 2.

At first ethanol and MWCNTs solutions were prepared to coat each faces of the NCFs. MWCNTs were dispersed in ethanol using a magnetic stirrer device. After that the solution of MWCNTs and ethanol were stayed in an ultrasonic bath. Later, each faces of the NCFs were coated using of the solution of MWCNTs and ethanol. After coating of the NCF with the MWCNTs solution, the specimens were left for two days in the room temperature to evaporate of the ethanol. Then, MWCNTs coated four layers fabrics were laid in mold cavity in a symmetrical stacking sequence ($[90_{wa}/0_{we}/90_{wa}/0_{we}]_s$) of the RTM system (Figure 3).
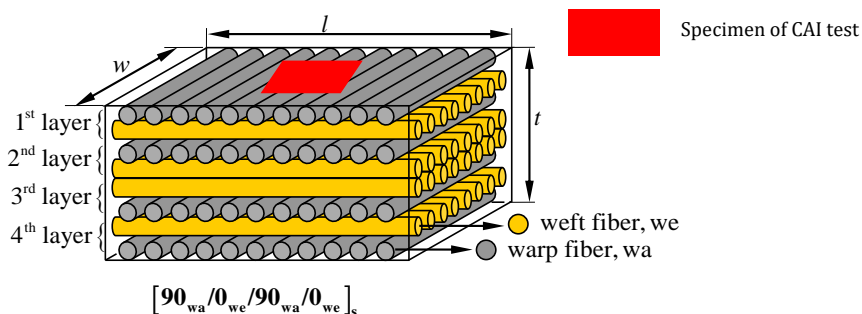

Fig. 2 The RTM apparatus

Fig. 3 Schematic drawing of the thermoset composites. Here, l: length, w: width and t: thickness of the fabricated composite plate

Table 3 Fiber volume fraction and thickness of fabricated composites

Composites	Weft Vf (%)	Warp Vf (%)	Binding Vf (%)	Total (warp, weft and binding) Vf (%)	Thickness (mm)
0.0 wt % MWCNT	17.4	16.1	0.66	34.2	5.4
0.4 wt % MWCNT	16.8	18.2	0.28	35.3	5.0

2.3. Characterization of Thermoset Composites

Zwick Roell Z250 KN Universal test equipment was used for both low velocity drop weight impact and CAI tests. The weight and diameter of the impactor was 6490 g and 12.9-mm. After completing the low energy impacts tests with 43 J, the damaged samples were used for the CAI tests. Impactor was able to damage the surface of the composite plate at 43 J. Therefore, 43 J impact energy level was chosen. The CAI tests were conducted on specimens with constant displacement of 0.5 mm/min. A 250 kN unit cell was used in the CAI tests. The CAI tests were performed on specimens using EN 6038 test standard. Three specimens were tested in the CAI tests. In the CAI tests, the specimens were placed in an anti-buckling jig where both loaded edges were fully clamped. In order to prevent global buckling the sides were simply supported in the CAI tests. The sample dimensions were: 150 mm in length, 100 mm in width and 5.0-5.4 mm in thickness in the compression after impact tests.

Charpy impact tests were performed in accordance with the ISO 179 testing standards with an impact hammer of 5 J energy capacity. In the charpy impact tests, three specimens were tested in the 90° directions for each type of the composite panels. The sample dimensions were: 90 mm in length, 15 mm in width and 5.0-5.4 mm in thickness in the charpy impact tests.

3. Results and Discussion

The surface morphologies of glass fibers after grafting CNTs are investigated via SEM as shown in Figure 4. The glass fiber surface was fairly grafted by CNTs but non-grafted regions were also observed (Figure 4a). According to this observation, the carbon nanotube grafting process forms of CNT inlets on the glass fiber surfaces. The high magnification SEM image of the individual CNT grafted glass fiber is shown in Figure 4b. The grafted CNTs on the fiber surface exhibit randomly oriented with non-uniform dispersion and fairly agglomerated areas were also observed.
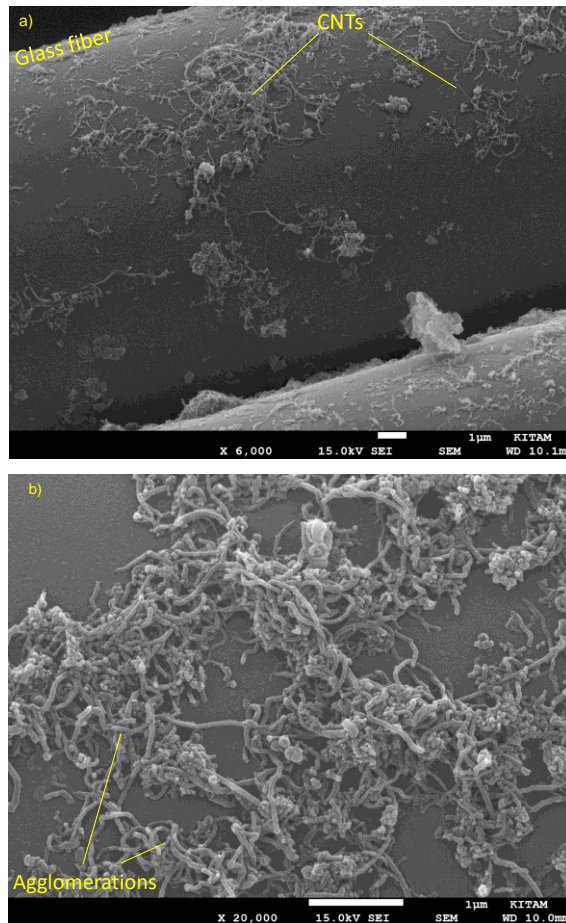
Fig. 4 SEM images of surface morphologies of glass fibers after grafting CNTs

Figure 5, 6 a and b represent the results of the CAI stress-strain curves and modulus and strength of the specimens of the thermoset composites with 0 wt% and 0.4 wt% MWCNTs. The CAI modulus and strength of the specimens with 0 wt% and 0.4 wt% MWCNTs were 0.55 GPa and 177.6 MPa and 0.80 GPa and 188.3 MPa. The CAI modulus and strength of the specimens with 0.4 wt% MWCNTs were 31% and 5.6% higher compared to the 0.0 wt% MWCNTs.

The RTM fabrication process of the composite laminates includes the post-curing step at 80 °C and this step could induce the formation of chemical bonds between functional groups on the MWCNTs and the glass fiber surfaces. The possible reason for the obtaining the improved CAI properties for the specimens incorporated with the MWCNTs was the synergy between fiber and matrix, which was created by the MWCNTs in the composite material. Since the CNTs having superior mechanical properties with large surface area, they improve mechanical properties of composites.

Comparing these results with others found in the literature, 0% and 7% in improvements in CAI strength for laminates with 5 wt% and 10 wt% of cup-stacked CNTs was reported by Yokozeki et al. [10]. 12–15% increase in CAI strength for nano-enhanced laminates containing 0.5 wt% MWCNTs was reported by Kostopoulos et al. [11]. 55% increase in CAI strength for nano-enhanced laminates containing 0.5 wt% MWCNTs was reported by Mannov et al. [7]. The good agreement between our results and literature supported our mechanical tests.
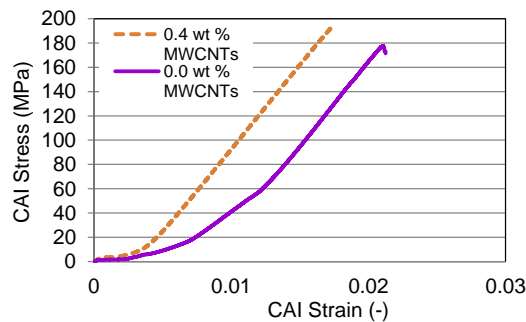

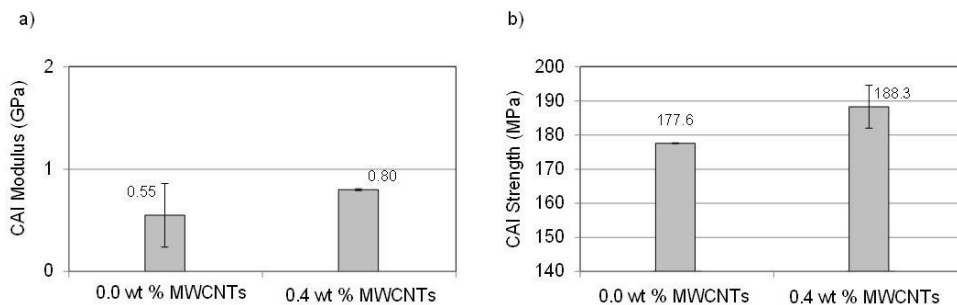Fig. 5 Results of CAI stress-strain properties of thermoset composites

Fig. 6 Results of CAI modulus and strength properties of thermoset composites

Figure 7 shows the results of the charpy impact properties of the specimens of the thermoset composites with 0 wt% and 0.4 wt% MWCNTs in the 90° direction. The charpy impact strength of the specimens with 0 wt% and 0.4 wt% MWCNTs were 162.9 kJ/m^2 and 181.4 kJ/m^2 in 90° direction. The CNT integrated specimens showed 10.2% improvement of the charpy impact strength against specimens without CNTs in the 90° degree direction. As mentioned earlier, the possible reason for the improvement in the

charpy impact strength might be the synergy between the fiber and matrix, which was created by the MWCNTs in the composites.
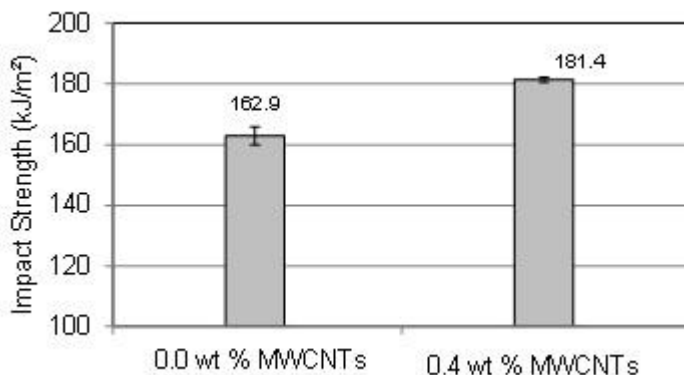

Fig. 7 Results of charpy impact properties of thermoset composites

The influence of addition of CNTs on the energy absorption properties of composites has been studied by various researchers. 48.7% higher energy absorption in charpy tests from the fabricated composites with MWCNTs was reported by Sharma et al. [12]. 20% increase in the charpy impact energy absorbance in the presence of 0.2 wt % MWCNTs interlayers was reported by Papila et al. [13].

4. Conclusions

The addition of the carbon nanotubes on the surface of the reinforcements enhanced the CAI modulus and strength and impact strength of the thermoset composites.

From the results of this study, the following conclusions can be drawn:

- The best improvement of the CAI modulus and strength with 31% and 5.6% were obtained from the specimens with 0.4 wt% MWCNTs due to the superior properties of carbon nanotubes.
- The highest results of charpy impact strength were achieved with 0.4 wt% MWCNTs.
- There was a good agreement of results of the CAI and impact tests of nano materials integrated composites from literature and from us.

In future study, we will try to investigate the interlaminar sheer strength properties of the nano materials integrated composite materials with the NCFs reinforcements.

Acknowledgment

References

[1] Meyyappan M. Carbon Nanotubes Science and Applications, CRC Press, New York, ISBN 9780849321115, 2005. https://doi.org/10.1201/9780203494936

[2] Demircan Ö, Çolak P, Kadıoğlu K, Günaydın E. Flexural properties of glass fiber/epoxy/MWCNT composites. Research on Engineering Structures and Materials, 2019; 5 (2): 91-98.

[3] Bilişik A, Sapanci E, Karaduman N. Short beam shear of nanoprepreg/nanostitched three dimensional carbon/epoxy multiwall carbon nanotubes composites. Journal of Composite Materials, 2019; 54: 2-19.

[4] Bilişik A, Sapanci E. Plain para-aramid/phenolic multiwall carbon nanotubes prepreg/multistitched preform composites: Experimental characterization of mode-I toughness, Journal of Composite Materials, 2019; 53 (13): 1847-1864. https://doi.org/10.1177/0021998318812176

[5] Eskizeybek V, Avcı A and Gulce A. Preparation and mechanical properties of carbon nanotube grafted glass fabric/epoxy multi-scale composites. Advanced Composite Materials, 2017; 26: 169-180. https://doi.org/10.1080/09243046.2015.1052188

[6] Eskizeybek V, Avcı A and Gulce A. The Mode I interlaminar fracture toughness of chemically carbon nanotube grafted glass fabric/epoxy multi-scale composite structures. Composite Part A, 2014; 63: 94-102. https://doi.org/10.1016/j.compositesa.2014.04.013

[7] Mannov E, Schmutzler H, Chandrasekaran S, Viets C, Buschhorn S, Tölle F, Mülhaupt R, Schulte K. Improvement of compressive strength after impact in fibre reinforced polymer composites by matrix modification with thermally reduced graphene oxide. Composites Science and Technology, 2013; 87: 36-41. https://doi.org/10.1016/j.compscitech.2013.07.019

[8] Gorbatikh L, Verpoest I, Lomov VS, Claes M, Tola C, Siegfried M. Impact and residual after impact properties of carbon fiber/epoxy composites modified with carbon nanotubes, Composites Structures, 2014; 111: 488-496. https://doi.org/10.1016/j.compstruct.2014.01.035

[9] Ye L, Tang Y, Zhang Z, Friedrich K. Interlaminar fracture toughness and CAI strength of fibre-reinforced composites with nanoparticles - A review. Composites Science and Technology, 2013; 86: 26-37. https://doi.org/10.1016/j.compscitech.2013.06.021

[10] Yokozeki T, Iwahori Y, Ishiwata S, Enomoto K. Mechanical properties of CFRP laminates manufactured from unidirectional prepregs using CSCNT-dispersed epoxy. Composite Part A, 2007; 38: 2121-2130. https://doi.org/10.1016/j.compositesa.2007.07.002

[11] Kostopoulos V, Baltopoulos A, Karapappas P, Vavouliotis A, Paipetis A. Impact and after-impact properties of carbon fibre reinforced composites enhanced with multi-wall carbon nanotubes. Composites Science and Technology, 2010; 70: 553-563. https://doi.org/10.1016/j.compscitech.2009.11.023

[12] Sharma SP, Lakkad SC. Impact behavior and fractographic study of carbon nanotubes grafted carbon fiber-reinforced epoxy matrix multi-scale hybrid composites Composite Part A, 2015; 69:124-131. https://doi.org/10.1016/j.compositesa.2014.11.005

[13] Papila M, Bilge K, Ozden-Yenigün. E, Şimşek E, Menceloğlu YZ. Structural composites hybridized with epoxy compatible polymer/MWCNT nanofibrous interlayers Composites Science and Technology, 2012; 72: 1639-1645. https://doi.org/10.1016/j.compscitech.2012.07.005

[14] Sager RJ, Klein PJ, Lagoudas DC, Zhang Q, Liu J, Dai L, Baur JW. Effect of carbon nanotubes on the interfacial shear strength of T650 carbon fiber in an epoxy matrix. Composite Science and Technology, 2009; 69: 898-904. https://doi.org/10.1016/j.compscitech.2008.12.021

[15] Siddiqui NA, Sham ML, Tang BZ, Munir A, Kim JK. Tensile strength of glass fibers with carbon nanotube-epoxy nanocomposite coating. Composite Part A, 2009; 40: 1606 - 1614. https://doi.org/10.1016/j.compositesa.2009.07.005

[16] Warrier A, Godara A, Rochez O, Mezzo L, Luizi F, Gorbatikh L, Lomov SV, Vuure AWV, Verpoest I, The effect of adding carbon nanotubes to glass/epoxy composites in the fibre sizing and/or the matrix. Composites: Part A, 2010; 41: 532-538. https://doi.org/10.1016/j.compositesa.2010.01.001

[17] Godara A, Gorbatikh L, Kalinka G, Warrier A, Rochez, O, Mezzo L, Luizi F, Vuure AWV, Lomov SV, Verpoest I. Interfacial shear strength of a glass fiber/epoxy bonding in composites modified with carbon nanotubes. Composite Science and Technology, 2010; 70: 1346-1352. https://doi.org/10.1016/j.compscitech.2010.04.010

[18] Liu Y, Zhang X, Song C, Zhang Y, Fang Y, Yang B, Wang X. An effective surface modification of carbon fiber for improving the interfacial adhesion of polypropylene composites. Materials and Design, 2015; 88: 810-819. https://doi.org/10.1016/j.matdes.2015.09.100

[19] Demircan O, Darkazali AA, Inanc I, Eskizeybek V. Investigation of the effect of CNTs on the mechanical properties of LPET/glass fiber thermoplastic composites, Journal of Thermoplastic Composite Materials, 2019: 1-22, DOI: 10.1177/0892705719833105. https://doi.org/10.1177/0892705719833105

Research Article

Mechanical and thermal behavior of natural fiber-polymer composites without compatibilizers

Veikko Sajaniemi[a], Alp Karakoç*[,b], Jouni Paltakari[c,]

Aalto University, Department of Bioproducts and Biosystems, P.O. Box 11000, FI-00076 Aalto, Finland

Article Info	Abstract
	The present study aims at understanding the mechanical and thermal properties of natural fibers in a polymer matrix without strong adhesion between the two constitutes. For this purpose, four types of pulps, which are refined and unrefined pine and birch kraft pulps, were used together with polypropylene without any compatibilizer. One constituent pulp based and composite pulp fiber-polypropylene handsheets were prepared by standard laboratory sheet preparation method followed by hot pressing process. In addition to these handsheets, pure polypropylene sheets were also formed as the reference. The produced handsheets were tested to determine their tensile properties following the ISO 1924-2 standard for paper and board. During these tests, infrared thermal imaging was also carried out with FLIR A655SC thermal camera with frame rate of 200 Hz and thermal resolution of 50 mK so as to investigate the thermal behavior. As a result of the experiments, it was deduced that the chosen methods produced composites with unsatisfactory properties. In addition, microstructures of the investigated handsheets were analyzed with scanning electron microscopy (SEM) indicating the heterogeneous mixing of constituents and existence of material defects, which was mainly due to the inherent incompatibility of hydrophilic natural fibers and hydrophobic thermoplastics. The study aims at paving a way for improved natural fiber-polymer composite manufacturing methods, a requirement for better understanding the natural fiber and polymer matrix bonding practices.

1. Introduction

Since the natural fibers are abundant, ecological, economical, light and have high specific mechanical characteristics, they have been widely used as reinforcement in natural fiber-polymer composites with applications in paper and packaging, construction and automotive industries [1, 2]. Thus, biocomposites based on natural fibers and especially thermoplastic polymer blends are being widely investigated to minimize the plastic waste problem [3-5]. The mechanical properties of these composites primarily depend on the elastic behavior and strength of fibers, fiber network, matrix and interfacial bonding [6-10]. Especially, a strong adhesion between the fiber and the matrix is of great importance for the effective load distribution and reinforcement throughout the composite [11-13]. However, in case of natural fiber-polymer composites, fibers are hydrophilic for most of the cases and incompatible with the common hydrophobic thermoplastics, which can limit the proper bonding [14, 15]. Thus, various compatibilizers, such as phosphate titanite, or wood surface modification treatments, like acetylation, are used to bind the constituents together [16-18].

In order to create an in-depth understanding of the bonding limits of natural fibers and thermoplastics, different natural fiber types with and without polymer matrix were investigated. For this purpose, four types of wood fiber; refined and unrefined birch kraft pulp and refined and unrefined pine kraft pulp; were investigated in polypropylene PP matrix without any compatibilizer. Mechanical properties of these composites were evaluated and compared to the papers made of either wood or PP that can be co-polymerized to increase its strength and durability [19]. Thermal camera recordings were also used to understand the thermal characteristics of the investigated materials which were subjected to tensile loading. Therefore, the present study aims at providing an advancement in natural fiber-polymer composite design and manufacturing with findings on the effects of compatibilizers on the physical and mechanical characteristics of final products.

2. Methodology

As listed in Table 1, nine types of laboratory handsheets were formed out of four types of pulps by following the ISO 5269-1:2005 laboratory sheet preparation standard so as to conduct subsequent physical tests [20]. Sheets had a rectangular shape and a side-length of 16.5 cm and a grammage of ~120 g/m². PP melting temperature was measured as 163 °C using hot plate and infrared thermometer in the Aalto University facilities. The measurements were in well alignment with the ones in the literature [21]. Composite handsheets were thereafter prepared adding PP granules to fiber-water suspension before forming process. Some adjustments, the details of which are elaborated below, were needed for these handsheets compared to the standard formation process due to the hydrophobic and light nature of the PP.

Based on the ISO-187:1990 standard atmosphere for conditioning and testing in line with ISO 5269-1:2005 laboratory handsheet preparation standard, the handsheets were kept in a room of 50% relative humidity and at 23°C temperature for minimum 24 hours for conditioning and drying [20, 22]. Thereafter, the handsheets were hot pressed under steady conditions for 2 minutes at 180 °C temperature with 50 kN force with Vakomet KRO-260 press and Siemens Simatic HMI KTP400 controller system. PP sheets of the same size and grammage as paper sheets were prepared by laying 3.267 g of PP granules in a paperboard frame, letting the specimen to melt on the hot press plate and pressing it to shape using 200 kN force and 200 °C temperature.

Retention was determined at 95 % and 94 % with refined birch and pine, respectively. Unrefined pulps were assumed to have 100 % retention due to non-existence of fines. PP retention was determined at 55 %, although it varied a lot due to challenging nature of PP granules in papermaking. PP had virtually no adhesion to fibers in aqueous phase and stuck easily to the walls of the handsheet trough. Also, PP interfered the process of removing fresh fiber mat from wire for drying. Being lighter than water and the fibers, PP granules settled on top of fiber matrix which resulted in very low adhesion of wet composite handsheets with the suction board. Additionally, PP granules detached easily out of the composite handsheets after drying the samples. Composite handsheets with unrefined pulps of low wet strength were especially challenging, the problem that was tackled adding part of the PP granules to dried handsheets just before the hot press. Due to these factors, the PP amount in these sheets varied profoundly.

Table 1. Handsheet materials, identification, their fiber and polymer fractions, physical characteristics

Material	ID	Fiber (mass %)	PP (mass %)	Thickness (μm)	Grammage (g/m^2)
Birch, refined	BR	100	0		
Mean				169	122
Std. dev.				1%	1%
Birch, refined, with PP	BRPP	50	50		
Mean				302	122
Std. dev.				5%	5%
Birch, unrefined	BU	100	0		
Mean				253	126
Std. dev.				2%	2%
Birch, unrefined, with PP	BUPP	50	50		
Mean				279	121
Std. dev.				3%	11%
Pine, refined	PR	100	0		
Mean				190	124
Std. dev.				1%	1%
Pine, refined, with PP	PRPP	50	50		
Mean				244	127
Std. dev.				4%	15%
Pine, unrefined	PU	100	0		
Mean				268	118
Std. dev.				1%	2%
Pine, unrefined, with PP	PUPP	50	50		
Mean				317	127
Std. dev.				8%	2%
Polypropylene	PP	0	100		
Mean				244	127
Std. dev.				4%	15%

Specimens were cut to dog-bone shape with mid-width of 10 mm and span length of 100 mm to determine their tensile properties by following the ISO 1924-2:2008 testing standard for paper and board [23]. Tensile tests were conducted under 50% relative humidity and at 23°C temperature by using MTS 400/M vertical tensile testing system equipped with 200 N load cell. The cross-head speed was fixed to 12 mm/min and the clamp span of 100 mm was used in these measurements. In this setup, displacement and strain readings were recorded via crosshead position while force and stress measurements were obtained through force transducer and the measure cross-sectional areas per specimen. Temperature difference at breakage point was determined using FLIR A655SC

thermal camera with frame rate of 200 Hz, optical resolution of 640 x 480 pixels and thermal resolution of 50 mK. The thermal images of the selected specimens can be found in the Appendix.

3. Results and Discussions

3.1 Tensile properties and thermal characterization

The tensile test results with mean and standard deviations are tabulated in Table 2 while the stress-strain curves are depicted in Figures 1 and 2 following the fiber content for birch and pine. Literature values for the elastic modulus of birch and pine based handsheets are between 1 and 10 GPa depending on the fiber orientation [24, 25]. In these one constituent handsheets, the fibers were randomly oriented and the handsheet elastic moduli obtained for the refined birch BR (4854 MPa) and the refined pine PR (4436 MPa) were well aligned with the previous investigations [26]. This was an expected outcome since the handsheets with one constituent have well established and standard production method. Nevertheless, in case of unrefined pulps, fiber bondings inside the handsheets were deduced to be weak since there was only mechanical and heat treatment for the formation process. Therefore, without the enhanced fiber bonding, interfiber breakage should prevail intrafiber failure, which results in lower elastic moduli as seen in unrefined birch and pine BU and PU, respectively, in Table 2. The same phenomenon explains the differences in tensile index, break strain and absorbed tensile energy. On the other hand, composite handsheets were deduced to have a lot of variation in their mechanical and thermal characteristics. This shows that importance of compatibilizers in composite handsheet formation, for which the bonding should be well built. Based on the present investigations, the compatibilizers are deduced to play a critical role especially in case of hydrophilic and hydrophobic constituents.
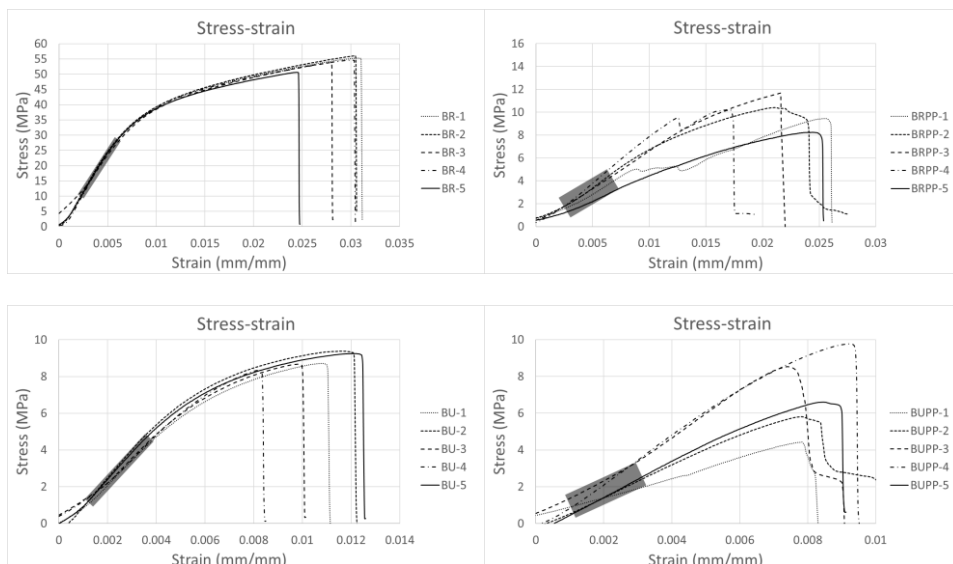

Fig. 1. Stress-strain curves obtained from tensile testing of handsheets from refined BR and unrefined birch BU and their blends with polypropylene PP. Highlighted domains represents the stress-strain ranges for the elastic modulus computations.
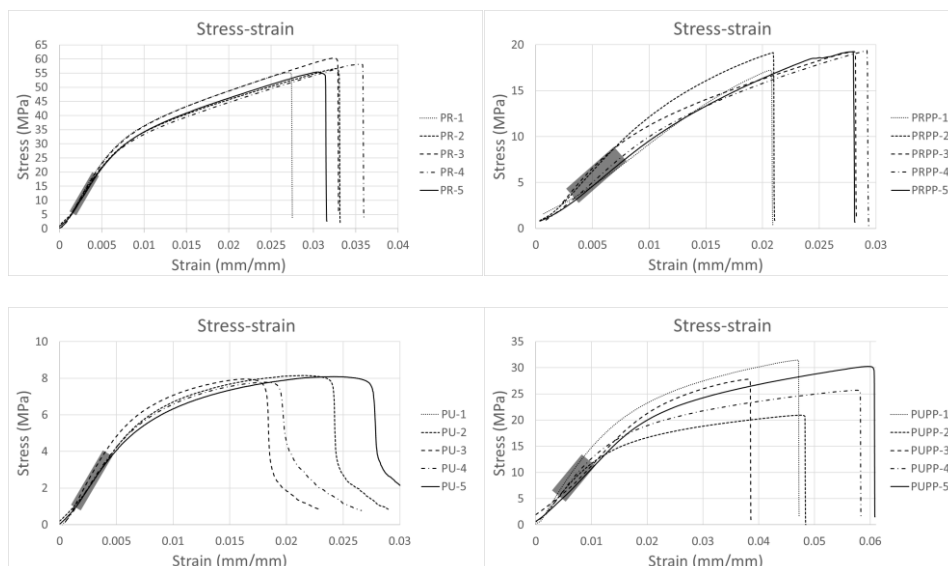
Fig. 2. Stress-strain curves obtained from tensile testing of handsheets from refined PR and unrefined pine PU and their blends with polypropylene PP. Highlighted domains represents the stress-strain ranges for the elastic modulus computations.

It is also observed that the produced composite handsheets did not follow the general rule of mixtures, i.e. neither Voigt model (upper-bound modulus) nor Reuss model (lower-bound modulus). This has been also observed by other researcher working on the natural fiber composites [11] when the fraction of pulp fibers in a PP matrix was over 20 % by mass. For example, refined pulp-polymer composites BRPP and PRPP are significantly weaker than plain fiber or polymer sheets. On the other hand, the unrefined pulps seem to gain strength with the addition of polymer. The strength of these sheets primarily comes from the polymer phase as their grammage and fraction is much higher than those of the other composites due to modifications in the manufacturing method. The scanning electron microscopy (SEM) images in the following section support the postulate.

3.2 Scanning electron microscopy

In order to understand the details of the apparent properties of the handsheets, SEM images were recorded with Hitachi TM1000 tabletop microscope in charge-up reduction mode with acceleration voltage of 15 kV recommended by the manufacturer. In contrast to the conventional sample preparation techniques, samples imaged by the TM-1000 required no special preparation such as metal coatings of non-conductive samples, which was very useful in terms of time and labor efficiency [27]. For the imaging, samples with surface areas of 2 x 2 mm² were cut from the handsheets, the thicknesses of which are same as the ones listed in Table 1. A wide range of magnifications from 100 to 2000 times was utilized to investigate the sample structure and constituents. The images presented in Figures 3-6 indicate the importance of the compatibilizers since the matrix and reinforcement were not mixed well enough to fulfil the reasonable mechanical characteristics. No polymer matrix is visibly present in between the fibers in the side and cross-section images of the refined birch-PP composite as shown in Figure 3. As also stated

previously, this confirms the importance of the compatibilizers to bind matrix and fiber material together in natural fiber polymer composites.

Table 2. Tensile test results of different composite handsheets. Please, refer to Table 1 for the handsheet abbreviations BR, BRPP, BU, BUPP, PR, PRPP, PU, PUPP and PP.

	Elastic modulus (MPa)	Tensile index (kNm/kg)	Break strain (%)	Tensile energy absolute index (J/m²)	dT (°C)
BR					
Mean	4854	75	2.8	1564	2.9
Std. dev.	5.3 %	3.3 %	7.6 %	11 %	33 %
BRPP					
Mean	726	19	2.3	270	1.6
Std. dev.	27 %	21 %	39 %	55 %	74 %
BU					
Mean	1161	18	1.0	117	2.6
Std. dev.	9.8 %	4.3 %	13 %	21 %	9.4 %
BUPP					
Mean	1243	28	1.6	417	2.3
Std. dev.	44 %	63 %	63 %	18 %	41 %
PR					
Mean	4436	87	3.0	1794	9.3
Std. dev.	7.8 %	3.8 %	11 %	15 %	10 %
PRPP					
Mean	1295	44	2.2	597	4.5
Std. dev.	17 %	5.1 %	21 %	26 %	31 %
PU					
Mean	975	18	1.8	243	1.1
Std. dev.	9.7 %	1.4 %	18 %	21 %	18 %
PUPP					
Mean	1258	51	3.6	1415	3.0
Std. dev.	22 %	25 %	47 %	63 %	49 %
PP					
Mean	1400	40	3.2	844	1.7
Std. dev.	23 %	30 %	45 %	55 %	59 %
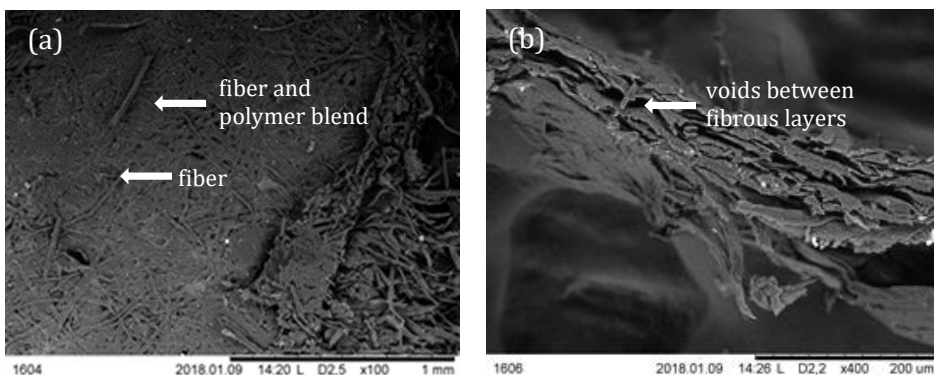
Fig. 3. SEM images of BRPP: (a) bottom side and (b) cross-section.

The layered structure is even more evident with top and bottom images of BUPP depicted in Figure 4. Considering the increasing porous structure of unrefined pulp compared to refined one, it is very unlikely that any melted polymer could have penetrated the fiber network in the heat press for any of the investigated birch samples.
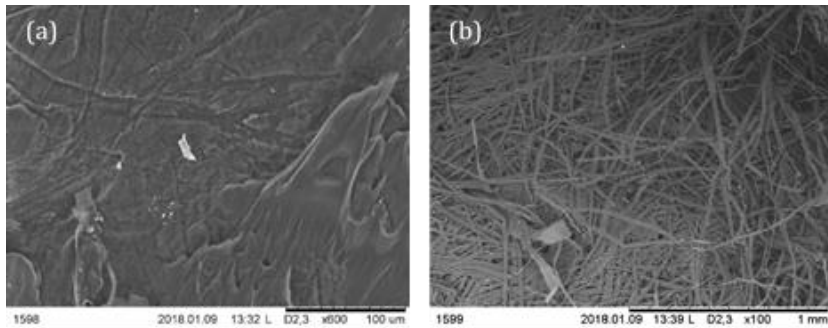

Fig. 4. SEM images of BUPP, (a) top side and (b) bottom side

Figures 5(a) and (b) show the layered structure of PRPP with a partially peeled off polymer coating on top of the fiber network. Through the thin polymer layer, the fiber network underneath is somewhat visible. The polymer layer contains pores in the magnitude of several tens of microns wide. These could be due to escaping water from the hydrophilic fibers during the hot pressing, though the sheets were thoroughly dried before the pressing. In addition to these, the cracks in Figures 5 (c) and (d) also indicate the brittle nature of polymer matrix resulting in poor and unstable mechanical properties.
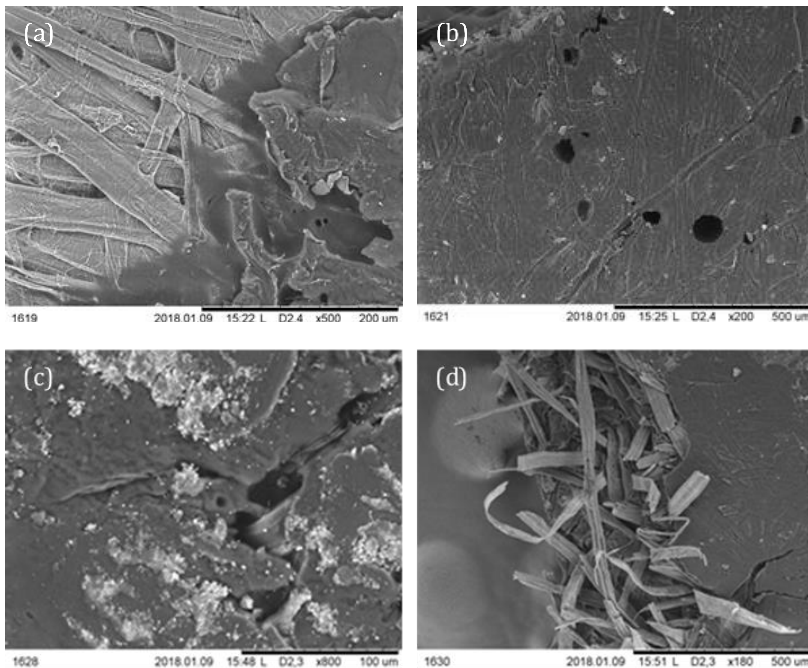
Fig. 5. SEM images of PRPP and PUPP, (a) PRPP image showing a peeled off layer of PP, (b) PRPP image showing pores in the matrix, (c) PUPP top side image, (d) PUPP cutting zone image

Further study of the SEM images in Figure 6 shows uneven distribution of polymer structure within all the composite and plain polymer sheets. This shows the importance of standardization and urge for the development in the manufacturing method.
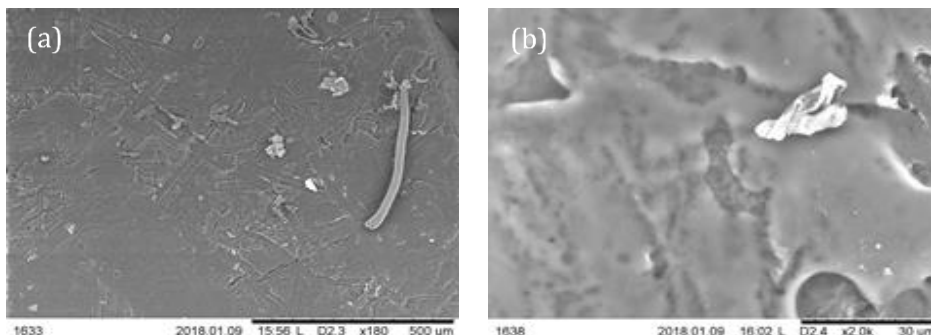
Fig. 6. SEM images of PP, with (a) 180x and (b) 2000x magnification

4. Conclusion

The present study was conducted to understand the effect of inherent incompatibility of hydrophilic natural fibers and hydrophobic thermoplastics on the mechanical and thermal behavior of their composites. Both the mechanical and thermal measurements exhibited a lot of variation and the chosen manufacturing method was deduced to produce unsatisfactory properties due to weak bonding between the constituents and existence of material defects such as pores, which can be clearly seen in the captured SEM images. This shows the necessity of compatibilizer use, which provides the retention and uniform mixing in case of constituent incompatibility.

Since the hot-pressing process was the mere option for the composite handsheet formation without damaging the fibers in the present facilities, another major challenge was the melting behavior of the PP during the process to get an interconnected and even matrix between the fibers. The hot pressing with the used parameters was not able to fulfil this task and fiber network was deduced to be dense for a uniform PP flow through. As seen in Figure 7(a), warping effect was experienced with most of the composite handsheets after hot pressing, which was an evidence of the nonuniform PP flow over the layered structure. When cutting the samples, the sheets had to be straightened as depicted in Figure 7(b), which caused residual strains as the aftermath.
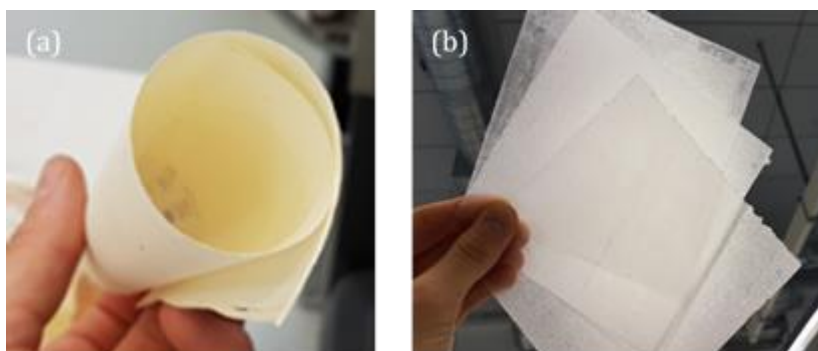

Fig. 7. Composite handsheets: (a) warping after hot pressing and conditioning to standard air moisture, and (b) handsheets to be used for test specimens
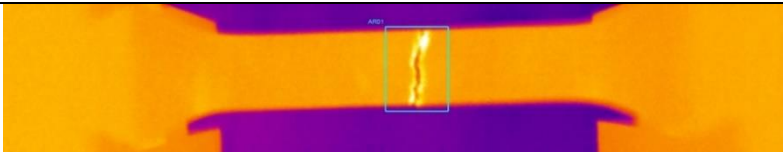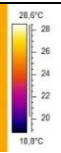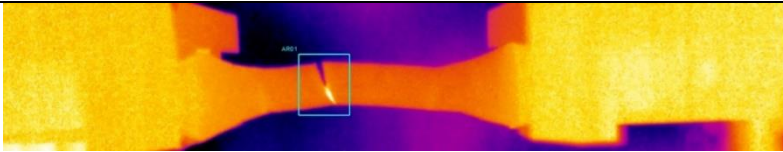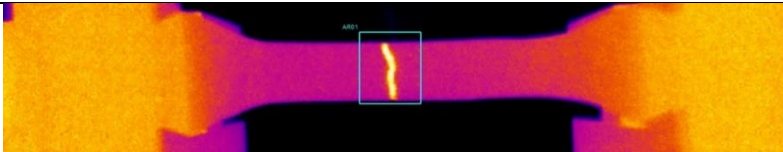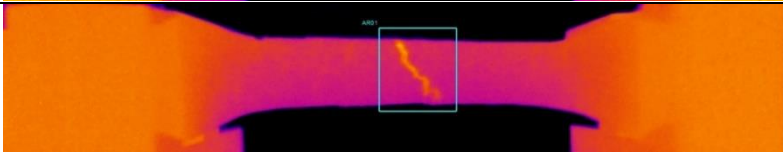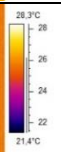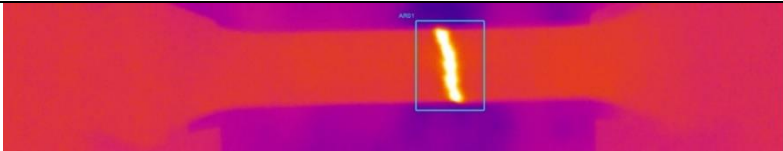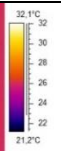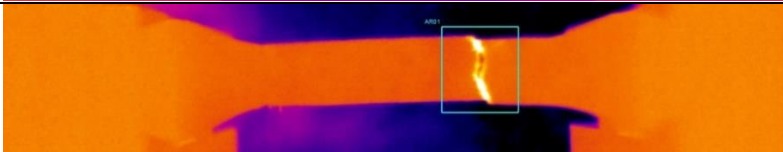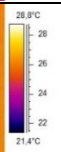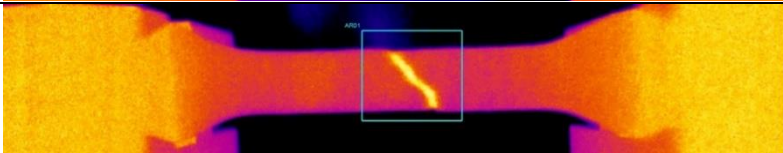
All these manufacturing-based defects and constituent incompatibility were detrimental and resulted in low mechanical characteristics with high variations. Therefore, use of ply structure with low grammage and thin layers of fiber network with polymer stacked on top of each other in multiple layers could be a potential solution to this issue. In addition, increase in the pressure and process time would be also beneficial. Alternatives to hot pressing could also be considered, as long as the other methods do not damage the fibers. As a summary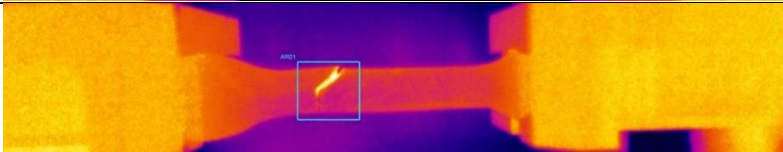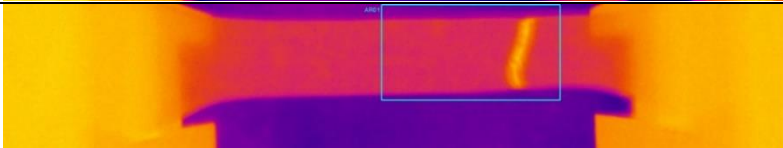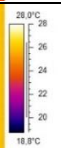, the present study, which investigated the interactions between the reinforcement and the matrix without a compatibilizer, paved a way for improved natural fiber polymer composite manufacturing methods.

References

[1] Iorga L, Pan Y, Pelegri A. Numerical characterization of material elastic properties for random fiber composites. Mech Mater Struct 2008;3(7):1279–98. https://doi.org/10.2140/jomms.2008.3.1279

[2] Russell S. Handbook of nonwovens. Boca Raton, Florida, USA: The Textile Institute: Woodhead Publishing, CRC Press; 2007.

[3] Eszer NH, Ishak ZAM. Effect of compatibilizer on morphological, thermal and mechanical properties of Starch-Grafted-Polypropylene/Kenaf fibers composites. Materials Science and Engineering 2018; 368: 012017. https://doi.org/10.1088/1757-899X/368/1/012017

[4] Özkan M, Karakoç A, Borghei M, Wiklund J, Rojas OJ, Paltakari J. Machine Learning assisted design of tailor-made nanocellulose films: A combination of experimental and computational studies. Polymer Composites 2019. https://doi.org/10.1002/pc.25262

[5] Özkan M, Borghei M, Karakoç A, Rojas O, Paltakari J. Films based on crosslinked TEMPO-oxidized cellulose and predictive analysis via machine learning. Nature Scientific Reports 2018; 8 (4748): 1-9. https://doi.org/10.1038/s41598-018-23114-x

[6] Karakoç A. A fiber network model to understand the effects of fiber length and height on the deformation of fibrous materials. Research on Engineering Structures and Materials, 2016; 2(2): 51-57. https://doi.org/10.17515/resm2015.17ma0825

[7] Karakoç A, Hiltunen E, Paltakari J. Geometrical and spatial effects on fiber network connectivity. Composite Structures, 2017; 168: 335-344. https://doi.org/10.1016/j.compstruct.2017.02.062

[8] Lavrykov S, Lindström S, Singh K, Ramarao B. 3D network simulations of paper structure. Nordic Pulp Paper Research Journal 2012; 27(2): 256-263. https://doi.org/10.3183/npprj-2012-27-02-p256-263

[9] Sampson W. Modelling stochastic fibrous materials with Mathematica, London Springer-Verlag, 2009, ISBN: 978-1-84996-811-9.

[10] Targhagh M, Simulation of the mechanical behaviour of low density paper and an individual inter-fiber bond, MSc. Thesis, University of British Columbia, 2016.

[11] Poletto M, Zattera A. Mechanical and dynamic mechanical properties of polystyrene composites reinforced with cellulose fibers: coupling agent effect. Journal of Thermoplastic Composite Materials 2017; 30(9): 1242-1254. https://doi.org/10.1177/0892705715619967

[12] Yu L, Dean K, Li L. Polymer blends and composites from renewable resources. Prog. Polym. Sci. 2006; 31: 576-602. https://doi.org/10.1016/j.progpolymsci.2006.03.002

[13] Mydul MA, Ahmed T, Haque MM, Gafur MA, Kabir H. Mechanical properties of natural fibre containing polymer composites. Polym. Plast. Technol. 2009; 48: 10113.

[14] George J, Sreekala MS, Thomas S. A review on interfacial modification and characterization of natural fiber reinforced plastic composites. Polym. Eng. Sci. 2001; 41: 1471-1485. https://doi.org/10.1002/pen.10846

[15] Pracella M, Minhaz-Ul Haque Md, Alvarez V. Functionalization, Compatibilization and Properties of Polyolefin Composites with Natural Fibres. Polymers 2010; 2(4): 554-574. https://doi.org/10.3390/polym2040554

[16] Bledzki A, Gassan J, Theis S. Wood-filled thermoplastic composites. Mechanics of composite materials 1998; 34(6): 563-568. https://doi.org/10.1007/BF02254666

[17] Bledzki A, Gassan J. Composites reinforced with cellulose based fibers. Progress in Polymer Science 1999; 24(2): 221-274. https://doi.org/10.1016/S0079-6700(98)00018-5

[18] Saheb D, Jog J. Natural fiber polymer composites: a review. Advances in Polymer Technology 1999; 18(4): 351-363. https://doi.org/10.1002/(SICI)1098-2329(199924)18:4<351::AID-ADV6>3.0.CO;2-X

[19] Whiteley KS, Heggs GT, Koch H, Mawer RL, Immel W. Polyolefins. Ullmann's Encyclopedia of Industrial Chemistry. Weinheim: Wiley-VCH.

[20] Pulps -- Preparation of laboratory sheets for physical testing -- Part 1: Conventional sheet-former method. ISO 5269-1:2005. Geneva, Switzerland: ISO.

[21] Maier C, Calafut, T. Polypropylene: The Definitive User's Guide and Databook. Elsevier Science 2013, ISBN: 978-1-884207-58-7.

[22] Paper, board and pulps -- Standard atmosphere for conditioning and testing and procedure for monitoring the atmosphere and conditioning of samples. ISO-187:1990. Geneva, Switzerland: ISO.

[23] Paper and board -- Determination of tensile properties -- Part 2: Constant rate of elongation method. ISO 1924-2:2008. Geneva, Switzerland: ISO.

[24] Karakoç A, Tukiainen P, Freund J, Hughes M. Experiments on the effective compliance in the radial–tangential plane of Norway spruce. Composite Structures 2013; 102: 287-293. https://doi.org/10.1016/j.compstruct.2013.03.013

[25] Gibson L. The hierarchical structure and mechanics of plant materials. Journal of the Royal Society, Interface 2012; 76(9): 2749-2766. https://doi.org/10.1098/rsif.2012.0341

[26] Berglund L, Carlsson L, Coffin D. Mechanics of Paper Products. Berlin, Boston DeGruyter, 2011, ISBN: 978-3-11-025463-1.

[27] Hitachi TM-1000 Tabletop Microscope Manual, http://www.marinereef.com/pdfs/tm-1000.pdf. Accessed 24 July 2019.

Appendix

ID	Thermal Image (camera: FLIR A655SC)
BR	
BRPP	
BU	
BUPP	
PR	
PRPP	
PU	
PUPP	
PP	

Research Article

Effects of ultra-high frequency induction system on the carbon fiber reinforced thermoplastic composites

Uğur Çavdar[*1, a], Oner Haşim Olgun[2,b]

[1] Mechanical Engineering Department, Engineering Faculty, İzmir Demokrasi University, İzmir/Turkey
[2] Department of Mechanical Engineering, Engineering Faculty, Celal Bayar University, Manisa, Turkey

Article Info	Abstract
	Because of their exceptional features, advanced composites with polymer matrix attract increasing interest in engineering applications recently. Compared to their weight ratio due to the high endurance and hardness values applications of polymer matrixed composites of lightweight, low density, and high performance are popular in military and civil aerospace, automotive, wind power and many other industries. Nowadays, induction heating of the carbon fiber reinforced thermoplastic composites is one of the most important worldwide studies. Due to the importance of accelerating the rate of production from approximately 180-240 minutes to a few minutes, in this study, the weldability of the carbon fiber reinforced thermoplastic composites was investigated. © 2019 MIM Research Group. All rights reserved.

1. Introduction

Thermoplastics are composed of linear molecule rings which are tied to each other with weak Van der Waals bonds. Thermoplastic materials soften over a critical glass transition temperature and viscosity decreases as the temperature raises. These materials become solid again when they are cooled. As an advantage, they can be stored in a solid state in room temperature. Thermoplastics have high rigidity and impact strength. Thermoplastic resins are preferred to increase the tensile and bending strength of the materials. [1]

Carbon fibers are reinforcing materials with the highest specific modulus and specific strength. [2] Combined with epoxy matrixes carbon fibers exhibit extraordinary strength and rigidity. They are not affected by humidity and their frictional resistance is very high. Their wear resistance and fatigue strength are quite good. Because of these properties, they are widely preferred in military and civil airframes. Having expensive production methods, they are used in high valued applications of the aircraft industry, sports equipment or medical equipment.

The reasons of the interest on carbon fiber reinforced thermoplastic composites are the production processes advantages as short autoclave times, low storage costs and ability to be thermoformed again alongside of their mechanic properties as good impact behavior, damage tolerance, high-temperature resistance, etc. [3-7]

Although it is generally mentioned with metals because of their electrical and magnetic properties, effects of induction heating on polymer materials and composites are also has been examined in the last decade. [8-20]

Welding of polymer composites to polymer composites is characterized by heating the components over melting temperature, combining them and cooling under pressure.

Induction heating is based on the effects of induced eddy currents and magnetic polarisation. When an alternative voltage is applied to a conductive coil an alternative current is generated. When a magnetically susceptible and electrically conductive material gets close to the coil's magnetic field, eddy currents are induced. Eddy currents encounter with the material's resistance and energy is lost by transforming into heat form. [21]

In welding of thermoplastics, a metal mesh between the contact interface or carbon fiber fabric is used along with other methods, but because this study is about induction welding we just focused on it. Other induction welding parameters are generator power, weld time, pressure and cooling time. [22]

In the first phase of this study, induction welding capability of 4 different compositions of carbon fiber reinforced thermoplastic composites is examined. It is observed from the experiments that cross-ply stacks (0°/90°) plates or unidirectional (UD) stacks plates of which fibers of interfaces are perpendicular to each other can be welded by ultra-high frequency induction system while UD stacks plates with fibers on the interfaces are in the same direction cannot. In the second phase, how the induction coil is heating the carbon fiber reinforced thermoplastic materials and the heating gradient on the surface and across cross-sectional area were observed.

2. Materials and Methods

In this study, carbon fiber reinforced thermoplastic (poly ether ether ketone - PEEK) composite plates, which have 56% carbon fiber ratio in weight, are used. In the first phase, the plates are produced by hot press method and have 14 plies with each ply thickness of 142 μm of prepregs. These are domestically produced by Mir Unique Solutions Inc. The features of the samples are in Table 1. The plates are 20 mm in width, 20 mm in length and 2 mm in thickness. Two of the plates with the same composition are oriented on top of each other and pressed under a standard 1,2 MPa pressure during the welding.

A 2.8kW and 900 kHz ultra-high frequency induction system is used in atmospheric conditions. The cylindrical single turn induction coil has 2 mm diameter as shown in Figure 1. The coupling distance is 4 mm. The weld times and temperatures are given in Table 2.

The temperatures of the composites were measured with an infrared pyrometer (± 5 °C) during the process. At the end of the heating process, the samples were left to cool naturally to room temperature.

In the second phase, the plates are produced in autoclave up to 385°C temperature under an increasing pressure process up to 0,8 Mpa. These too are domestically produced by Mir Unique Solutions Inc. The orientations of the carbon fibers are unidirectional, cross-ply stacks (0°/90°) and 5 satin harness (HS) plates. The plates made of multiplies are 20 mm in width, 40 mm in length and 2 mm in thickness except for the 5 satin harness plies plates due to having 16 plies where the others have 14. Single plies of the compositions are also tested where cross-ply stacks and 5 satin harness orientations have 2 plies naturally.

Table 1. The features of the samples

Sample no.	Description of sample	Contents of sample	The production method of sample
S1	Two (0°/90°) cross-ply stack plates	PEEK matrice and carbon fiber	Hot (400°C) pressed for 15 mins and cold pressed for 15 mins under 5 MPa
S2	Two (0°/90°) cross-ply stack plates	PEEK matrice and carbon fiber	Hot (400°C) pressed for 15 mins and cold pressed for 15 mins under 5 MPa
S3	Two (0°) unidirectional (UD) plates on a hot plate	PEEK matrice and carbon fiber	Hot (400°C) pressed for 15 mins and cold pressed for 15 mins under 5 MPa
S4	Two (0°) UD plates	PEEK matrice and carbon fiber	Hot (400°C) pressed for 15 mins and cold pressed for 15 mins under 5 MPa
S5	Two (0°/90°) cross-ply stack plates	PEEK matrice and carbon fiber	Hot (400°C) pressed for 15 mins and cold pressed for 15 mins under 5 MPa
S6	Two (0°/90°) cross-ply stack plates	PEEK matrice and carbon fiber	Hot (400°C) pressed for 15 mins and cold pressed for 15 mins under 5 MPa
S7	Two (0°) UD plates, the fiber directions are perpendicular in the contact interface	PEEK matrice and carbon fiber	Hot (400°C) pressed for 15 mins and cold pressed for 15 mins under 5 MPa
S8	Two (0°) UD plates, the fiber directions are perpendicular in the contact interface	PEEK matrice and carbon fiber	Hot (400°C) pressed for 15 mins and cold pressed for 15 mins under 5 MPa
S9	Two (0°) UD plates	PEEK matrice and carbon fiber	Hot (400°C) pressed for 15 mins and cold pressed for 15 mins under 5 MPa

Due to the melting temperature of PEEK matrice (343°C) [23], the samples were heated in 350, 400, and 450°C for 2 minutes. During the heating process, the temperature of the samples' reverse sides was measured by another infrared thermometer on the projection of the coil.

Table 2. Welding parameters of samples

Sample no.	Welding temperature (°C)	Welding dwell time (minute)
S1	280	5
S2	310	3
S3	400	5
S4	310	5
S5	280	3
S6	310	5
S7	400	3
S8	310	3
S9	280	5

Fig. 1 The cylindrical single turn induction coil.

3. Result and Discussion

The weldability results for carbon fiber reinforced thermoplastic composites are presented in Table 3.

Empirical values are applied in weld times because when the heating generation will be uniform in the cross-sectional area cannot be assessed in this phase of the study due to the lack of thermal camera. The pictures of all of the samples in the study are shown in Figure 2.

The samples in Figure 2 are welded because the orientation of the plies of carbon fibers are perpendicular to each other that eddy currents were induced in closed loops. These eddy currents caused to heat generation.

In the rest of the samples, welding didn't occur because of the unidirectional orientation of carbon fibers to each other. Although hot plate was used under S3, heat generation was not enough to exceed the melting temperature that weld didn't happen due to the too long coupling distance with the hot plate. When the coupling distance is arranged in the field of the coil it is assessed that hot plate will be useful to weld. In some of these samples, variable

regions have delamination's or deformations are observed. Because the defining of parameters is not studied in this phase, especially with interfaces they are not examined.

Table 3. The weldability results

Sample no	Welding orientation	Result (*Because of calcification problems of the material, results are checked by eyesight only.*)
S1	Two (0°/90°) cross-ply stack plates	Welded
S2	Two (0°/90°) cross-ply stack plates	Welded
S3	Two (0°) unidirectional (UD) plates on a hot plate	In line with the theory, eddy current could not be generated and although hot plate was used heat generation and welding did not happen.
S4	Two (0°) UD plates	In line with the theory, eddy current could not be generated, thus heating and welding did not happen.
S5	Two (0°/90°) cross-ply stack plates	Welded
S6	Two (0°/90°) cross-ply stack plates	Welded
S7	Two (0°) UD plates, the fiber directions are perpendicular in the contact interface	Welded
S8	Two (0°) UD plates, the fiber directions are perpendicular in the contact interface	Welded
S9	Two (0°) UD plates	In line with the theory, eddy current could not be generated, thus heating and welding did not happen.

In the second phase, 35 samples are used but because the IR thermometer is not precise and the single turn coil couldn't generate a uniform heat distribution, correct and precise measurements couldn't be done. So the results were not satisfactory and are not given here.

In order to achieve more uniform heating pattern, a new coil design is needed. Thus a new coil was designed as in Figure 3. The new coil has 3 mm in diameter due to the restrictions of the sample dimensions and the design.

The coupling distance was arranged as 3 mm at the beginning but desired heating values were not achieved because of not enough power of the generator that it was decreased to 2 mm. The reason for this is assessed as the new coil has a thicker (3 mm) diameter and the induction system is designed for a coil with 2 mm diameter. So the power of the system was not enough for the new coil.

The setting point of the pyrometer is shown in Figure 4. The temperatures below the samples were measured on two points. These two points are as in Figure 5.

In the first four samples, it is seen that measured values of single 5 HS stack plates are very close to the set temperatures by the pyrometer.
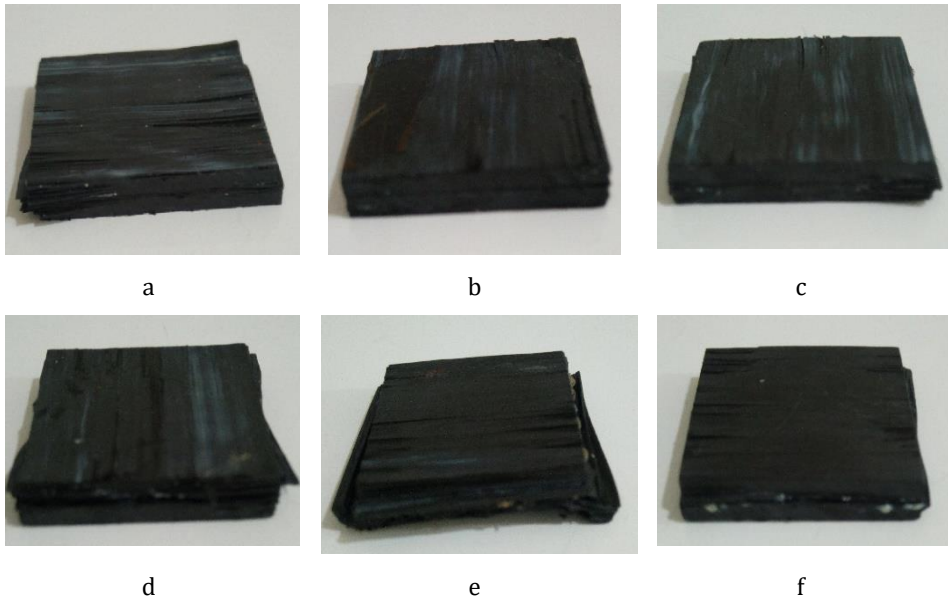
Fig. 2. The pictures of the induction welded samples: a) S1, b) S2, c) S5, d) S6, e) S7, f) S8

In 5 and 6th samples, 8 5 HS woven plies stack plates' measured temperatures, especially of the 1st temperature point, are significantly low. Although it is assessed that the reason is the increasing coupling distance by the thickness of the plates, 7 and 8th samples do not support the assessment. This situation might be a subject of further studies with more precise measurement equipment and more samples.

Fig. 3 The new coil design

Fig. 4 Setting point of the pyrometer.

In the 9, 10, 11 and 12th samples, measured temperatures of cross-ply stack (0/90) of 14 plies decrease slightly due to the explanation of 5 and 6th samples.

As a result of the study, it is observed that setting the pyrometer at 350°C does not provide exceeding the melting temperature of PEEK matrices of the samples and it is not a good parameter. Thus, 400°C will be used in successive studies.
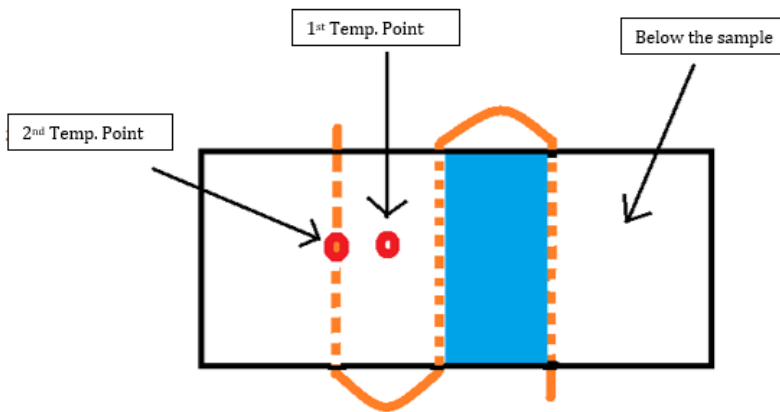

Fig. 5 The measurement points by IR thermometer.

Table 4. Heating gradient results.

Sample no	Set Temp. (°C)	1st and 2nd Temp. Point by IR Thermometer (°C)	Sample Architecture
1	400	365-400	Single 5 HS stack
2	400	345-400	Single 5 HS stack
3	350	310-325	Single 5 HS stack
4	350	310-345	Single 5 HS stack
5	400	310-330	8 5 HS woven plies stack
6	400	315-330	8 5 HS woven plies stack
7	350	295-345	8 5 HS woven plies stack
8	350	320-350	8 5 HS woven plies stack
9	400	355-375	Cross ply stack (0/90) of 14 plies
10	400	295-345	Cross ply stack (0/90) of 14 plies
11	350	330-345	Cross ply stack (0/90) of 14 plies
12	350	310-320	Cross ply stack (0/90) of 14 plies

4. Conclusion

In line with the theory, welding has occurred in the samples 1, 2, 5, 6, 7 and 8 while in the samples 4 and 9, due to no eddy current generation in (0°) UD plates heating and welding didn't happen in contact interfaces. In sample 3, to overcome the mentioned problem, the hot plate was placed under the plates but the heat generated in the interface didn't reach the melting temperature that welding didn't happen.

Defining the parameters will be the subject of future phases of the study. In the second phase, the architecture and orientations of the plates were considered and heating gradients of (0°) UD, (0°/90°) cross-ply stacks and 5 satin harness plates with single and multiplies were revealed. According to the conclusions of the study; the thermoplastic composites with % 56 wt. carbon fiber reinforcement were heated successfully due to the response of carbon fibers to induction currents.

Acknowledgments

References

[1] Aran A. Elyaf takviyeli karma malzemeler, İTÜ: İstanbul, Turkey 1990: 8-9.

[2] Callister WDJr, Rethwisch DG. Malzeme Bilimi ve Mühendisliği, 8th ed.; Wiley: New York, 2011: 648-650.

[3] Vieille B, Chabchoub, M. Bouscarrat, D., Gautrelet, C. A fracture mechanics approach using Acoustic Emission Technique to investigate damage evolution in woven-ply thermoplastic structures at temperatures higher than glass transition temperature, Composites Part B. 2016; 116: 340-351. https://doi.org/10.1016/j.compositesb.2016.10.074

[4] Vieille B, Casado VM, Bouvet C. About the impact behavior of woven-ply carbon fiber-reinforced thermoplastic - and thermosetting - composites: a comparative study, Compos Struct. 2013; 101: 9-21. https://doi.org/10.1016/j.compstruct.2013.01.025

[5] Vieille B, Casado VM, Bouvet C. Influence of matrix toughness and ductility on the compression after-impact behavior of woven-ply thermoplastic- and thermosetting composites: a comparative study, Compos Struct. 2014; 110: 207-218. https://doi.org/10.1016/j.compstruct.2013.12.008

[6] Vieille B, Aucher J, Taleb L. About the influence of temperature and matrix ductility on the behaviour of carbon woven-ply PPS or epoxy laminates: notched and unnotched laminates, Comp Sc Tech. 2011; 71: 998-1007. https://doi.org/10.1016/j.compscitech.2011.03.006

[7] Vieille B, Albouy W. Fatigue damage accumulation in notched woven-ply thermoplastic and thermoset laminates at high-temperature: influence of matrix ductility and fatigue life prediction, Int. J. Fatigue. 2015; 80: 1-9. https://doi.org/10.1016/j.ijfatigue.2015.04.019

[8] Bayerl T, Duhovic M, Mitschang P, Bhattacharyya D. The heating of polymer composites by electromagnetic induction - A review, Composites: Part A. 2014, 57: 27-40. https://doi.org/10.1016/j.compositesa.2013.10.024

[9] Bensaid S, Trichet D, Fouladgar J. 3-D simulation of induction heating of anisotropic composite materials, IEEE Trans. Magn. 2005; 41(5): 1568-1571. https://doi.org/10.1109/TMAG.2005.845047

[10] Bensaid S, Trichet, D, Fouladgar J. Electromagnetic and thermal behaviours of multilayer anisotropic composite materials, IEEE Trans. Magn. 2006; 42(4): 995-998. https://doi.org/10.1109/TMAG.2006.870926

[11] Menana H, Féliachi M. 3-D eddy current computation in carbon-fibre reinforced composites, IEEE Trans. Magn. 2009; 45(3): 1008-1011. https://doi.org/10.1109/TMAG.2009.2012542

[12] Ramdane B, Trichet D, Belkadi M, Saidi T, Fouladgar J. Electromagnetic and thermal modelling of composite materials using multilayer shell elements, IEEE Trans. Magn. 2011; 72(5): 1134-1137. https://doi.org/10.1109/TMAG.2010.2075918

[13] Wasselynck G, Trichet D, Ramdane B, Fouladgar J. Microscopic and macroscopic electromagnetic and thermal modelling of carbon fibre reinforced polymer composites, IEEE Trans. Magn. 2011; 47(5): 1114-1117. https://doi.org/10.1109/TMAG.2010.2073456

[14] Chen SC, Jong WR, Chang JA. Dynamic mould surface temperature control using induction heating and its effect on the surface appearance of weld line, J. Appl. Polym. Sci. 2006; 101: 1174-1180. https://doi.org/10.1002/app.24070

[15] Kim S, Shia CS, Kim BH, Yao D. Injection moulding nanoscale features with the aid of induction heating, Polym. Plast. Technol. Eng. 2007; 46: 1031-1037. https://doi.org/10.1080/03602550701522344

[16] Tanaka K, Katsura T, Kinoshita Y, Katayama T. Mechanical properties of jute fabric reinforced thermoplastic moulded by high-speed processing using electromagnetic

induction, High Perform. WIT Trans. Built Environ. 2008; 97: 211-219. https://doi.org/10.2495/HPSM080231

[17] Border J, Salas R. Induction heated joining of thermoplastic composites without metal susceptors, Proceedings of the 34th international SAMPE symposium, 1989; 2569-2578.

[18] Stokes VK. Experiments on the induction welding of thermoplastics, Polym.Eng.Sci. 2003; 43(9): 1523-1541. https://doi.org/10.1002/pen.10129

[19] Kagan VA, Nichols RJ. Benefits of induction welding of reinforced thermoplastics in high performance applications, J. Reinf. Plast. Compos. 2005; 24(13): 1345-1352. https://doi.org/10.1177/0731684405048846

[20] Knauf BJ, Webb DP. Liu C, Conway PP. Polymer bonding by induction heating for microfluidic applications, Proceedings of the 3rd IEEE international conference on electronics systems and integration technologies (ESTC), 2010. https://doi.org/10.1109/ESTC.2010.5642834

[21] Ahmed TJ, Stavroc D, Bersee HEN, Beukers A. Induction welding of thermoplastic composites - An overview. Composites: Part A. 2006; 37: 1638-1651. https://doi.org/10.1016/j.compositesa.2005.10.009

[22] Rudolf R, Mitschang P, Neitzel M. Induction heating of continuous carbon-fibre-reinforced thermoplastics. Composites: Part A. 2000; 31: 1191-1202. https://doi.org/10.1016/S1359-835X(00)00094-4

[23] Liang B, Hamila N, Peillon M, Boisse P. Analysis of thermoplastic prepreg bending stiffness during manufacturing and of its influence on wrinkling simulations. Composites: Part A. 2014; 67: 111-122. https://doi.org/10.1016/j.compositesa.2014.08.02

Research Article

Investigating the effect of silica aerogel content on the mechanical properties of epoxy resin system

Hasan Yavuz Ünal[1,a], Selay Sert Çok[2,b], Fatoş Koç[2,c], Nilay Gizli[2,d], Yeliz Pekbey[*1,e]

[1]*Department of Mechanical Engineering, Ege University, Izmir, Turkey*
[2] *Department of Chemical Engineering, Ege University, Izmir, Turkey*

Article Info	Abstract
	Nowadays, silica aerogels have been widely used in many applications due to their extremely low density, low thermal conductivity and high specific surface area. Many researchers have proved that the addition of the nanoparticles into thermoset polymers resin has influenced the mechanical properties of the composites. Epoxy resins are one of the mostly used thermoset polymers. Although they have superior mechanical strength, they are usually suffered from their fragile structure. There are several additives such as carbon nanotubes, nanoclay, calcite etc. that can be added to epoxy resins to enhance their mechanical properties such as tensile strength, modulus of elasticity, break strain. In this study, the silica aerogels were added as nano-fillers into epoxy to investigate the effect of the silica aerogel content on the mechanical performance of silica aerogel–epoxy composites. Two different silica aerogel–epoxy composites were produced with various silica aerogel content (0.5 and 1 wt. %) and effect of aerogel amount on the mechanical and structural properties of final nanocomposites was investigated. Silica aerogels used in the study were synthesized by traditional sol gel method to obtain versatile silica aerogel–epoxy composites. Apart from the classically synthesized silica aerogels, aerogels in the present study contain short chained ionic liquid (IL) as porogenic agents. The effect of the addition of the silica aerogel on the tensile and flexural properties of final composites were observed by the measurement of the tension and three-point bending tests, respectively according to ASTM standard. The results have shown that the mechanical behavior of the epoxy resin was significantly influenced by the silica aerogel addition. The mechanical strength of epoxy composite with silica aerogel addition was improved compared to that of the neat epoxy.

1. Introduction

Silica aerogels are extraordinary porous materials with numerous superior properties such as very low density (0.003-0.5 g/cm^3), high surface area (500-1200 m^2/g), and high porosity (80%-99.8%) [1-4]. Due to their outstanding properties aerogels are frequently used in many applications as thermal insulators [5], catalysis, chemical sensors [6], in drug delivery systems [7], acoustic insulators [8] and in space applications [9]. Due to their highly developed 3D porous structure, aerogels are also used as nano-fillers in several composites production, recently. Many researchers have showed that the addition of

nanoparticles such as silica aerogels to polymers can improve mechanical, thermal, and electrical properties of epoxy in comparison with the neat composites [10, 11]. Li et.al [2] have investigated the mechanical performance and the thermal conductivity of aramid fibers reinforced with silica aerogels. They concluded that inorganic fibers reinforced with silica aerogels can improve the compressive strength and flexural strength. There are also large amount of studies considering the improvement of mechanical, thermal, and electrical properties of epoxy resins [12,13].

In the recent studies, silica aerogels have become a promising candidate as nano-fillers in many composite productions. Maghsoudi and Motahari, in their study, have focused on the mechanical, thermal, and hydrophobic properties of silica aerogel–epoxy composites. They measured the thermal conductivity and thermal stability of the nanocomposites with different silica aerogel contents. They have deduced that mechanical, thermal, and hydrophobic properties of silica aerogel–epoxy composites were enhanced by increasing the nanoparticle content [14]. Lei et al. have studied the thermal insulation performance and mechanical properties of silica aerogel monoliths by mixing graphene oxide. They measured the compressive modulus and the thermal conductivity of pure aerogel and composite aerogels. The results have showed that the thermal insulation property and compressive strength of silica aerogels were enhanced with the addition of graphene oxide in the silica matrix [15]. In another study, Li et al. investigated mechanical, thermal and flammability properties of glass fiber film/silica aerogel composites. These researchers showed that the elasticity and flexibility of the composites were found to be better than those of the silica aerogel, and could withstand large amounts of compressive strain without failure or cracking [16]. Zhou et al. have investigated mechanical performance and thermal stability of glass fiber reinforced silica aerogel composites based on co-precursor method by freeze-drying. They concluded that the silica aerogel composites showed remarkable mechanical strength and flexibility, which could endure large compressive and flexural strain without structural destroyed [17]. Salimian et al., in another study, proved that addition of small amount of silica aerogels into epoxy resin significantly increased the tensile strength, modulus of elasticity, toughness and glass transition temperature [18]. Due to sufficient pore size of silica aerogels, epoxy resin and silica aerogels are easily consociated. Besides that, mesopores in silica aerogels filled with epoxy according to dead pore ratio. Shafi et al. have used silica gel as a binder or filler in silica aerogel-glass fiber composites. Silica gels filled the gap or channel between glass fiber and silica aerogel. In this manner, thermal conductivity has decreased without make concessions in compression strength. They also conclude that higher than 5 % silica gel addition increase the thermal conductivity [19]. Zhao et al. have investigated effects of precursor and catalyst contents on microstructural, mechanical, hydrophobicity and thermal conductivity [20]. EtOH/MTES (E) and $NH_4OH/MTES$ (N) contained aerogels with different ratios of were synthesized by sol gel method. Young modulus and contact angle increased with lower (E). Additionally, linear shrinkage decreased with higher (N) ratio. Thermal stability of aerogel was measured around 350 ºC and maximum contact angle was obtained as 145.6 º. The lowest density and thermal conductivity belong to aerogels with E=10 and N=3.6. Aerogels could be used up to 40 % strain without permanent deformation. There is hardly any study that investigates the silica aerogels containing different porogenic agents and functional group as a novel nano-fillers in epoxy resin systems. Hence, this study aims to include the ionic liquids in sol-gel process to enhance the morphological and chemical characteristics of typical aerogels and therefore to yield a well-defined, mechanically reinforced aerogel-epoxy nanocomposites.

In this study, the silica aerogel was added as nano-filler into epoxy to investigate effect of the silica aerogel on the mechanical performance of silica aerogel–epoxy composites. Silica

aerogels in the study was prepared by sol-gel method, which is simply based on consequent hydrolysis and condensation reactions of a silica precursor in the presence of proper solvent and catalysts. Preparation of the sol, aging of the gel and drying stages are the crucial steps in the sol-gel method. Aging and drying periods are the key steps in the formation of three dimensional of porous network and should be carefully carried out. In the study, in addition to the classical sol components, organic salts with an extremely low vapor pressure called ionic liquids were also included in sol-gel steps to control the aging and drying steps and hence to obtained well-developed porous network.

Silica aerogels mediated with an imdazolium based ionic liquid were used in different amounts (0.5 and 1 wt. %) in the production of silica aerogel-epoxy nanocomposites to investigate their mechanical properties in this study. The effect of the silica aerogel on the tensile and flexural properties of the final composites were observed by the measurement of the tension and three-point bending tests, respectively. The results have shown that the mechanical behavior of the epoxy resin was significantly influenced by the silica aerogel addition. The mechanical strength of epoxy composite with silica aerogel addition was improved compared to that of neat epoxy composites.

2. Experimental

2.1. Preparation of the Silica Aerogels

Tetraethylorthosilicate (TEOS) as silica precursor and 3-aminopropyltriethoxy-silane (APTES) as co-precursor were acquired from Sigma Aldrich. 1-Ethyl-3-methylimidazolium bis(trifluoromethanesulfonyl)imide (EMIMTF$_2$N) was utilized as the short-chain imidazolium based ionic liquid, and 3-methacryloxypropyltrimethoxysilane (MEMO) as surface modification agent were purchased from Sigma Aldrich. Ethanol (EtOH) and n-hexane were used as solvents and hydrochloric acid (HCl) was used as the acid catalyst.

The silica aerogels were prepared by following one-step sol-gel processes containing ionic liquid. During the synthesis, TEOS was firstly hydrolyzed by using 0.01 M HCl for 90 min by stirring at 25 °C. Then APTES was added to the sol to start condensation reaction. The sol component consists of TEOS: APTES: IL: EtOH: HCl with the molar ratios of 1:0.47:0.14:6.3:7.4×10^{-5}. After complete gelation, the sample was allowed to age for 24 h in a polypropylene cylindrical mold to further continuation of the condensation reaction. Subsequently, the solvent exchange was carried out by treating the wet gels with fresh n-hexane for 12 h to ensure complete removal of the impurities within the gel. Then, surface modification was conducted by immersing the sample in silylating agent (MEMO) diluted with n-hexane at a volumetric percent of 50 % at room temperature. Finally, silica aerogel samples containing ionic liquid were dried in ambient condition.

2.2. Composite Preparation

The epoxy resin, hardener and mold release were purchased from Fibermak Co. (Turkey). As epoxy resin, diglycidyl ether of bisphenol A (DGEBA, trade name F1664) and as amine hardener, F3486 were used. The viscosity, density, color and glass transition temperatures were 1250- 1450 mPa s, 1,1 - 1,2 g/cm^3, colorless and 80ºC, respectively. A calculated amount of silica aerogel (0.5-1 wt. %) was distributed into epoxy resin using ultrasonic homogenizers (Hielscher, UP400S, 400 W and 24 kHz) (Figure 1). Half an hour of sonication was applied to silica aerogel-epoxy solution. The working conditions of Sonicator were 1 cycle and 100% amplitude. During sonication, solution temperature increases, for that reason, the mixture was taken into an ice bath.

Fig. 1 Ultrasonic homogenizer for dispersion silica aerogel.

Mold release was applied to all surfaces of aluminum mold for three times to easily remove the completely cured samples from the mold. Entrapped air was removed from both silica aerogel-epoxy and silica aerogel-epoxy-hardener mixture by using vacuum pump. When no bubbles remained in mixture, liquid was slowly poured into the mold (Figure 2).

Fig. 2 Pouring mixture into aluminum mold.

Curing of the prepared samples was carried out by arranging the sequence of process. Molds were initially kept at 50 °C for 5h. Then the temperature slowly decreased down to ambient temperature. After that, the samples were removed from slots. Three sets of composites were shown in Figure 3.
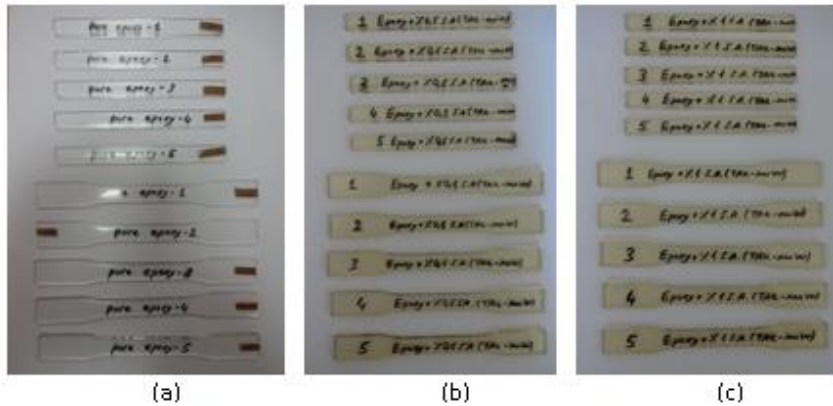
Fig. 3 Tensile and three point bending samples

(a) pure epoxy, (b) epoxy - 0.5 wt. % silica aerogel, (c) epoxy - 1 wt. % silica aerogel.

2.3. Characterizations

To identify the microstructure of the composites, Scanning Electron Microscopy (SEM) images of the samples were taken with various magnification rates.

Tensile tests were carried out with a universal testing machine (Shimadzu). These tests were performed according to ASTM D638-14 and the loading rate was set as 5 mm/min at 25°C until material failure. The geometry of samples was dog bone therefore rupture was observed from the thinner section. During the test, load and displacement data were directly received. Then, the load displacement curve for each test was converted to a stress–strain curve. Stress and strain formulas were given in Eq. 1 and 2:

$$\sigma = \frac{F}{A} \quad \text{[MPa]} \tag{1}$$

$$\varepsilon(\%) = \frac{\Delta L}{L} \; x100 \tag{2}$$

where F is force (N), A is area (mm²), ΔL is elongation (mm) and L is gauge length (mm).

Three-point bending test was performed with a Shimadzu machine according to ASTM D790-17. In this test, the rectangular cross section samples were prepared with dimensions of 127x12.7x3.2 mm as shown in Figure 3. Loading rate was set at 2 mm/min. The ratio of support span to thickness was 16. Stress-strain formulas in three-point bending were given in Eq. 3 and 4:

$$\sigma = \frac{3Fl}{2wt^2} \quad \text{[MPa]} \tag{3}$$

$$\varepsilon(\%) = \frac{6\delta t}{l^2} \; x100 \tag{4}$$

where F is force (N), w is width (mm), t is thickness (mm) and l is support span (mm), δ is deflection (mm).
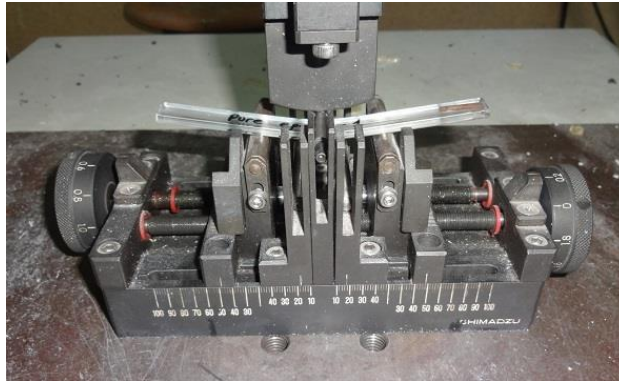
Fig. 4 Photograph of the three-point bending test.

Tensile and three-point bending tests were repeated five times to achieve reliable results for the neat epoxy and each of silica aerogel-epoxy composites.

3. Results and Discussions

3.1. Morphology of the Composites

SEM images of the nanocomposites were obtained to investigate the morphology of the final composites and to observe the distribution of the silica aerogel powders in epoxy resin. The SEM images of the ionic liquid mediated silica aerogel/epoxy nanocomposites were shown in Fig. 5. It can be seen from Fig. 5a-c that the morphology of nanocomposites became rougher in the presence of silica aerogels. The small amount of silica aerogel was uniformly dispersed in epoxy resin, which resulted in good interfacial adhesion between filler and matrix. However, as the amount of silica aerogel addition was increased up to 1 wt. % in epoxy, aerogel particles tend to agglomerate as small clusters. The possible reason for this situation can be the interaction between functional groups on the filler surface and matrix that leads less homogeneous dispersion. On the other hand, silica aerogel-epoxy composite with 0.5% silica aerogel addition seemed to be distributed more homogenously than the composite having 1% silica aerogel addition.
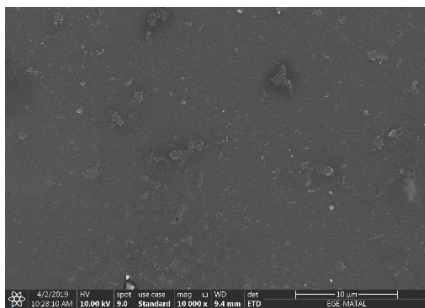
(a)
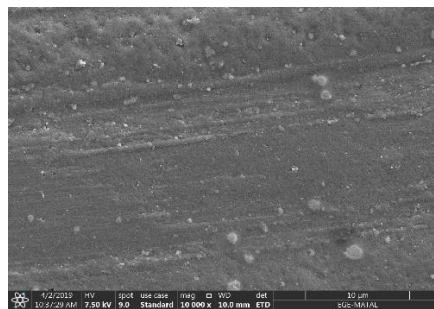
(b)
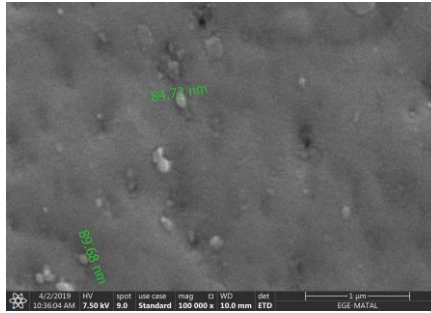
(c)

Fig 5. SEM images of SA-epoxy nanocomposites

a- Epoxy + 0.5 % S.A, b- Epoxy + 1 % S.A, c- Epoxy + 0.5 % S.A.

3.2. Tensile Properties of the Composites

Tensile tests were performed to measure the effect of the silica aerogel particles on the mechanical properties of the epoxy composites. Tensile properties of the silica aerogel–epoxy composites were reported in Table 1.

Table 1 Tensile properties of silica aerogel-epoxy composite.

Specimen/Value	Ultimate Stress (MPa)	Modulus of Elasticity (MPa)	Break strain (%)
Pure Epoxy	41.725 ± 2.666	316.028 ± 17.797	14.350 ± 2.388
Epoxy + 0.5 % S.A	49.207 ± 2.611	598.252 ± 49.907	10.951 ± 1.529
Epoxy + 1 % S.A	53.939 ± 2.022	566.204 ± 7.993	11.760 ± 0.951

The modulus of elasticity (Young's modulus) of the samples was identified by the slope of the initial linear portion of the stress-strain curve obtained during tensile tests. Stress – strain curve of the one of the specimens in each group was shown in Figure 6.
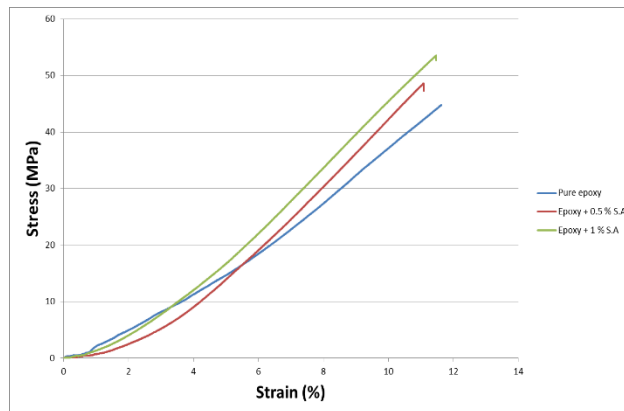

Fig. 6 Tensile stress – strain diagram of nanocomposites

The first considerable outcome was that the tensile strength significantly increased with addition of small amount of silica aerogel. The increment of tensile strength was 18 % and

29 % compared to pure epoxy for 0.5 and 1 wt. % silica aerogel composites, respectively. In addition, rigidity of epoxy composite increased with silica aerogel addition. Approximately, twice of modulus of elasticity was obtained with 0.5 wt. % silica aerogel addition. The reason for increment of tensile strength and modulus was due to the high specific surface area of silica aerogel. Because of this, content area between silica aerogel and epoxy was sufficient to transfer forces to matrix.

However, elongation at break for silica aerogel composites was smaller than that of pure epoxy. The decrement of break strain was found 24 % and 18 % for 0.5 wt. % and 1 wt. % silica aerogel composites, respectively. Silica aerogel may have caused micro-crack formation and early failure.

3.3. Flexural Properties of the Composites

The reaction of composite for bending moment was obtained with three-point bending test. Samples were placed on two stationary supports and load was applied on the middle of the sample. Flexural stress, modulus and break strain were calculated. Flexural modulus was obtained with drawing a tangent line to stress-strain curve. Flexural properties of the silica aerogel–epoxy composites were reported in Table 2.

Table 2 Flexural properties of silica aerogel-epoxy composite.

Specimen/Value	Ultimate Bending Stress (MPa)	Bending Modulus (MPa)	Break strain (%)
Pure Epoxy	108.484 ± 6.199	2960.623 ± 188.427	13.113 ± 3.189
Epoxy + 0.5 % S.A	115.892 ± 4.894	3475.490 ± 169.119	13.610 ± 0.211
Epoxy + 1 % S.A	99.497 ± 4.190	2831.092 ± 158.945	13.434 ± 1.292

Flexural properties divided from tensile properties. Ultimate bending stress and bending modulus were increased for 0.5 wt. % and decreased for 1 wt. % silica aerogel composites. Composite with 0.5 wt. % showed 7 % and 17 % increase in bending stress and bending modulus, respectively. Additionally, increase in flexural break strain was not significant. Only 4 % increment was observed. The stress – strain diagram for one specimen in each group was plotted in Fig 7.
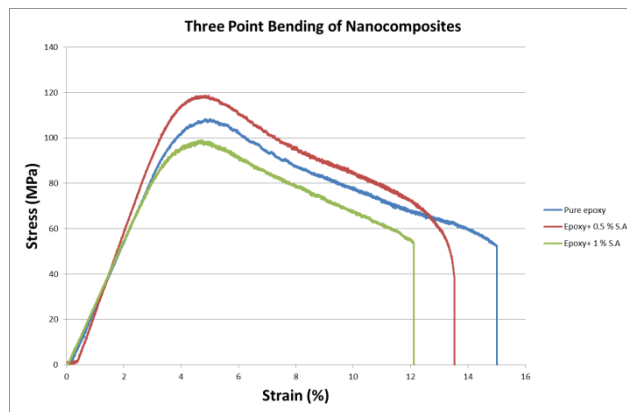

Fig. 7 Three point bending stress – strain diagram of nanocomposites

When silica aerogel content was 1 wt. %, ultimate bending stress and bending modulus were smaller than that of pure epoxy. 8 % and 4 % decrement were observed, respectively. Moreover, flexural break strain showed medium results. It was located between pure and containing 0.5 wt. % silica aerogel composite. By adding 1 wt. % silica aerogel into epoxy, flexibility of the composite was increased. Since 0.5% silica aerogel containing epoxy was produced homogenously, it was resulted in good bending properties. On the other hand, increasing aerogel content in epoxy resin has caused some agglomeration within the matrix and hence, it resulted with local concentrated stress and bending strength decreased for this reason.

4. Conclusion

In this study, the effect of silica aerogel on the mechanical properties of epoxy composites was investigated. Silica aerogels were produced with sol gel method. Two silica aerogel–epoxy composites with different silica contents were prepared to perform mechanical tests. Silica aerogels were distributed into epoxy resin by ultrasonic cavitation technique. ASTM D638-14 and D790-17 standard mechanical tests were performed. The mechanical analysis displayed that the tensile and flexural properties was influenced by the addition of the silica aerogel with increasing weight percent from 0.5 wt. % to 1 wt. %. In addition, significant improvements in the Young's modulus (89 %), tensile strength (18 %) and flexural modulus (17 %) were observed with the optimal content of silica aerogel (0.5 wt. %). Due to the large pore volume of silica aerogels and strong interaction with epoxy, mechanical properties of nanocomposites were increased. Epoxy resin filled the pore of silica aerogel and structural rigidity increased.

The results showed that the break strain of the neat epoxy composite decreased with adding silica aerogel content in tensile test. Due to the strong interfacial interaction between silica aerogel and epoxy resin, nanocomposites showed rigid structure. Although strength increased, break strain value decreased due to brittle behavior of the nanocomposites. The maximum bending strength, modulus and strain at break was attributed to the composite containing 0.5 wt. % silica aerogel in comparison to the neat epoxy. However, the flexural properties of the composites decreased when highest silica aerogel content was used. As seen from the SEM images, the bending properties of the 1 wt. % silica aerogel containing nanocomposite, which tends to agglomerate, was lower than that of pure epoxy.

Acknowledgements

References

[1]. Li M, Jiang H, Xu D, Hai O, and Zheng W. Low density and hydrophobic silica aerogels dried under ambient pressure using a new co-precursor method. Journal of Non-Crystalline Solids. 2016 Nov; 452: 187–193. https://doi.org/10.1016/j.jnoncrysol.2016.09.001

[2]. Li Z, Cheng X, He S, Shi X, Gong L, and Zhang H. Aramid fibers reinforced silica aerogel composites with low thermal conductivity and improved mechanical performance. Compos. Part A Appl. Sci. Manuf.2016; 84: 316–325. https://doi.org/10.1016/j.compositesa.2016.02.014

[3]. Laskowski J, Milow B, and Ratke L. Aerogel-aerogel composites for normal temperature range thermal insulations. Journal of Non-Crystalline Solids. 2016; 441: 42–48. https://doi.org/10.1016/j.jnoncrysol.2016.03.020

[4]. Soleimani Dorcheh A and Abbasi M. H. Silica aerogel; synthesis, properties and characterization. J. Mater. Process. Technol. 2008; 199-1:10–26. https://doi.org/10.1016/j.jmatprotec.2007.10.060

[5]. Parmenter K. E. Mechanical properties of silica aerogels. Journal of Non-Crystalline Solids. 1996 Nov; 1: 79–189.

[6]. Amonette J. E, and Matyáš J. Functionalized silica aerogels for gas-phase purification, sensing, and catalysis: A review. Microporous Mesoporous Materials. 2017; 250: 100–119. https://doi.org/10.1016/j.micromeso.2017.04.055

[7]. Maleki H, Dur L, and Garc C. A. Synthesis and Biomedical Applications of Aerogels: Possibilities and Chal- lenges Hajar. Advance Colloid Interface Science. 2016; 236: 1–27. https://doi.org/10.1016/j.cis.2016.05.011

[8]. Buratti C, Merli F, and Moretti E. Aerogel-based materials for building applications: Influence of granule size on thermal and acoustic performance. Energy Buildings. 2017; 152: 472–482. https://doi.org/10.1016/j.enbuild.2017.07.071

[9]. Berthon-Fabry S, Hildenbrand C, Ilbizian P, Jones E, and Tavera S. Evaluation of lightweight and flexible insulating aerogel blankets based on Resorcinol-Formaldehyde-Silica for space applications. Eur. Polym. J. 2017 May; 93: 403–416. https://doi.org/10.1016/j.eurpolymj.2017.06.009

[10]. Li Z, Gong L, Cheng X, He S, Li C, Zhang H. Flexible silica aerogel composites strengthened with aramid fibers and their thermal behavior. Materials and Design. 2016; 99: 349–55. https://doi.org/10.1016/j.matdes.2016.03.063

[11]. Chal B, Foray G, Yrieix B, Masenelli-Varlot K, Roiban L, Chenal J-M. Durability of silica aerogels dedicated to superinsulation measured under hygrothermal conditions. Microporous and Mesoporous Materials. 2018; 272: 61–69. https://doi.org/10.1016/j.micromeso.2018.05.047

[12]. Maleki H, Durães L, Portugal A. An overview on silica aerogels synthesis and different mechanical reinforcing strategies. J Non Cryst Solids. 2014; 385: 55–74. https://doi.org/10.1016/j.jnoncrysol.2013.10.017

[13]. Salimian S, Zadhoush A, Talebi Z, Fischer B., Winiger P., Winnefeld F., Zhao S, Barbezat M, Koebel M M, Malfait W J, Silica Aerogel–Epoxy Nanocomposites: Understanding Epoxy Reinforcement in Terms of Aerogel Surface Chemistry and Epoxy–Silica Interface Compatibility, Applied Nano Materials, 2018; 1: 4179-4189. https://doi.org/10.1021/acsanm.8b00941

[14]. Maghsoudi K, Motahari S. Mechanical, thermal, and hydrophobic properties of silica aerogel-epoxy composites. J Appl Polym Sci. 2018;135(3):1–9. https://doi.org/10.1002/app.45706

[15]. Lei Y, Hu Z, Cao B, Chen X, Song H. Enhancements of thermal insulation and mechanical property of silica aerogel monoliths by mixing graphene oxide. Materials Chemistry and Physics. 2017; 187: 183-190. https://doi.org/10.1016/j.matchemphys.2016.11.064

[16]. Li C, Cheng X, Li Z, Pan Y, Huang Y, Gong L. Mechanical, thermal and flammability properties of glass fiber film/silica aerogel composites. J Non Cryst Solids. 2017;457:52–59. https://doi.org/10.1016/j.jnoncrysol.2016.11.017

[17]. Zhou T, Cheng X, Pan Y, Li C, Gong L, Zhang H. Mechanical performance and thermal stability of glass fiber reinforced silica aerogel composites based on co-precursor method by freeze drying. Appl Surf Sci. 2018; 437: 321–328. https://doi.org/10.1016/j.apsusc.2017.12.146

[18]. Salimian S, Malfait W. J, Zadhoush A, Talebi Z, Naeimirad M. Fabrication and evaluation of silica aerogel-epoxy nanocomposites: Fracture and toughening

mechanisms. Theoretical and Applied Fracture Mechanics. 2018; 97: 156–164. https://doi.org/10.1016/j.tafmec.2018.08.007

[19]. Shafi S, Navik R, Ding X, Zhao Y. Improved heat insulation and mechanical properties of silica aerogel/glass fiber composite by impregnating silica gel. Journal of Non-Crystalline Solids. 2019; 503-504: 78–83. https://doi.org/10.1016/j.jnoncrysol.2018.09.029

[20]. Zhao Y, Li Y, Zhang R. Silica aerogels having high flexibility and hydrophobicity prepared by sol-gel method. Ceramics International. 2018; 44: 21262–21268. https://doi.org/10.1016/j.ceramint.2018.08.173

Technical Note

Two simple methods for surface modification of lithium disilicate dental blocks with hydroxyapatite

Mehmet Topuz[*1,2,a], Burak Dikici[3,b]

[1]*Department of Mechanical Engineering, Van Yüzüncü Yıl University, Van, Turkey*
[2]*Natural and Applied Sciences, Department of Mechanical Engineering, Atatürk University, Erzurum, Turkey*
[3]*Department of Metallurgical and Materials Engineering, Atatürk University, Erzurum, Turkey*

Article Info	Abstract
	Crowns are materials that attracting the attention and lithium disilicates among them widely used because of their high bulk mechanical features. Increasing the bioactivity of crowns has generally been a common aspect of all studies. In this study, lithium disilicate dental blocks were coated with bioactive calcium–phosphate components using sol–gel dip–coating methods to increase their surface bioactivity. Two coating methods called as slurry and powder methods were proposed to obtain dense and remarkable layer on the lithium disilicate substrates. The coating layers were characterized by scanning electron microscopy attached with energy dispersive spectroscopy. Coating procedures have successfully accomplished and show enhanced surface properties with terms of calcium/phosphate ratios. Tri–calcium phosphate obtained by the slurry method, which has 1.5 calcium/phosphate ratio, is a favorable structure for bio–absorbable. However, the powder method has approximately 1.67 calcium/phosphate ratio which necessary for hydroxyapatite (HA) structure for higher crystallinity and lower solubility properties.

1. Introduction

In the area of dentistry, highly detailed studies have been carried out for the restoration of the teeth that have been decaying, ageing or lost their function. As the technology progresses, always there is another innovation in the field of health. Especially in recent years, CAD/CAM technologies which have come into our lives have caused many developments in the field of dentistry. With the help of the new computer–aided image and design technology developed within this scope, it is possible to have new teeth in a short time like 40min [1]. The crown is a method of restoring damaged teeth for various reasons. Crowns can be used as an implant superstructure to prevent weakened teeth from cracking, repair a broken tooth, make a bridge, overcoat a lost or deformed tooth due to excessive caries. It can be made of full–metal, metal–backed porcelain or full–porcelain. Crowns are prepared according to the model. If porcelain is used, the natural tooth tone is determined and the support adheres to the tooth [2]. Ceramic dental materials used in CAD/CAM processes are classified according to their chemical content; feldspathic, low leucite–containing glass, lithium disilicate and mica reinforced, alumina and magnesium ceramics. The lithium disilicate consists of several randomly interleaved layers. In terms of fracture resistance, the needle–like crystals prevent both cracking and divergence of the cracks [3].

On the other hand, the biggest advantage of lithium disilicate crowns is that it does not need any reinforcing elements such as metal or zirconium in its infrastructure. In other words, they are kind of a porcelain type that has been made more than 3 times more durable than classical porcelain. So, what brings us to this increase in endurance? The fact that a prosthesis can be made without the use of a substructure gives us a great advantage in mimicking the characteristic appearance of natural teeth under the light. Besides, the fact that it can be worked with thinner means that less tissue will be removed from the teeth on which it will be made. According to the location of the prosthesis to be made, dentists had to make difficult decisions to be durable or aesthetic [4].

Calcium phosphates have the ability to increase bone formation in the surrounding tissue and implanted in the human skeletal system. They are used extensively as coating components due to the higher osteoblast orientation capabilities. The apatite compound of calcium phosphates is almost identical to the mineral phase of bone and tooth, especially HA [5].

Many techniques can be used for the coating of ceramic dental blocks such as sol–gel dip–coating, plasma electrolytic oxidation and plasma spray [6-8]. However, among these techniques, sol–gel dip–coating has easier process steps and also cheaper than others.

A similar study was done on zircon blocks by Azari et al. [9] and compared thermal coating and air abrasion methods. As a result of the study, the crystalline HA structure was found in the thermal coating method while in the air abrasion method HA mini–islands were encountered. Another research conducted by Azari et al. [10], suggested that HA coatings on zirconia blocks could be a solution for increasing the adhesion strength of resin cement. In another study on bone tissue formation, it was observed that HA coatings on zircon block contributed to the formation of new bone tissue [11]. It has been stated by many researchers that there will be no problems with adhesion resistance at the abutment–crown interface with the use of hydrofluoric acid [12,13]. However, different surfaces are being studied to investigate the living cell reaction at the interface [14]. Therefore, it has become necessary to investigate whether the bioactivity can be increased by coating lithium disilicate surfaces.

In this study, lithium disilicate dental blocks were coated with calcium phosphate components to increase their surface bioactivity. Two different coating methods (called as a slurry (LD-S) and powder (LD-P) methods) were proposed to obtain dense and remarkable layer on the lithium disilicate substrates. The synthesis steps are discussed in details, comparatively.

2. Materials and Methods

Lithium disilicate materials with dimensions 14.4×14.4×18mm were used as a substrate for coating procedures (Ivocolar IPS e.max CAD). The standard structure of blocks was; 57.0-80.0% SiO_2, 11.0-19.0% Li_2O, 0.0-13.0% K_2O, 0.0-11.0% P_2O_5, 0.0-8.0% ZrO_2, 0.0-8.0% ZnO, 0.0-10.0% other oxides (Al_2O_3 and MgO) and consists of 0.0-8.0% color oxides by means of weight. First of all, the samples were sandblasted by Al_2O_3 particles of 150µm. The aim of sandblasting is to obtain better wettability between substrates and coating layer. Subsequently, the surface cleaning process was carried out in distilled water (DW) for 15min in order to remove surface residues after sandblasting.

Two different coatings procedures (LD-S: slurry) and (LD-P: powder) were used to examine the characteristics of HA coatings synthesized on the base materials. The first one is the dipping into the slurry solution and the other is powdered and sintered HA's into a solution and the surface is coated with a dipping process. Agar was used in order to obtain a higher wettability on the surface. Synthesis of the LD-S coatings, the sol–gel method was

used in which low sintering temperatures were sufficient, allowing complex shapes to be easily coated. In the synthesis of the sols, ethyl alcohol (Sigma–Aldrich), calcium nitrate tetrahydrate (Calcium source: $Ca(NO_3)_2 \cdot 4H_2O$, Sigma–Aldrich), di-ammonium hydrogen phosphate (Phosphate source: $(NH_4)_2HPO_2$, MERCK) and agar (MERCK) were used as precursors. The amount of precursors which used for procedures was determined from the Ca/P stoichiometric ratio of HA. 12.619g of calcium nitrate tetrahydrate and 4.457g of phosphorus pentoxide were dissolved in two separate 500ml breakers with 100 and 120ml DW, respectively. After one hour stirring 75ml ammonia was added to $(NH_4)_2HPO_2$ solution and stirred 10min more. Then Ca solution, 1.708g agar (1wt%) was added to P solution slowly, and 10min stirred. The mixed solution was heated until boiling and stirred 10min while boiled. The boiled solution was waited in order to the aging of sol. for 24h. Unlike the LD-S procedure, LD-P procedure has different steps. Firstly, the slurry solution (LD-S procedures last step) filtered for 1 day to squeeze the excess amount of ammonia in the solution. Then dried in an oven at 200°C for 4h, to evaporate the residual ammonia and organic components in the wet cakes, and pulverized with the aid of a mortar. The CaP powders were sintered at 1000°C for 1h. 2g CaP powder was mixed for 2h in 50ml DW for obtaining coating sol. After these steps, both sols were homogenized ultrasonically for 20min at 25% duty rate to obtain homogenous sol. before dipping. The samples were dip-coated for three times to obtain thicker films on its, and every dip-coating steps were pre-dried at 40°C for 5min. Finally, samples were sintered for 2h at 300°C for LD-S and 200°C for LD-P procedures. In pre-sintering trials, small burn marks on the surfaces of lithium disilicate materials were effective in the selection of sintering temperatures. In the LD-S procedure, the sintering temperature is determined as 300°C, because the reactions between Ca and P can be occur. In the LD-P procedure, since the powders were sintered at 1000°C before coating, 200°C sintering temperature was considered sufficient. The algorithmic flow chart of both procedure is presented in Fig. 1.

Phase formations in the coatings were investigated by X–Ray diffraction (XRD, Bruker D8). XRD analyses were performed on a stage which using a radiation wavelength $\lambda=1.54056$Å X–ray source with a scan rate of $0.06°\cdot s^{-1}$ between 10 to 90°. Microstructural characterization of the coatings was performed using scanning electron microscopy (SEM, JEOL JSM-6335F) and energy dispersive spectroscopy (EDS, Oxford Inca). Because the coatings are ceramic–based, they were coated with Au–Pd alloy prior to the examination to improve the image quality for SEM and EDS examinations.

4. Results and Discussions

SEM surface morphology and EDS result of LD-S coated samples are given in Fig. 2. When the SEM surface morphologies are examined, it is seen that there are micron–size pores in some parts of the coating structure. It is thought that these micron–sized pores formed because of the lack of surface wetting by the LD-S solution. It was also mentioned by other researchers that the nano–sized crystal structures in the pore were lithium disilicate [15]. Researchers reported that the nano–sized lithium disilicate crystals which noodles–like shaped could improve the strength of the material because of the different orientation of these crystals [3]. This situation was also determined by EDS analysis that the electron energy distribution of Si element was observed at 1.739 keV.
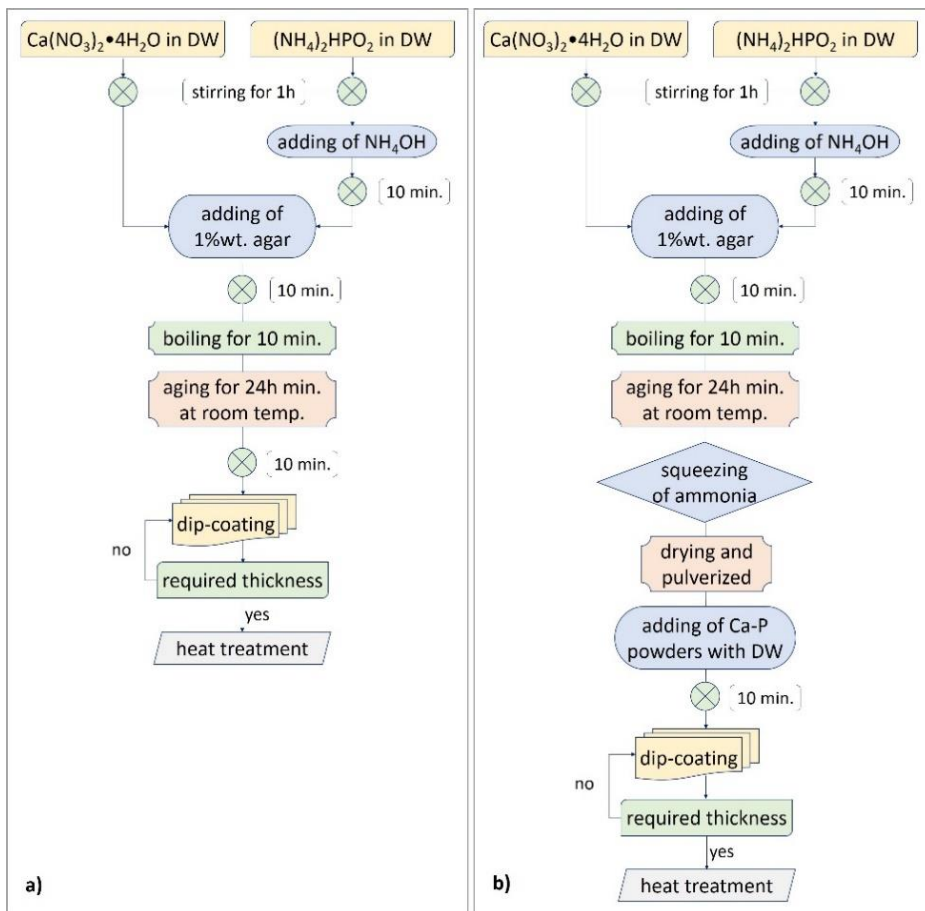
Fig. 1 Algorithmic flow charts of (a) LD-S and (b) LD-P synthesis of HA sols
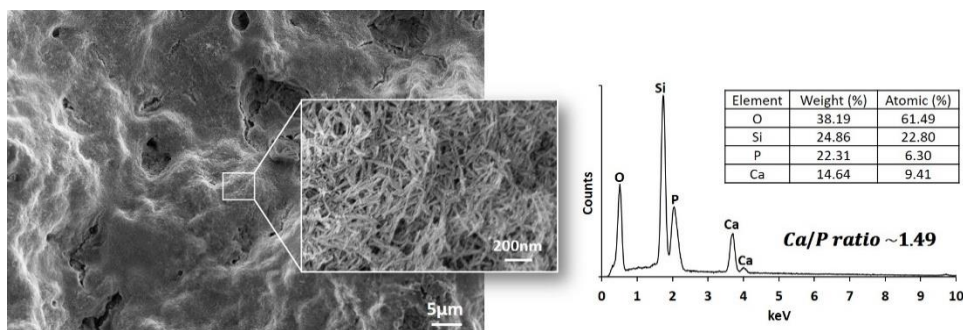

Fig. 2 SEM surface morphology of LD-S coated sample and EDS result

On the other hand, calcium and phosphate elements on the surface have been proven by EDS analysis, and the Ca/P atomic ratio (~1.49) was determined to be tri–calcium phosphate (β–TCP, Ca/P ratio 1.5) [5]. It has been mentioned by many other researchers that this β–TCP structure has lower crystallinity compared to the HA structure and resulted in higher solubility but has similarly improved osseointegration properties [16]. The low Ca/P ratio and low crystallinity values achieved may be due to the fact that coating components are made at low sintering temperatures (300°C for LD-S). On the other hand,

high sintering temperatures to be used in the coating affect the long–term service life as it causes permanent damage to the substrate or changes in the grain structure.
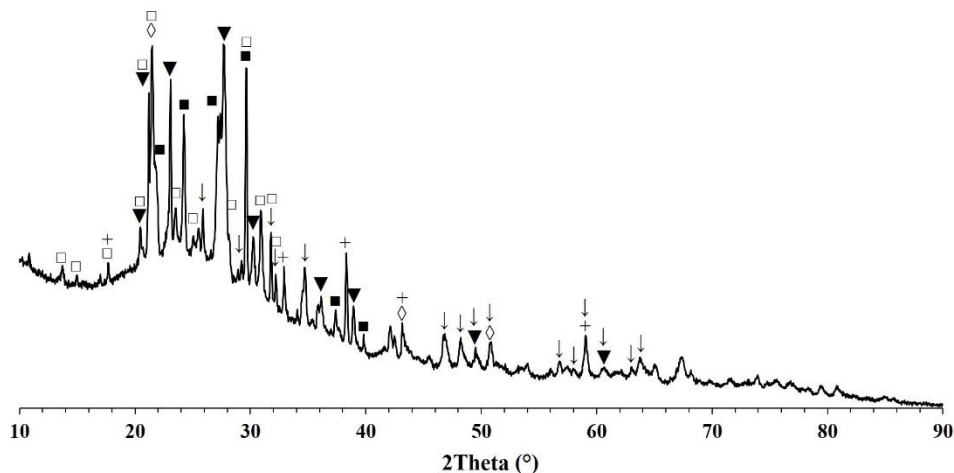
Fig. 3 XRD result of LD-S coated sample, legends are; ↓ HA, ◊ Cristoballite (SiO_2), ■ $Li_2Si_2O_5$, ▼ Trdymite (SiO_2), +Li_2SiO_3, □ β–TCP

XRD analyze of LD-S coated samples was given in Fig. 3. As shown from XRD result of LD-S sample, β–TCP structure was confirmed with 09-0348 JCPDS card number. This result agrees with EDS analyze result. LD-S coated samples show small amount of HA peaks (09-0432) which may be observed as it is sintered at the β–TCP–HA transition temperature. On the other hand, different phases such as Cristoballite (SiO_2), Trdymite (SiO_2), $Li_2Si_2O_5$ and Li_2SiO_3 were found from the base material (JCPDS card numbers are; 01-0424, 01-0378, 040-0376 and 010-0017 respectively). It is thought that phases which contain lithium and silicate come from the substrate materials, due to the inhomogeneous surface morphology of the coating.
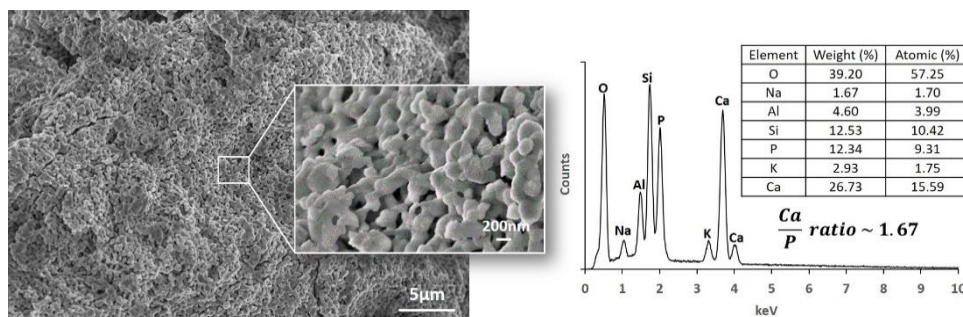

Fig. 4 SEM surface morphology of LD-P coated sample and EDS result

The SEM surface morphology and EDS results of the coating synthesized by the LD-P method are shown in Fig. 4. It can be shown that from Fig. 4 the surface is smoother than LD-S and has nano–sized pores. These nano-sized pores may responsible for enhanced biocompatibility. Unlike the LD-S method, the Ca/P ratio was measured as 1.67 in this method, atomically. In order to determine whether HA which another calcium phosphate structure is formed, the researchers decide either the Ca/P ratio or the XRD test. As it is known from the literature, the Ca/P ratio of HA is 1.67 and it is the same as the value obtained in this method [17,18]. It was determined that the Na, Si, and K elements of the

EDS results from the blocks which used as substrate material [2], Al element was determined due to the blasting process applied before the coating. The high crystallinity of the HA shows that it will not dissolve easily and have a long life in the physiological environment. The surfaces similar to the surface of the LD-P were also obtained by other researchers [19,20].
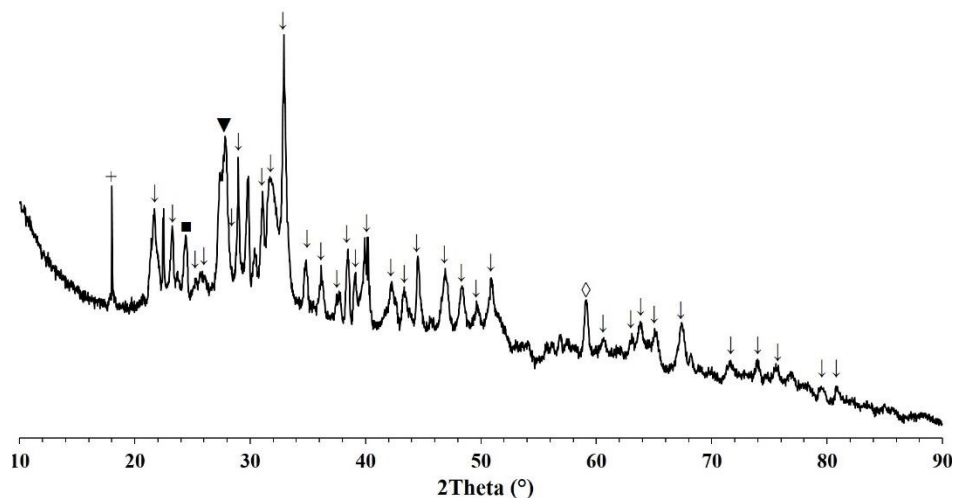

Fig. 5 XRD result of LD-P coated sample, legends are; ↓ HA, ◊ SiO_2, ■ $Li_2Si_2O_5$, ▼ SiO_2, +Li_2SiO_3

Phase formations and transformations (XRD result) of LD-P coated samples are presented in Fig. 5. These results were in agreement with SEM/EDS results. When compared with XRD results of LD-S samples, it is seen that XRD peak widths of LD-P samples are narrower and this may be caused by pre–sintering process applied in LD-P method. Unlike LD-S method's XRD result, LD-P coated sample has completely HA phases on it.

Findings from the studies emphasized that agar causes Ca deficiency in HA structure [21]. Ouyang et al. [22] were found that the amount of agar decreased to about 30% by weight, but not completely decomposed by heat treatment at 300°C. The difference in Ca/P ratios between LD-S and LD-P procedures is thought to be due to the agar's removal from the coating composition after 1000°C of heat treatment for powdering in the LD-P procedure. As can be seen from the researches, the sintering temperature of the LD-S procedure was 300°C, did not completely decompose the agar from the coating composition. Thus, it is evident that a small amount of agar remaining in the coating composition leads to Ca deficiency and a low Ca/P ratio. Besides SEM/EDS analyses, phenomenon which formation of both β–TCP and HA, proved by XRD results. $Li_2Si_2O_5$ was major phase from substrate materials but there is a small amount of SiO_2 and Li_2SiO_3 peaks which may occur nucleation of Li and Si during sintering. It's thought that such higher intensities, as can be seen in XRD results, are favorable to human body due to the lower soluble behavior.

Also, as Narayanan et al. [23] mentioned, β–TCP stated that it could be absorbed in the body and HA could not be absorbed. While absorption in the body is a more important condition, due to the unpredictable dissolution behavior of β–TCP, HA which has high stability properties, is more desirable. After all these results and discussions, the LD-P procedure is thought to be an alternative coating procedure for lithium disilicate ceramics due to its HA structure and surface homogeneity. HA formation on LD-P coated samples were proved by XRD results. In addition, it is thought to have a positive effect on cell growth at the

abutment–crown interface with its optimal Ca/P ratio and will not cause any adverse reactions.

5. Conclusion

In this study, lithium disilicate blocks used in the field of dentistry were investigated by using two different methods and their ability to form a possible calcium phosphate component was investigated. The coatings obtained in the LD-P method were found to be more preferable both as surface morphologies and Ca/P ratio. In the literature, there are a few studies which conducted on surface morphologies of HA coatings on lithium disilicates but it is suggested that osteoconductivity or osteoblast formability tests of the coatings synthesized by both methods will be made and investigated in the future.

References

[1] Liu P-R. A Panorama of dental CAD/CAM restorative systems. Compendium of continuing education in dentistry. 2005;29(7):507-512.

[2] Figueiredo-Pina CG, Patas N, Canhoto J, Claudio R, Olhero SM, Serro AP, Ferro AC, Guedes M. Tribological behaviour of unveneered and veneered lithium disilicate dental material. Journal of the Mechanical Behavior of Biomedical Materials. 2016;53:226-238. http://dx.doi.org/10.1016/j.jmbbm.2015.08.007

[3] Ural Ç. Diş Hekimliği Pratiğinde Tamamı Seramik ve Cad-Cam Uygulamaları. Dirim Tip Gazetesi. 2011;86:27-38.

[4] Tysowsky G. The Science Behind Lithium Disilicate: Today's Suprisingly Versatlie, Esthetic & Durable Metal-Free Alternative. Oral Health. 2009;99(3):93-97.

[5] Topuz M. Production of Bioactive Hybrid Coatings on Beta (β) –Type Titanium Alloys, Characterization and Investigation of In-vitro Corrosion Properties, Ms Thesis, Yüzüncü Yıl University, Van, Turkey, 51-52, 2016.

[6] Dikici B, Niinomi M, Topuz M, Say Y, Aksakal B, Yılmazer H, Nakai M. Synthesis and characterization of hydroxyapatite/TiO2 coatings on the β-type titanium alloys with different sintering parameters using sol-gel method. Protection of Metals and Physical Chemistry of Surfaces. 2018;54(3):457-462. https://doi.org/10.1134/S2070205118030255

[7] Songur F, Dikici B, Niinomi M, Arslan E. The plasma electrolytic oxidation (PEO) coatings to enhance in-vitro corrosion resistance of Ti–29Nb–13Ta–4.6Zr alloys: The combined effect of duty cycle and the deposition frequency. Surface and Coatings Technology. 2019;374:345-354. https://doi.org/10.1016/j.surfcoat.2019.06.025

[8] Xu H, Geng X, Liu G, Xiao J, Li D, Zhang Y, Zhu P, Zhang C. Deposition, nanostructure and phase composition of suspension plasma-sprayed hydroxyapatite coatings. Ceramics International. 2016;42(7): 8684-8690. https://doi.org/10.1016/j.ceramint.2016.02.102

[9] Azari A, Jamnani SN, Yazdani A, Atri F, Rasaie V, Yazdi AFA. Deposition of Crystalline Hydroxyapatite Nanoparticles on Y-TZP Ceramic: A Potential Solution to Enhance Bonding Characteristics of Y-TZP Ceramics. Journal of Dentistry (Tehran). 2017;14(2):62-68.

[10] Azari A, Nikzad S, Yazdani A, Atri F, Yazdi AFA. Deposition of crystalline hydroxyapatite nano-particle on zirconia ceramic: a potential solution for the poor bonding characteristic of zirconia ceramics to resin cement. Journal of Materials Science: Materials in Medicine. 2017;28(7). https://doi.org/10.1007/s10856-017-5921-8

[11] Hirota M, Hayakawa T, Ohkubo C, Sato M, Kara H, Toyama T, Tanaka Y. Bone responses to zirconia implants with a thin carbonate-containing hydroxyapatite coating using a

molecular precursor method. Journal of Biomedical Materials Research - Part B Applied Biomaterials. 2014;102(6):1277-1288. https://doi.org/10.1002/jbm.b.33112

[12] Lanza MDS, Lanza FJSR, Manso AP, Matinlinna JP, Carvalho RM. Innovative surface treatments for improved ceramic bonding: Lithium disilicate glass ceramic. International Journal of Adhesion and Adhesives. 2018;82:60-66. https://doi.org/10.1016/j.ijadhadh.2017.12.007

[13] Prochnow C, Pereira GKR, Venturini AB, Scherer MM, Rippe MP, Bottino MC, Kleverlaan CJ, Valandro LP. How does hydrofluoric acid etching affect the cyclic load-to-failure of lithium disilicate restorations. Journal of the Mechanical Behavior of Biomedical Materials. 2018;87:306-311. https://doi.org/10.1016/j.jmbbm.2018.07.040

[14] Mehl C, Kern M, Schütte A-M, Kadem LF, Selhuber-Unkel C. Adhesion of living cells to abutment materials, dentin, and adhesive luting cement with different surface qualities. Dental Materials. 2016;32(12):1524-1535. https://doi.org/10.1016/j.dental.2016.09.006

[15] Küçük BE, Kunt GE. Lityum Disilikat Seramikler. Atatürk University Journal of Dentistry Faculty. 2012;5:123-131.

[16] Zhang J, Iwasa M, Kotobuki N, Tanaka T, Hirose M, Ohgushi H. Fabrication of hydroxyapatite-zirconia composites for orthopedic applications. Journal of the American Ceramic Society. 2006;89(11):3348-3355. https://doi.org/10.1111/j.1551-2916.2006.01237.x

[17] Janković A, Eraković S, Mitrić M, Matić IZ, Juranić ZD, Tsui GCP, Tang C, Misković-Stanković V, Rhee KY, Park SJ. Bioactive hydroxyapatite/graphene composite coating and its corrosion stability in simulated body fluid. Journal of Alloys and Compounds. 2015;624:148-157. https://doi.org/10.1016/j.jallcom.2014.11.078

[18] Dikici B, Niinomi M, Topuz M, Koç SG, Nakai M. Synthesis of biphasic calcium phosphate (BCP) coatings on β–type titanium alloys reinforced with rutile-TiO2 compounds: adhesion resistance and in-vitro corrosion. Journal of Sol-Gel Science and Technology. 2018;87(3):713-724. https://doi.org/10.1007/s10971-018-4755-2

[19] Karamian E, Khandan A, Kalantar Motamedi MR, Mirmohammadi H. Surface characteristics and bioactivity of a novel natural HA/zircon nanocomposite coated on dental implants. BioMed Research International. 2014;2014:1-10. http://dx.doi.org/10.1155/2014/410627

[20] Pardun K, Treccani L, Volkmann E, Streckbein P, Heiss C, Destri GL, Marletta G, Rezwan K. Mixed zirconia calcium phosphate coatings for dental implants: Tailoring coating stability and bioactivity potential. Materials Science and Engineering C. 2015;48:337-346. https://doi.org/10.1016/j.msec.2014.12.031

[21] Deng Y, Wang H, Zhang L, Li Y, Wei S. In situ synthesis and in vitro biocompatibility of needle-like nano-hydroxyapatite in agar-gelatin co-hydrogel. Materials Letters. 2013;104:8-12. https://doi.org/10.1016/j.matlet.2013.03.145

[22] Ouyang Q-Q, Hu Z, Li S-D, Quan W-Y, Wen L-L, Yang Z-M, Li P-W. Thermal degradation of agar: Mechanism and toxicity of products. Food Chemistry. 2018;264(March);277-283. https://doi.org/10.1016/j.foodchem.2018.04.098

[23] Narayanan R, Seshadri SK, Kwon TY, Kim KH. Calcium phosphate-based coatings on titanium and its alloys. Journal of Biomedical Materials Research - Part B Applied Biomaterials. 2008;85(1):279-299. https://doi.org/10.1002/jbm.b.30932

Research on
Engineering Structures & Materials

In This Issue

C O N T E N T

Research on
Engineering
Structures & Materials

Research Group